

Investigations on the techniques for development of high resolution optical systems for earth observation

*A thesis submitted
in partial fulfilment for the Degree of*

Doctor of Philosophy

by

M. SENTHIL KUMAR



Department of Physics

INDIAN INSTITUTE OF SPACE SCIENCE AND TECHNOLOGY

Thiruvananthapuram – 695547

JULY 2014



www.iist.ac.in



भारतीय अंतरिक्ष विज्ञान एवं प्रौद्योगिकी संस्थान

(वि.अ.आयोग अधिनियम 1956 की धारा-3 के अधीन भावी मानित विश्वविद्यालय घोषित)

भारत सरकार, अंतरिक्ष विभाग, वलियमला पोस्ट, तिरुवनंतपुरम 695 547 भारत

Indian Institute of Space Science and Technology

(A Deemed to be University u/s 3 of the UGC Act, 1956)

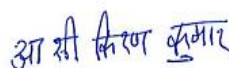
Government of India, Department of Space

Valiamala P.O., Thiruvananthapuram 695 547 India

CERTIFICATE

This is to certify that the thesis entitled **Investigations on the techniques for development of high resolution optical systems for earth observation** submitted by **M. Senthil Kumar** to the Indian Institute of Space Science and Technology, Thiruvananthapuram, in partial fulfillment for the award of the degree of **Doctor of Philosophy** is a bona fide record of research work carried out by him under our supervision. The contents of this thesis, in full or in parts, have not been submitted to any other Institution or University for the award of any degree or diploma.



C.S. Narayanamurthy
Supervisor
आचार्य एवं अध्यक्ष, भौतिकी विभाग
Senior Professor and Head
Scientist
भारतीय अंतरिक्ष विज्ञान एवं प्रौद्योगिकी संस्थान
Department of Physics
IIST
Department of Space, Govt. of India
Thiruvandrum (India) 695 547


A.S. Kiran Kumar
Supervisor
Distinguished SCIENTIST

Director
SAC, ISRO
Ahmedabad (India)

Thiruvananthapuram - 695 547

July 2014


Head
Department of Physics
डॉ. सी. एस. नारायणमूर्ति
Dr. C.S. Narayanamurthy
आचार्य एवं अध्यक्ष, भौतिकी विभाग
Prof. & Head, Dept. of Physics
भारतीय अंतरिक्ष विज्ञान एवं प्रौद्योगिकी संस्थान
Indian Institute of Space Science and Technology
अंतरिक्ष विभाग, भारत सरकार
Department of Space, Govt. of India
तिरुवनंतपुरम 695 547

DECLARATION

I declare that this thesis entitled **Investigations on the techniques for development of high resolution optical systems for earth observation** submitted in partial fulfilment of the degree of **Doctor of Philosophy** is a record of original work carried out by me under the supervision of Dr. C.S. Narayanamurthy (IIST) and Shri A.S. Kiran Kumar (SAC, ISRO), and has not formed the basis for the award of any other degree or diploma, in this or any other Institution or University. In keeping with the ethical practice in reporting scientific information, due acknowledgements have been made wherever the findings of others have been cited.


[M. Senthil Kumar]
[SC10D011]

Thiruvananthapuram - 695 547

03.07.2014

ACKNOWLEDGMENTS

There are several individuals, institutions, establishments directly or indirectly contributed to me to reach this position. I take this space to sincerely acknowledge their role in my progress. I also would like to sincerely thank Indian Space Research Organisation (ISRO), Department of Space (DOS) for providing me an opportunity to pursue Ph.D. at Indian Institute of Space science and Technology (IIST), Thiruvananthapuram.

Prof. C.S. Narayanamurthy, research supervisor and head of physics department, deserves a great deal of thanks for accepting me to register with him. He had supported and helped a lot during the six months residential period at IIST, and also throughout my research work. I always wonder the way he carry forward the things; with his own enthusiastic, energetic, intuitive and jovial way. His encouragement and freedom made me to enjoy doing work under his supervision.

I owe my deepest gratitude to Shri A.S. Kiran Kumar, research supervisor and director of SAC, he is one who persuaded me to join Ph. D. I express my thanks for believing in my interest and providing freedom to work. It is a constant learning from him from the day one I joined his division, Sensors Systems Division (SSD) in 1991. I thank all discussions during the design and development of optical systems that were first of its kind for various satellites. I always admire his involvement and hard work.

I take this opportunity to thank Dr. K.S. Dasgupta, director IIST for his encouragement and support to accomplish this work. I would like to thank my doctoral committee - Prof. Kothiyal, Late Dr. C.L. Nagendra, Prof. Kurian, Dr. Anathamayee Tej for their critical reviews and valuable suggestions. My thanks are due to office of dean R&D and dean Academics.

I would like to acknowledge my division colleagues Dr. Gopal, Manish, Anita, Mukesh, Rahul - those who have supported directly or indirectly during this work. My thanks are due to Mr. K.N Mankad of SAC for his support during the final lap

of my research work. I owe my deep gratitude to Dr. Subbarao who has meticulously read through the initial manuscript and offered his valuable suggestions. I would like to express my thanks to colleagues of Sensor mechanical group, Climatic test facility and Material quality evaluation division for providing necessary fabrication, test and evaluation support.

Special thanks are due to my group-mates during the residential period of Ph. D- Ameya, Baskhar, Lithesh, Muthu, Raja, Ranajit, Sanid, Srinivas, Jalaja, Remya, Richa, Hari, Kavita, Sarika. Being the first batch of Ph. D. in IIST, moving together to vast separated lecture-halls and facing new challenges, it was a back to school experience. Those are the people made my six months stay at IIST easy and memorable. My sincere thanks are also due to Mr. Ananthakumar, Mrs. Bindya, Mr. Remakrishnan, Mr. Vinod, Mr. Bipin for providing me the required support during the stay at IIST. I express my thanks to the entire IIST faculty who all had supported and encouraged me during this work.

My sincere thanks are due to Dr. Navalgund, former director of Space Applications Center (SAC), Ahmedabad for granting me the permission and also due to Dr. B. N. Suresh, former director of IIST for providing me an opportunity to join IIST. Special thanks are due to all experts who have interacted in any form during this work.

I take this space to express my deepest gratitude to my parents, relatives, teachers, classmates, colleagues and friends those who had helped in any form to attain this position. Finally, I express my thanks to my wife Devi and my daughter Dhakshika for carrying forward during my absence and also whatever support they could render during this work.

M. Senthil Kumar

ABSTRACT

Optical system is one of the major elements of a sensor for remote sensing. Remote sensing is acquiring of information about an object or phenomenon without making physical contact with it. A large number of missions carrying variety of sensors have been launched providing priceless information leading to the establishment and operationalization of a large number of applications of the remote sensing technology. Earth observation satellites are categorized as low (> 100 m), medium (10-100 m) and high (< 10 m) spatial resolution. Over the years with the advent of newer technologies, there is a growing demand for higher spatial resolution optical system for the earth observation. The limiting resolution for observing the earth through atmosphere i.e., from space is estimated as 4.6 cm. One can expect that the demand for the spatial resolution of a classical earth observation sensor may extend till the limiting resolution.

The performance metric of an imaging system is, in general, defined by the product of the modulation transfer function and the signal to noise ratio. The desirable goal of a sensor design is to achieve a near photon noise limited signal to noise ratio and a diffraction limited modulation transfer function at nyquist spatial frequency. The modulation transfer function, more pertinent to optical systems, mainly depends on the optical system aperture ratio. In the past, smaller F-number (typically F/4) optical systems were adopted to have adequate margin for the modulation transfer function and the signal to noise ratio with respect to the final specification. Increase in spatial resolution demands for longer focal length optical system. However the commensurate increase in the aperture to meet the practised F-number is constrained by issues pertaining to fabrication and testing, assembly and alignment, retention of optical elements position in the instrument structure, launch load and envelope. Therefore, the margin in the modulation transfer function available for various stages of development of a high resolution optical system to meet the final specification is less and becomes critical.

The critical nature of the modulation transfer function which is one among the performance metric of the optical system needs to be addressed at

various stages of development of a high resolution optical system. The development of an optical system is basically categorized as (1) design, (2) components fabrication, (3) assembly and alignment and (4) test and evaluation stages.

In the design stage, we have developed a baffle design method based on a combination of the results of optical design software and analytical relations formulated herein. The method finds the exact solution for the baffle parameters of a modified Ritchey–Chretien telescope by iteratively solving the analytical relations using the actual ray coordinates of the telescope computed with the aid of an optical design software. The baffle system so designed not only blocks the direct rays of stray light reaching the image plane but also provides minimum obscuration to imaging light. Based on the iterative method, we proposed a baffle design approach for a rectangular-image-format telescope. We have verified the performance of the baffle design method through a numerical experiment using a realistic modified Ritchey–Chretien telescope model with a standard light analysis tools. Also the baffle design method is implemented in the planned next in series optical system of cartography satellite of Indian Space Research Organisation.

The optical elements (mirrors) are held in position in the telescope using mechanical mounts/structures. Flexure mounts are being used to reduce the distortions on the mirror surface that arise due to deformations of mechanical interfaces. The mirror and the flexure called *mirror assembly* are held together with an adhesive. To investigate the procedures in the assembly stage, we have prepared samples and carried out experiments in detail, for the known space qualified adhesives, to understand the adhesive-induced stress and other effects on space-borne optical components. Cases and parameters that are not reported elsewhere for adhesives Epotek-301 and 3M 2216 B/A gray are experimentally studied and discussed here. We have also attempted from the results, with the known properties of various space-qualified adhesives, to establish an empirical relation that helps to identify adhesives for space borne high resolution optics.

It is necessary not only to evaluate but also to understand the degradation of performance of a space borne optical system that occurs during various tests and operations. We have proposed and designed a wavefront analyser based on

Shack-Hartmann wavefront sensor to test the optical system in an electro optical module. We have analysed the effect of parameters of the wavefront sensor on the accuracy of wavefront determination. During the development of wavefront sensor, while addressing experimentally the effect of parameters on wavefront retrieval accuracy, we have proposed and demonstrated new methods of determination of focal length of microlens array using (1) spherical and (2) plane wavefronts. Those methods also facilitate in the axial positioning of the microlens array in the wavefront sensor configuration; hence improves the determination accuracy of wavefront. The wavefront sensor which is developed is demonstrated by evaluating the wavefront that emerges from a simulated-telescope and the results are compared with that of the standard interferometer which is configured for an *in situ* measurement. The comparison of results after calibration showed a close match between the two methods and hence supporting the utility of the proposed wavefront sensor for the testing.

The work reported here in terms of methods, hardware development and experimental studies demonstrate that there is an overall improvement on the development of high resolution optical systems for earth observation.

Table of Contents

Certificate

Declaration

Acknowledgements

Abstract

List of Figures

List of Tables

Abbreviations

Chapter 1	Introduction	1
Chapter 2	Design of stray light shields for the optical system	23
2.1	Introduction	23
2.2	Design of baffles	25
2.2.1	Direct method	26
2.2.2	Iterative method	33
2.3	Baffle design for a rectangular image format	35
2.4	Design of vanes for the primary mirror baffle	41
2.5	Summary	44
Chapter 3	Design, Modelling and Evaluation of stray light shield for a modified RC telescope	47
3.1	Introduction	47
3.2	Numerical example	47
3.3	Design of baffles	48
3.4	Modelling of baffles	52
3.5	Modelling of source and detector	54
3.6	Stray light analysis	54
3.7	Imaging performance analysis	59
3.8	Summary	60

Chapter 4	Direct bonded mounting of optical component: An experimental study	63
4.1	Introduction	63
4.2	Direct bonded optical assembly	66
4.3	Experimental details	67
4.3.1	Sample details	67
4.3.2	Evaluation method	73
4.4	Results	77
4.4.1	Surface distortion due to Epotek-301	77
4.4.2	Surface distortion due to 3M 2216 B/A gray	79
4.4.3	Lap shear strength and out-gas properties	82
4.5	Discussion	83
4.6	New method to reduce surface distortion	87
4.7	Summary	87
Chapter 5	Design of wavefront sensor for optical system testing at EOM	89
5.1	Introduction	89
5.2	Principle of SH WFS	91
5.3	Polynomial representation of wavefront	94
5.3.1	Zernike polynomial representation	95
5.4	Proposed test scheme at EOM	99
5.5	Design of SH WFS	100
5.6	Summary	107
Chapter 6	Development and verification of wavefront sensor for optical system testing at EOM	109
6.1	Introduction	109
6.2	Methods of MLA characterization	109
6.3	Spherical wavefronts method	110
6.3.1	Theory	112
6.3.2	Error analysis	117
6.3.3	Measurement procedure	117
6.3.4	Results and Discussion	120

6.4	Plane wavefront method	123
6.4.1	Theory	124
6.4.2	Error analysis	126
6.4.3	Measurement procedure	127
6.4.4	Results and Discussion	129
6.5	Development of SH WFS	134
6.6	Evaluation of optical system with the SH WFS	134
6.7	Summary	143
Chapter 7	Summary and Conclusion	145
7.1	Summary and Key results	145
7.2	Future work	149
	References	151
	Appendix 1	159
	Appendix 2	173
	Publications based on the thesis	177
	Author's Biography	

List of Figures

Fig. no	Caption	Pg. no
1.1	Definition of ground sampling distance	2
1.2	Aperture of optical system for various resolutions	12
1.3	Diffraction limited MTF of optical system for various resolutions	13
1.4	Comparison of MTF of an obscured and an unobscured system	14
1.5a	Configuration of anobscured axially centred two mirror system	16
1.5b	Configuration of an unobscured three mirror system	16
1.5c	Configuration of an obscured three mirror system	17
1.5d	Configuration of an obscured catadioptric system	17
1.6	Schematic depiction of MTF	18
1.7	Depiction of reduction of the MTF in the presence of stray light	19
2.1	Optical layout of a modified RC telescope	26
2.2	Optical layout pertinent to primary mirror baffle parameters	28
2.3	Optical layout pertinent to secondary mirror baffle parameters	30
2.4	Optical layout for the determination of ray “c” parameters	33
2.5	Definition of skew ray at pupil	37
2.6	Front view of the primary mirror baffle	38
2.7	Front view of the secondary mirror baffle	39
2.8	Side view of the secondary mirror baffle	40
2.9	Isometric view of the secondary mirror baffle	40
2.10	Placement of vanes in the primary mirror baffle	43
3.1	Definition of a rectangular image format	48
3.2	Convergence of iteration of baffle parameters	48
3.3	Baffles modelled using ZEMAX [®] NSC	52
3.4	Model of the primary mirror baffle with vanes	53
3.5	Model of the secondary mirror baffle	53
3.6	Non sequential ray trace for the FOV 0.5°	55
3.7	Non sequential ray trace for the FOV 11°	56
3.8	Plot of normalized light power reaching the detector plane with and without the primary baffle vanes	58

3.9	Plot of non-uniformity of light across the image plane for ($\pm 0.6^\circ$ cross track , 0.18° along track)	58
3.10	Modelling of the effective obscuration telescope with baffles	59
3.11	Plot of comparison of MTF (Tangential) for various cases	60
3.12	Plot of comparison of MTF (Sagittal) for various cases	60
4.1	Interferogram, surface plot, spot size and MTF for a free mirror	65
4.2	Interferogram, surface plot, spot size and MTF for a stressed mirror	65
4.3	1: 6 aspect ratio optical flat	68
4.4	1: 10 aspect ratio optical flat	68
4.5	Optical flat with the mount	68
4.6	Schematic of the relief bond pad on the mount	69
4.7a	Schematic of the lap shear sample	69
4.7b	Photograph of lap shear and outgas samples	69
4.7c	Details of the lap shear test sample	70
4.8	Experimental set up for the surface figure evaluation of optical assembly	73
4.9	Optical flat resting bed on the experimental setup	74
4.10	Photograph of the experimental setup for the surface evaluation	74
4.11	Details of hot soak	75
4.12	Details of thermal cycle	75
4.13	Details of cold soak	76
4.14	Optical flat in free condition	81
4.15	Optical assembly with Epotek-301 upon cure	81
4.16	Optical assembly with Epotek-301 upon thermal exposure (test at RT)	81
4.17	Optical assembly with 3M 2216 B/A gray upon cure	82
4.18	Optical assembly with 3M 2216 B/A gray upon thermal exposure (test at RT)	82
4.19a	Surface distortion phenomenon of optical assembly upon cure	85
4.19b	Surface distortion phenomenon of optical assembly upon thermal exposure and test at RT	85
5.1	Sketch of the Fizeau interferometer test of optical system	89
5.2	Image spot corresponds to sampling of incident wavefront by the SH WFS	92

5.3	Displacement of image spot due to change of local wavefront tilt	93
5.4	Contour plot of various Zernike polynomials modal coefficients	96
5.5	Outline of the proposed EOM test set with the SH WFS	100
5.6a	Surface plot of wavefront deformation at zero 'g'	101
5.6b	Surface plot of a trefoil deformation of wavefront	102
5.6c	Surface plot of an astigmatic deformation of wavefront	102
5.7	Image spot spread and allowable image spot displacement and	104
5.8	Image spot displacement for the expected values of modal coefficients	105
6.1	Proposed experimental configuration for the spherical wavefront method	111
6.2	Image spot at the MLA focal plane for a spherical wavefront	112
6.3	Sketch of the interferometer based experimental setup for spherical wavefront method	118
6.4	Photograph of the interferometer based experimental setup for spherical wavefront method	119
6.5	Centroid estimation error σ_c for various image spot measurements averages	120
6.6	Plot of intensity spread measure for various image plane separations	121
6.7	Estimated focal length for various TS relative measurement positions	122
6.8	Image spots at the focal plane of MLA for a plane wavefront	123
6.9	Position of light spot for various angles of incident plane wave at the MLA focal plane	124
6.10	Schematic of interference of light between tilted plane surfaces	125
6.11	Schematic of experimental set up of the plane wavefront method	127
6.12	Photograph of experimental set up of the plane wavefront method	128
6.13	Typical measured tilt θ between the plane wavefront and the MLA (Inset: interference fringes)	130
6.14	Sensitivity of the plane wavefront method	131
6.15	Sensitivity of the spherical wavefront method	131
6.16	Focal length of each microlens	132
6.17	Focal length of the MLA for various incident plane wavefront angles	133
6.18	Photograph of the developed SH WFS	134

6.19	Quality of wavefront emerging from the simulated telescope	136
6.20	Sketch of the SH WFS configuration for the evaluation of telescope	136
6.21	Photograph of the SH WFS configuration for the evaluation of telescope	137
6.22	Quality of the wavefront emerging from the plano-convex lens	138
6.23	<i>In situ</i> verification of the SH WFS with a Fizeau interferometer	141

List of Tables

Table No	Caption	Pg. no
1.1	Johnson criteria for visual discrimination	6
1.2.	Some of the world-wide high resolution optical imaging systems for earth observation	7
1.3	Parameters of a typical imaging sensor for various GSDs	10
1.4	Diameter of optical systems of various satellites	11
1.5	Comparison of refractive and reflective optical system configuration	15
3.1	Comparison of parameters of baffles	49
3.2	Comparison of parameters of secondary mirror baffle	50
3.3	Dimensional details of primary mirror baffle with vanes	51
3.4	Ray trace for the field angles in the larger FOV direction	56
3.5	Ray trace for the field angles in the smaller FOV direction	57
3.6	Ray trace for the field angles in the diagonal FOV direction	57
4.1	Properties of adhesive Epotek-301	71
4.2	Properties of adhesive 3M 2216 B/A gray	72
4.3	Acceptance criteria on various parameters	77
4.4	Surface figure of the bonded optical assembly with Epotek-301	78
4.5	Surface figure of the bonded optical assembly with 3M 2216 B/A gray	80
4.6	Results of mean value of lap shear strength, CVCM and TML	83
4.7	Comparison of the salient properties of adhesives	86
5.1	Definition of the lower-order Zernike circular polynomials	98
5.2	First derivatives of the lower-order Zernike circular polynomials	99
5.3	Details of the MLA and the CCD for the SH WFS	106
5.4	Expected uncertainty in the retrieved Zernike coefficient	107
6.1	Catalogue parameters of MLA and CCD camera	118
6.2	Measured parameters of the MLA	133
6.3	Zernike polynomial coefficients retrieved with the SH WFS (vibration isolation condition)	140

6.4	Zernike polynomial coefficients retrieved with the SH WFS (vibration non- isolation condition)	141
6.5	Zernike polynomial coefficients retrieved with the interferometer (vibration isolation condition)	142
6.6	Zernike polynomial coefficients retrieved with the interferometer (vibration non-isolation condition)	143

ABBREVIATIONS

a.u – Arbitrary unit
BC – Babinet Compensator
CCD- Charge Coupled Device
CTE – Coefficient of thermal expansion
CVCN – Collected Volatile Condensable Material
DM - Direct Method
DN- Digital Number
EOM – Electro Optical Module
FEM – Finite Element Model
FOV – Field of View
F# - F-number
GSD – Ground Sampling Distance
IFOV- Instantaneous Field of View
IGFOV- Instantaneous Geometric Field of View
IM - Iterative Method
LTE- Low Thermal Expansion
MLA – Microlens Array
MS – Multi-spectral
MTF – Modulation Transfer Function
NSC – Non-Sequential components
PAN - Panchromatic
PSF – Point Spread Function
PSI – Polarization Shearing Interferometer
PV – Peak to Valley
RC- Ritchey Chretien
RH – Relative Humidity
RMS – root mean square
RSS – root sum square
RT – Room Temperature
SH WFS – Shack Hartmann Wavefront sensor

SNR – Signal to Noise Ratio
T_g – Glass Transition Temperature
TML – Total Mass Loss
TS – Transmission Sphere
TDI – Time Delay Integration
UDA – User Defined Aperture
WFE – Wavefront error

CHAPTER 1

INTRODUCTION

Optical system is one of the major elements of a sensor for remote sensing. Remote sensing is acquiring of information about an object or phenomenon without making physical contact with it. It is also acquiring knowledge of the object or phenomenon of interest that may not be directly measured but related through some other variable that is being observed. With the launch of the first satellite *Sputnik* on October 4, 1957, a whole new world of opportunities opened up and the era of space based remote sensing began when the first photograph of the earth was taken by US satellite Explorer-6 in August 1959. Similarly, camera on *TIROS-1* satellite launched in 1960 provided the synoptic view of the earth and its surroundings for meteorological applications. *Landsat* satellite launched in 1972 demonstrated the power and versatility of multi-spectral imagery for observing the earth for purposes of monitoring its natural and manmade features over time. Since then, many applications of remote sensing have become important in management of the earth's health and the utilization of its resources. A large number of space missions carrying variety of sensors have been launched providing priceless information leading to the establishment and operationalization of a large number of applications of the remote sensing technology. The earth observation satellites are categorized as low (> 100 m), medium (10-100 m) and high (< 10 m) resolution. The term *resolution* defines the smallest discernable physical unit of an observed signal by an onboard sensor

(Kramer, 2002). The resolution of an optical imaging system primarily categorized in terms of *spatial*, *spectral*, *temporal*, and *radiometric* parameters.

Spatial resolution represents the detail discernible in an image of the sensor and refers to the size of the smallest possible object (feature) that can be detected. Instead of spatial resolution more convenient way to define the spatial domain parameter of sensor is ground sampling distance d . The GSD is the geometrical projection of the smallest element (pixel) of detector at the focal plane of optical system on ground (shown in Fig 1.1).

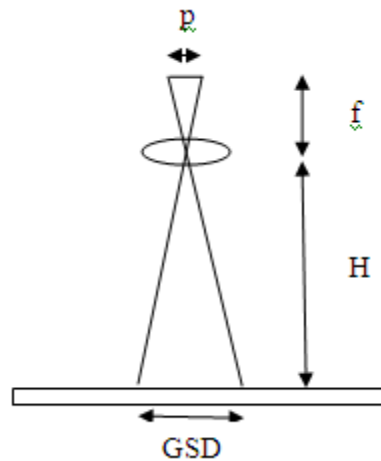


Fig. 1.1 Definition of ground sampling distance.

It is also represented in angular terms as θ instantaneous field of view or instantaneous geometric field of view. The GSD d is expressed in terms of the optical system focal length f , size of the detector pixel p and the satellite altitude H as,

$$d = \theta H \quad (1.1)$$

and

$$\theta = \frac{p}{f} \quad (1.2)$$

The sensor is required not only to sample smaller area on ground but also to carry out smaller sampling over a large area on ground. Multiple GSDs make the swath of the sensor. The swath is defined as the maximum number of GSD elements that an imaging system able to view in a given instant. The swath is represented by the FOV of the sensor.

Spectral resolution describes the sensor's ability to distinguish different portions of the electro-magnetic radiation spectrum. Some sensors are sensitive to visible light only, while others can also capture any other portion of the electromagnetic spectrum. The portions (ranges) of the spectrum to which an instrument is sensitive are referred to as its bands. Performance of the sensor in spectral domain is represented by number of bands, central wavelength and width of each band. A sensor can have multiple bands, and bands can be of varying widths. Spectral resolution refers to both the number and width of the bands for a given sensor.

Temporal resolution is the time interval at which a sensor images, or can image, exactly the same area at the same viewing angle a second time. This is important because many applications depend on observing changes in phenomena over time. The time factor in imaging is particularly important in case of visible sensors where ability to obtain imagery of a particular area of interest is uncertain due to cloud cover. The platform on which a sensor is mounted is the greatest determinant of that sensor's temporal resolution. In the

case of a satellite based systems, the temporal resolution is equal to the revisit period which refers to the length of time it takes for a satellite to complete one entire orbit cycle. The revisit period of a satellite sensor is usually several days. However, because of some degree of overlap in the imaging swaths of adjacent orbits and the increase in this overlap with increasing latitude, some areas of the earth tend to be re-imaged more frequently. Also, some agile satellite systems are able to point their sensors to image the same area between different satellite passes separated by periods from one to five days. Thus, the actual temporal resolution of a sensor depends on a variety of factors, including the satellite/sensor capabilities, the swath overlap and latitude. In general, the larger the swath, hence larger the FOV, the higher is temporal resolution.

The ability to collect imagery of the same area of the earth's surface at different periods of time is one of the most important elements for applying remote sensing data. Spatial and spectral characteristics of features may change over time and these changes can be detected by collecting and comparing multi-temporal imagery. For example, during the growing season, most species of vegetation are in a continual state of change and our ability to monitor those subtle changes using remote sensing is dependent on when and how frequently we collect imagery. In addition, the changing appearance of a feature over time can be used to distinguish it from near-similar surrounding. High temporal resolution is required to monitor short-lived phenomena like cyclones, floods, oil slicks, strategic activities etc.

While the arrangement of pixels describes the spatial structure of an image, the radiometric characteristics describe the actual information content in an image. Every time an image is acquired by a sensor, its sensitivity to the magnitude of the electromagnetic energy determines the radiometric resolution. The radiometric resolution of an imaging system describes its ability to discriminate very slight differences in energy. The finer is the radiometric resolution of a sensor the more is the sensitive to detect small differences in reflected or emitted energy. In terms of the sensor parameters, it is the number of unique values that can be recorded by a sensor system when measuring reflected or emitted radiation. Typically, this ranges from 8 to 14 bits, corresponding to 256 levels of the gray scale and up to 16,384 intensities or "shades" of colour, in each band. The radiometric also depends on the instrument noise. The noise of the sensor is defined by its signal to noise ratio.

The classifications of spatial resolution have been changing over the years with the advent of new enabling technologies. Nevertheless we classify here the spatial resolutions as low spatial resolution for the GSD > 100m, medium resolution for the GSD 10 to 100 m and high resolution for the GSD < 10 m. Nowadays spatial resolution of ≤ 1 m are categorized as very high resolution system. It is widely adopted that high resolution satellite refers to the high spatial resolution. The high resolution wide spectral band imaging systems are found applications in target discrimination.

The visual discrimination is arbitrarily divided (Johnson, 1958) into four categories as detection, orientation, recognition and identification. The results of

Johnson's report can be seen in the book written by Holst G. C, (2008). The spatial frequency of observation required for the classification under any of the visual discrimination category is given in table 1.1.

Table 1.1: Johnson criteria for visual discrimination

Discrimination level	Meaning	Spatial frequency (cycles/ minimum dimension)
Detection	Ability to find an object of interest	1.0
Orientation	Ability to find an object symmetricity and its orientation	1.4
Recognition	Ability to find class to which the object (car, truck)	4.0
Identification	Ability to find type of object within the class (Model of the car)	6.4

Table 1.2 gives the spatial resolution of optical imaging system for the earth observation launched/planned worldwide. It is obvious from table 1.2 that, over the years with the advent of newer technologies, there is a growing demand for higher spatial resolution optical system for the earth observation. The limiting resolution for observing the earth through atmosphere i.e., from space is estimated as 4.6 cm (Freid, 1966). One can expect that the demand for the spatial resolution of a classical earth observation sensor may eventually approach the limiting resolution in due course of time.

Table 1.2: Some of the world wide high resolution optical imaging systems for earth observation.

Satellite	Sensors onboard (GSD m)
IRS 1C, 1D Resource sat 1, 2	PAN (5.8), LISS-3 (23.5), MS (5.8)
SPOT-4	PAN (10), MS (20)
IKONOS 2	PAN (1), MS (4)
KOMPSAT-1	PAN (6.6)
KOMPSAT-2	PAN (1), MS (4)
EROS-A1	PAN (1.8)
EROS-B	PAN (0.7)
QuickBird 2	PAN (0.61), MS (2.44)
SPOT-5	PAN (2.5), MS (10)
Formosat-2	PAN (2), MS (8)
CARTOSAT-1	PAN (2.5)
CARTOSAT-2,2A,2B	PAN (0.8)
TES	PAN (1)
Worldview-I	PAN (0.5)
Geoeye-1	PAN (0.41), MS (1.65)
Pleaidess-1	PAN (0.7), MS (2.8)

The IGFOV for a diffraction-limited system can be obtained from Rayleigh criteria. Rayleigh has proposed that two close by objects can be just distinguished separately if the angular separation $\Delta\theta$ of central peaks of the images is such that the central peak of one image falls upon the first minimum of the other. It is expressed in radians as,

$$\Delta\theta = \frac{1.22\lambda}{D} \quad (1.3)$$

where D is the aperture of the optical system and λ is the wavelength of light. This criterion for an aberration free optical system and source of equal brightness corresponds to a 27% fall in the intensity between the two peaks. The GSD or IGFOV can also be obtained from Sparrow criteria. It defines the limit of resolution when the combined intensity pattern of image of the two sources has just no minimum between the two centres. This condition occurs when

$$\Delta\theta = \frac{\lambda}{D} \quad (1.4)$$

The GSD of the optical system is obtained by multiply Eq. (1.3) or Eq. (1.4) with the satellite altitude H . Further, the spatial resolution of sensor depends on the PSF. The PSF is the spread of light intensity in the image of a point source. The PSF is complex to be defined as a metric of sensor for practical purposes. Hence, the imaging performance of an optical system is commonly specified by the MTF. The MTF is a measure of degradation of amplitude of various sinusoidal frequency components that make up the object during image formation. Due to this there could be two sensors with the same GSD but significantly different spatial resolution. The performance of earth observation system is primarily dictated by the product of MTF and SNR. The MTF and the irradiance (signal) of the optical system are inverse function of the ratio of focal length to aperture i.e., $F\#$ (Smith, 2000).

Design of preliminary optical imaging system starts with the definition of requirements satisfying the applications; in terms of the sensor parameters namely resolutions, SNR and MTF under the specified conditions (Slater,

1980). The amount of optical power I in watts reaching the detector can be found out using the relation,

$$I = \pi / 4 \quad D^2 W_s \eta \Delta \lambda \theta^2 \quad (1.5)$$

where D - diameter of collecting optics (cm), f - focal length of optics (cm), W_s - light radiance ($\text{W}/\text{cm}^2\text{-str-}\mu\text{m}$), η - optical efficiency, $\Delta \lambda$ - spectral bandwidth (μm) and θ - IGFOV (rad). The sensor collects light energy E (Joules) over a time T_{int} called integration time. During the integration time the sensor IGFOV moves completely to the next resolution element. In the case of a pushbroom scanner, T_{int} corresponds to time taken by sensor to move from one to another ground sampling element completely.

$$T_{int} = \frac{GSD}{V_s} \quad (1.6)$$

where V_s is the ground track velocity of satellite. The energy E collected,

$$E = I T_{int} \quad (1.7)$$

As can be seen, for a high spatial resolution system the IGFOV will be small and the signal reaching the detector will reduce drastically as per the square relationship. In addition, there is commensurate reduction in the integration time further aggravating the situation. To compensate one has to go for smaller F# (larger diameter optics) and/or wider spectral bands (e.g. panchromatic). Strategies like noon orbits, step and stare scanning and TDI are used to maximize the E . The MTF of sensor depends on F#, wavelength and spatial frequency of

operation (detector pitch p). Smaller the $F\#$ higher is the MTF for given wavelength and spatial frequency. The SNR of the system is depend upon the overall system noises arising from photon noise, detector noise, thermal noise, quantisation noise and the system engineering noise. The desirable goal of a sensor design is to achieve a near photon noise limited SNR and a near diffraction limited MTF at nyquist spatial frequency. The parameters for a typical remote sensor of $F\#$ 4 operating at 800 km attitude with swath of 50 km and detector pixel size of 0.007 mm for different spatial resolutions (GSD) have been worked out and given in table 1.3.

Table 1.3: Parameters of a typical imaging sensor for various GSDs

Parameter	GSD (m)				
	10	5	2	1	0.25
IGFOV (μrad)	12.5	6.25	2.5	1.25	0.31
Focal length f (mm)	560	1120	2800	5,600	22,400
Optics Aperture D (mm)	140	280	700	1,400	5,600

From table 1.3, the increase in spatial resolution requires longer focal length for a given detector pixel pitch. In order to maintain the $F\#$, hence the MTF, of the optical system, the diameter of optics has to be increased proportionately. The complexity involves in realization of large diameter optics increases manifold (Fender, 2000). When there is an increase in spatial resolution, dwell time and solid angle over which light energy available for the pixel to collect reduces. However the shortcoming of light energy collection can be

overcome either by asynchronous imaging (step and stare) or by usage of time delay integration techniques (Joseph, 2003). The diameter and the F# of optical system used for various space borne electro optical systems are given in table 1.4.

Table 1.4: Diameter and F# of optical systems of various satellites

Satellite	Payload	Optics aperture (mm)	GSD (m)	F#
IRS 1C, 1D Resourcesat 1, 2	PAN	240	5.8	4.5
	LISS-3	72	23.5	4.5
SPOT HRV	PAN	379	10	3.5
Cartosat-1	PAN	500	2.5	4
TES	PAN	560	1	7
KOMPSAT-2	PAN	600	1	15
IKONOS-1	PAN	700	0.8	14.2
Cartosat-2,2A,2B	PAN	700	0.8	8
Pleaidies-1	PAN	650	0.7	20
GEOEYE-1	PAN	1100	0.41	12

In the past, smaller F/# (typically F/4) optical systems were adopted to have an adequate margin on the MTF and the SNR with respect to the final specification (Joseph, 1996). The increase in spatial resolution demands for longer focal length optical system. However, commensurate increase in the aperture to meet the practised F/# is constrained by issues pertaining to fabrication and testing, assembly and alignment, retention of optical elements position in the instrument structure, launch load and envelope (Kasturirangan, 2004; Michaelis. et al, 1998). All above factors govern the configuration of the optical system and hence the realization of aperture of optics. The trend of optical aperture adopted

for various resolutions are shown in Fig. 1.2. There is a shift in criteria adopted for deciding the aperture of the optical system. The aperture of the optical system for a very high resolution optical system is being arrived at using either Rayleigh at upper bound or Sparrow criteria at lower bound. It is obvious from Fig. 1.2 that there is a vast difference in aperture of optical system arrived at by the past trend and by the present criteria. Therefore, there is also a vast difference in their F#.

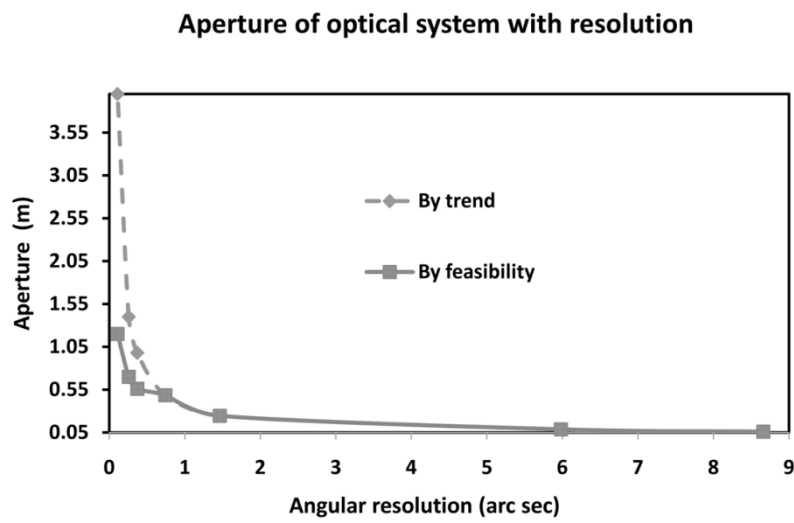


Fig. 1.2. Aperture of optical system for various resolutions

The diffraction limited MTF of optical system computed with the aperture from the past and the present is shown in Fig. 1.3. It can be noticed in Fig. 1.3 that the diffraction limited MTF of present system is less approximately by 60% at the near mid spatial resolution of operation as compared to the focal ratio adopted for optical systems realized in the past. Therefore, the margin available on the MTF for various stages of the development of high resolution optical system to meet the final specification is less and becomes critical.

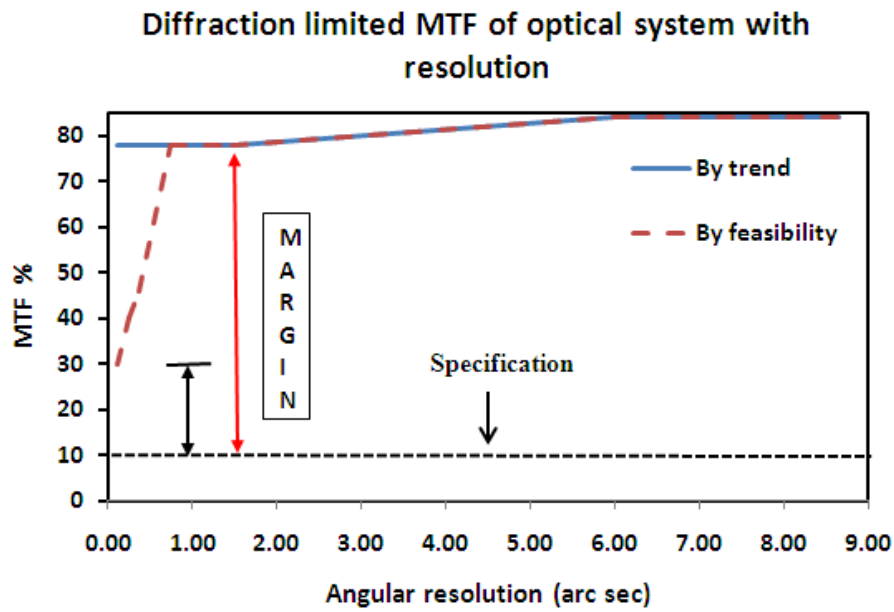


Fig. 1.3. Diffraction limited MTF of optical system for various resolutions

The critical nature of MTF which is one among the performance metric of the system needs to be addressed at various stages of the development. The development of optical system is basically categorized as (1) design, (2) components fabrication, (3) assembly and alignment and (4) test and evaluation stages. The objective of this research work is outlined as,

(1) To investigate the procedures and realisation aspects involved in the development of the optical system namely, design, assembly and alignment, and testing that having impact on the imaging performance.

(2) To identify the present limitations on the procedures and realisation aspects.

(3) To devise techniques that will help to eliminate or to minimize the degradation of the imaging performance during the various development stages of the optical system.

(4) To devise a compatible method to evaluate the imaging performance of the optical system at any stage of the EOM development.

In the design stage, the starting configuration of the optical system is arrived at from the salient specifications. In general, the optical system design is categorized under three broad classifications namely refractive, reflective and catadioptric types. Advantages and disadvantages of the refractive and the reflective system are given in the table 1.5. It is clear from the table 1.5 that the configuration of the optical system for a high resolution wide spectral band broadly converges to the reflective type (Cawthorne, 2008; Lamard, 2004; Simonetti, 2006). The reflective types are further categorized as an obscured and an un-obscured system (Wilson, 2007; Korsch, 1980). The un-obscured optical system configuration has more light gathering power and more diffraction limited MTF than that of the obscured system. The MTF for an unobscured and obscured (linear obscuration of 0.3 and 0.8) system are shown in Fig. 1.4.

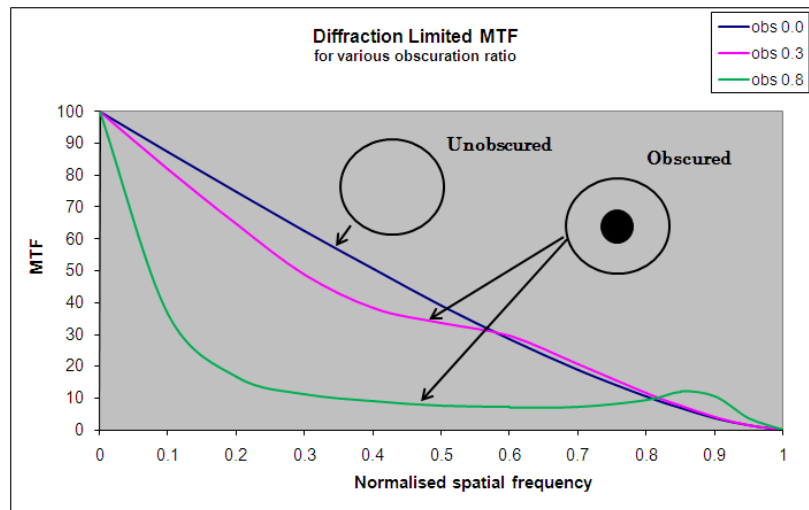


Fig. 1.4 Comparison of MTF of an obscured and unobscured system

Table 1.5: Comparison of refractive and reflective optical system configuration

Refractive system	Reflective system
Advantages	Advantages
1. Lens systems though multi-element, they are compact.	1. Long focal length system can be achieved with fewer components.
2. More number of variables are available for the correction of monochromatic aberrations	2. Front surface participates for the image formation. Rear surface material can be scooped out for light weighting. Also more freedom is available for holding the mirror.
3. Achievable FOV is large.	3. Light interacts with the front surface, hence no chromatic aberration, suits for wide spectral band
Disadvantages	Disadvantages
1. Light encounters the refractive index of the glass and hence it suffers from the chromatic aberration.	1. Less number of degrees of freedom is available for the aberration correction.
	2. Achievable FOV is small.
2. Suits only for a narrow spectral band even though large number of glasses available for chromatic aberration correction	3. Fewer mirrors are required to achieve a long focal length and hence each mirror requires a greater control on its parameters during fabrication, assembly, alignment and field operation.

However the un-obscured system occupies more volume and hence more weight in comparison to that of the obscured system. Axially obscured systems in general are symmetric about the optic axis and more suitable for agile spacecraft

missions. Further the limitation in the FOV of classical two mirror telescope can be overcome with the help of aft-optic lenses forming the catadioptric configuration or mirrors forming the multi-mirror configurations. Various optical system configurations used for high resolution optical systems are shown in Figs. 1.5a-d.

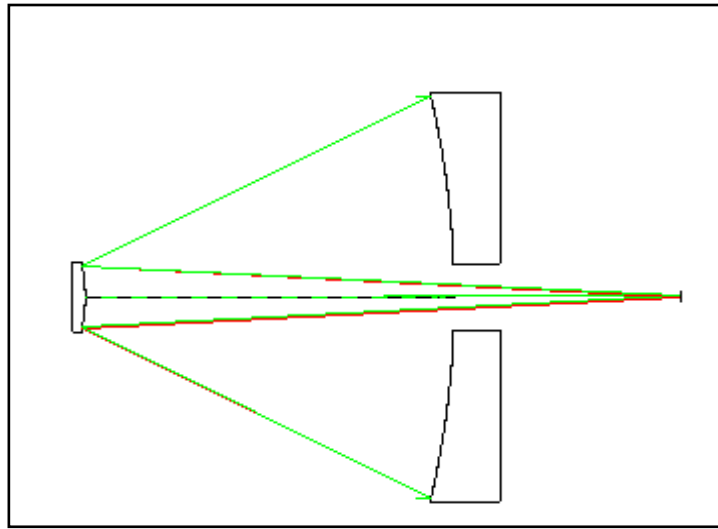


Fig. 1.5a Configuration of an obscured axially centred two mirror system

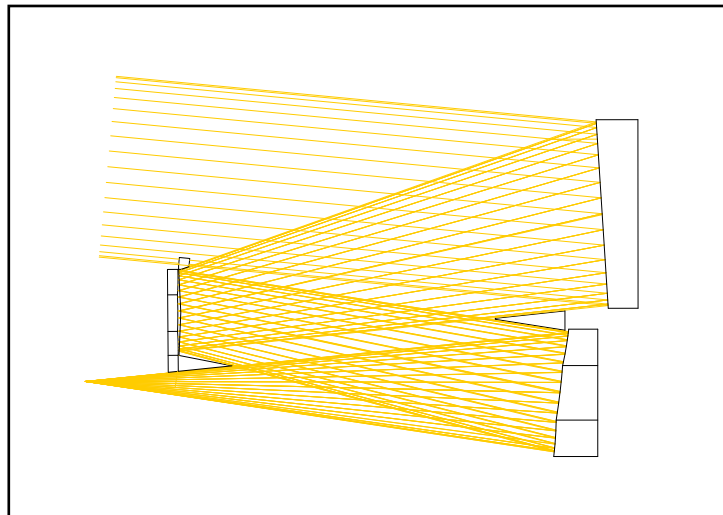


Fig. 1.5b Configuration of an unobscured three mirror system

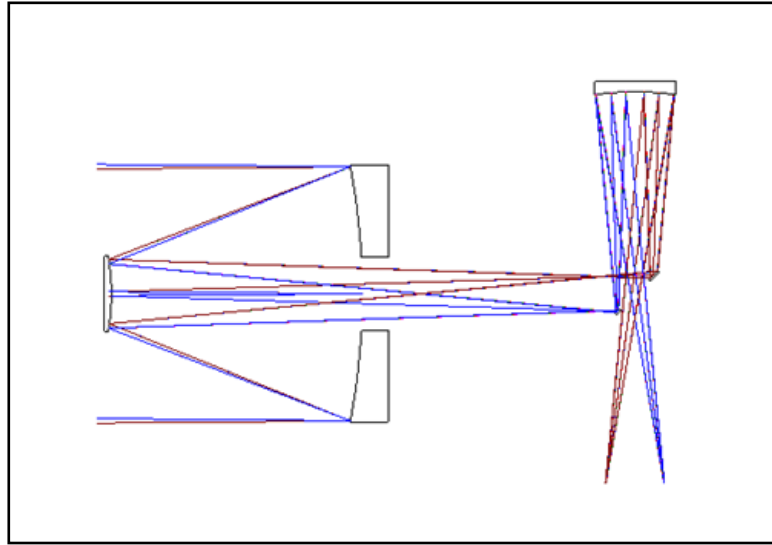


Fig. 1.5c Configuration of an obscured three mirror system

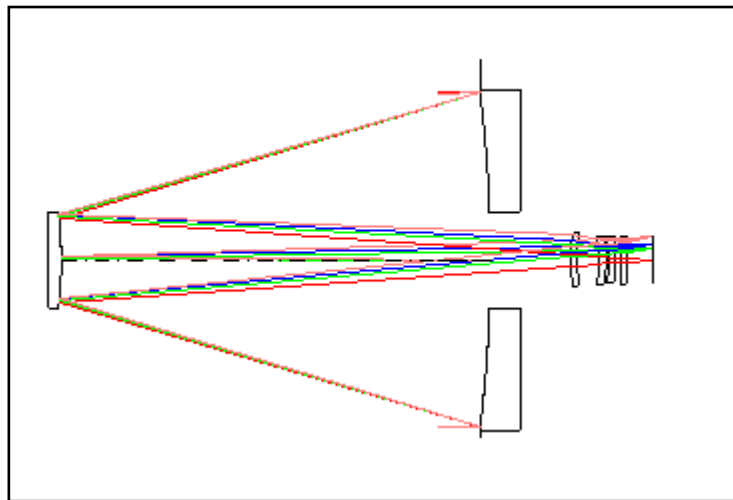


Fig. 1.5d Configuration of an obscured catadioptric system

The concept of MTF can be broadly visualized as a redistribution of energy from the bright to dark portion as shown in Fig. 1.6. The example that is shown in Fig 1.6, the light intensity of 500 (a.u) in the bright and zero (a.u) in the dark portions in the object are redistributed between the bright (300 a.u) and dark

(200 a.u) portions in the image while transferring various object details from the object space to the image space by the imaging system, hence the MTF of the optical system is 20%. The redistribution of intensity at the image plane of the optical system arises due to the image blur that is produced by various aberrations present in the optical system.

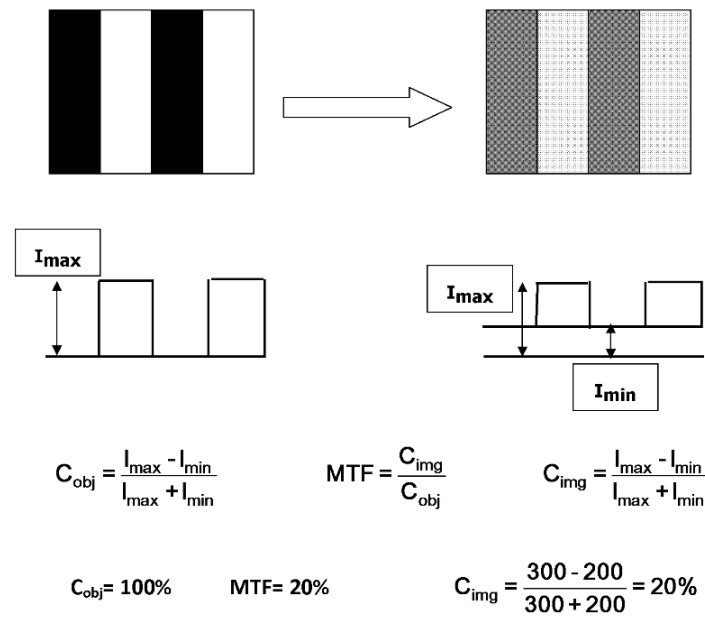


Fig. 1.6 Schematic depiction of MTF

In the design stage, it is always aimed at reducing the blur to the near diffraction limit besides meeting the other first order requirements like focal length, field of view, spectral band width etc. This is achieved by optimizing the various available degrees of freedom optical elements and systems namely, curvature, conic constant, inter spacing, etc. Besides the blur, the presence of stray light in the optical system degrades the image (Coleman, 1947; Fest, 2013; Harvey, 2010). For a case of an imaging system that forms an image with the MTF of 20% that is further reduced to 11% due to the presence of back ground

intensity arise from the stray light as shown in Fig. 1.7. It can also be noted that for the same intensity difference between bright and dark portion for a change of the back ground intensity (DC component) changes the system MTF from 20% to 11% as in Fig 1.7. Therefore, it is necessary to design optimum baffles to minimize the effect of stray light component on the MTF.

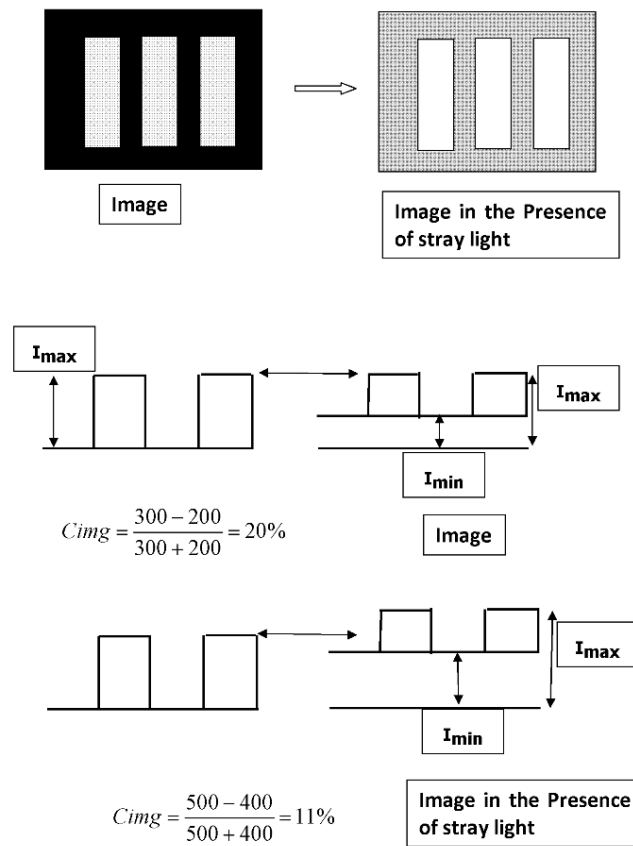


Fig. 1.7 Depiction of reduction of the MTF in the presence of stray light

The assembly and alignment stage of the optical system follows the fabrication of individual components. Individual optical components of the optical system are required to be positioned at the design coordinates in the instrument structure. In an high resolution optical systems, the positional tolerances of the

optical components are stringent requiring rigid fixing of optical components. Different types of mounting configurations are available.

1. Seat and retainer mount: It is the classical means of mounting the optical element. This method offers good accuracy and stability at the expense of high stresses in the metal-glass interface.

2. Direct bonded: It is a simple way of mounting and allows to achieving a semi-kinematic mounting configuration using mechanical flexures.

Any type of mountings of optical components is primarily concerned with maintaining the position of the component in the optical system besides not distorting the optical surface. Misalignment and surface distortion of the optical components in an optical system reduce the MTF.

The testing of individual optical component (West et al., 1992) as well as the complete aligned optical system is essential (Stahl, 2011). The high resolution optical system is aligned using the interferometer-aided reverse optimization method. The interferometer-aided reverse optimization allows one to align the optical system as well as test it. Interferometer based testing enables to evaluate the optical system in terms of wavefront. An optical system meant for space mission shall undergo various environmental tests namely vibration, thermo-vacuum, thermal tests to ensure its survivability while on ground, launch and in-orbit operations. It is required to evaluate the stability of the optical performance after every environmental test. The detailed evaluation of the optical system in terms of wavefront at every stage of the EOM development will enable not only to

confirm the performance stability but also to a certain extent identify the source of degradation.

In the chapter 2, we investigate the techniques used for design of baffles for a modified RC telescope to control the direct rays of stray light. We then develop a new method of baffle design overcoming the limitations of past methods of baffle design.

In the chapter 3, we show the design of baffle using a realistic numerical example of a modified RC telescope and analysis the performance of the baffle using ZEMAX[®] non-sequential mode.

In the chapter 4, we describe the study carried out to find the effect of space qualified adhesives on the surface of the optical assembly. We then discuss tests carried out and infer the results obtained.

In the chapter 5, we describe a method to test the optical system in an integrated EOM. We then carry out design and analysis of the wavefront sensor to perform the proposed test method.

In the chapter 6, we discuss the steps followed to develop the proposed sensor and test method detailed in chapter 5. We describe the demonstration of sensor to test a simulated optical system. We then show the cross-verification of the results of the sensor with a standard interferometer.

In the chapter 7, we present the summary of the key results obtained through this work and also we give the future scope of work.

CHAPTER 2

DESIGN OF STRAY LIGHT SHIELDS FOR THE OPTICAL SYSTEM

2.1 Introduction

The basic optical design of an imaging system aims at achieving a near diffraction limited performance by optimizing parameters of the optical elements viz. radius of curvature, conic and aspheric constant, inter-separation etc. The blur and hence, the reduction in the contrast of the image occurs due to the presence of optical aberrations in the optical system. During the design of optical system, it is targeted to correct the aberration to a minimum level such that the image blur is primarily due to diffraction. The performance of the optical system can be conveniently evaluated in terms of modulation transfer function. In calculating the modulation transfer function, it is presumed that the light is emanated from an object surrounded by dark background. In practical situation, the background of the object may not be dark but of varying gray shades starting from white to black. There is a likely chance that the light from the background reaching the image plane due to various means (direct rays, reflections and scattering) and thus giving rise to stray light. The stray light is the unwanted light emanating from light sources present outside the scene of interest that reaches the image plane. The presence of stray light reduces the image contrast and hence the image quality. The stray lights suppression system (baffles) shall be addressed and designed during the design stage of the optical system, because the presence of stray light modifies the nominal modulation transfer function of the optical system

estimated during the optical design and analysis. Also, it may not be possible to implement an optimal stray light control to suppress the stray light that is detected during the test and evaluation of the optical system. From the various available optical system design configurations, compact and less complex axially obscured RC telescopes with CCD at image plane are preferred for earth observation systems (Jung H et al, 2005; Simonetti et al, 2006) on an agile spacecraft mission. The RC telescope is modified with an addition of aft-optics to enhance the performance over a large image format, in other words, to meet the requirement of larger FOV (Smith, 1992; Epps et al, 1997; Shannon, 1997; Laikin, 2001; Kingslake et al, 2010). Axially obscured two-mirror based telescopes are more prone to light from outside the FOV directly reaching the image plane without encountering both mirrors. An efficient control of stray light is required for the radiometric fidelity and stable angular resolution (Treibitz et al, 2012). The design of stray light shields, however, is not a straight forward method with the available optical design software, although several stray-light programs are available to evaluate the performance of previously designed baffles. Eventually, the baffle design is done outside the software packages (Smith, 1998). In practice, the direct rays of stray light reaching the image plane are blocked with mechanical stops called baffles placed near each mirror. The baffle introduces additional obscuration to the imaging light. The axially obscured optical systems having *nyquist* sampling lying between low and mid spatial frequency inherently has the low MTF and the additional obscuration due to baffle leads to further reduction. It is desirable to have baffles blocking the stray light over the required FOV with minimum obstruction of the imaging light. The stray light shields are designed

with graphing method (Young, 1967) but arriving at exact solutions is difficult. Analytical methods of baffle design reported earlier (Prescott, 1998; Hales, 1994; Bely, 2003; Malacara et al, 2004) find exact solution for the baffle parameters over smaller FOV by solving formulated analytical expression of either second or fourth degree. The ray coordinate values substituted for the analytical relations are either approximate or valid for telescope of smaller FOV Cassegrain telescopes. Therefore, we have proposed here a method that is valid even for telescope of larger FOV. Our method differs from those methods by substituting actual ray coordinate values computed with optical design software for the analytical relations and solving it iteratively with linear analytical relations formulated herewith. Also our method utilizes the benefit of computation complexity, flexibility and accuracy of optical design software. Nowadays, optical design software based design optimization (Gregory, 1998) is an essential tool for almost every engineer and researcher aspiring for high productivity. Therefore the iterative method of baffle design proposed here is simple, easy to adapt and accurate.

2.2 Design of baffles

In axially obscured two-mirror-based telescopes light reaches the image plane directly without encountering both the mirrors, so it is necessary to have baffles to block the direct rays of stray light. The basic criterion for the two-mirror telescope baffle design is to block the direct rays of stray light and allow the unobscured-imaging rays without vignetting (preserve inherent image uniformity). Typically, it is satisfied with mechanical projection towards front side from the

vertex of each mirror of the telescope. The optical schematic of modified RC telescope system with typical primary and secondary mirror baffles is shown in Fig. 2.1.

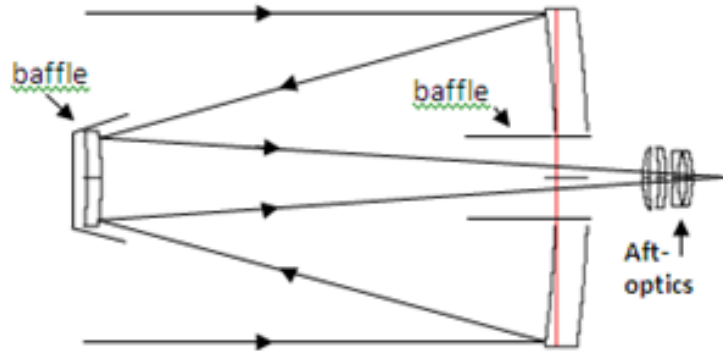


Fig. 2.1 Optical layout of a modified RC telescope

2.2.1 Direct Method (DM)

The fundamental principle of baffle design is to find the length and diameter of baffles that satisfies the basic criterion mentioned earlier. The method of baffle design, contrary to earlier methods, is based on combination of results of optical design software and analytical relation formulated herewith. The ray trace routine of optical design software computes angle and intercept height of the defined ray at a designated surface. The computed values of ray coordinates are substituted in the analytical expression to arrive at the baffle design. This method is simple and straightforward. Both baffles parameters are determined in two sequential steps.

Step 1: Determination of parameters of primary mirror baffle

Light rays from object at infinity with FOV $\pm \theta^\circ$ travel to telescope entrance pupil of semi-diameter R and reach the image plane (image height “ $2h$ ”) after reflection at primary and secondary mirrors, and refraction through aft-optics. In this discussion positive FOV is measure of angle in the counter-clockwise direction. The parameters required for the design of primary mirror baffle are shown in Fig. 2.2 (positive axis along arrow head of axis definition). The aim is to find Z_p (defines the location of the front end from the secondary mirror vertex plane) and Y_p (defines the semi-diameter of the front end cut-out) of the primary mirror baffle. The ray “a” originates from the positive edge of FOV of object and passes at the rim of entrance pupil of the telescope. It intersects at A_1 on the primary mirror and after reflection it strikes at B_1 on the secondary mirror (shown in Fig. 2.2). The reflected ray from the secondary mirror strikes at H_1 on the image plane after passing through the aft-optics. The ray “b” originates from the negative edge of FOV of object and passes at the edge of axial obscuration (shown in Fig. 2.2). It intersects at A_2 on the primary mirror and after reflection it strikes at B_2 on the secondary mirror. The reflected ray from the secondary mirror strikes at H_2 on the image plane after passing through the aft-optics.

The necessary conditions for primary mirror baffle are, (condition: 1) baffle should not block the ray segment L_1 of the ray a between secondary mirror and aft-optics and (condition: 2) baffle should not block the ray segment L_2 of the ray b between primary and secondary mirrors (shown in Fig. 2.2). Any ray segment L_i can be written in the form of straight line equation, $Y = m_i Z + c_i$, where, m_i is the slope ($\tan(\text{subtend angle of ray segment with optic axis})$) and

upward slope from secondary mirror vertex plane is indicated by +ve sign, c_i is the intercept height from optic axis of the ray segment at the vertex plane of secondary mirror. Hence,

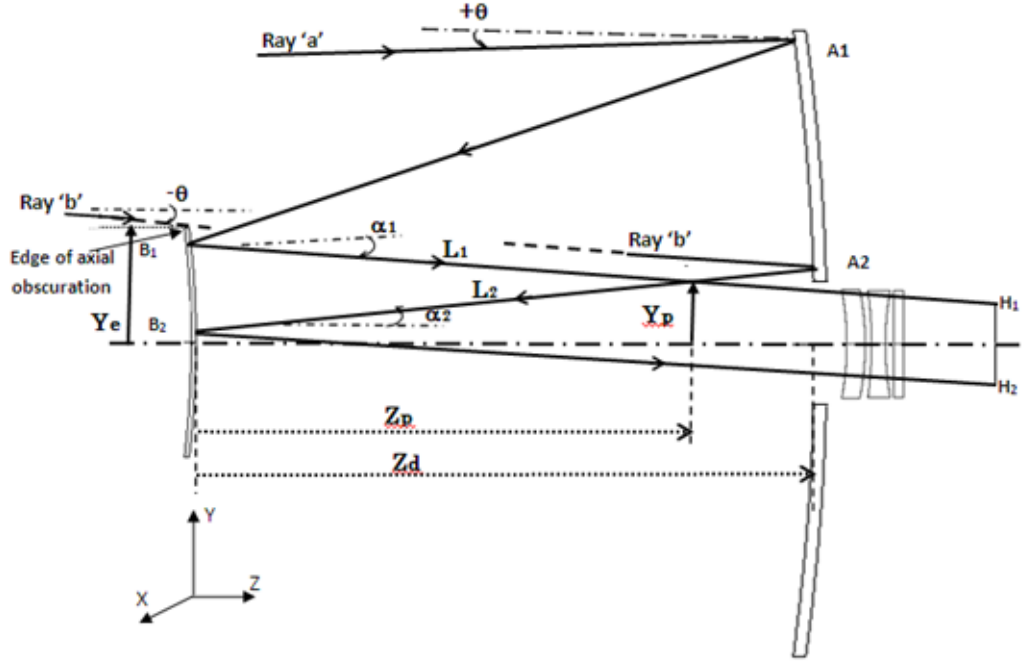


Fig. 2.2 Optical layout pertinent to the primary mirror baffle parameters

L_1 is written as,

$$Y = -m_1 \times Z + c_1 \quad (2.1a)$$

m_1 is the slope ($\tan(\alpha_1)$) of ray segment L_1 and c_1 is the intercept height from optic axis of the ray segment at the vertex plane of secondary mirror.

L_2 is written as,

$$Y = m_2 \times Z + c_2 \quad (2.1b)$$

m_2 is the slope [$\tan (\alpha_2)$] of ray segment L_2 and c_2 is the intercept height from optic axis of the ray segment at the vertex plane of secondary mirror.

The condition 1 and 2 are satisfied simultaneously at the intersection point of L_1 and L_2 . At the intersection point Eqs. (2.1a) = (2.1b) and also Z is denoted as Z_p . Hence,

$$Z_p = \frac{c_1 - c_2}{m_1 + m_2} \quad (2.2a)$$

When $Z=Z_p$ in Eq. (2.1a) then $Y=Y_p$, thus

$$Y_p = -m_1 \times Z_p + c_1 \quad (2.2b)$$

The coefficients defined in Eqs. (2.1a) and (2.1b) are computed with the optical design software in the following way. The coefficients m_1 and c_1 are computed by placing one dummy surface at zero distance from the secondary mirror after reflection in the sequential optical design data of the telescope. The unsigned output value of tangent angle and ray intercept for Y -axis for the ray a at that dummy surface computed through ray trace tool of optical design software is substituted for m_1 and c_1 respectively. The coefficients m_2 and c_2 are computed by placing one dummy surface at zero distance from the secondary mirror before reflection in the sequential optical design data of the telescope. The aperture stop is nominally located at primary mirror (hence also the entrance pupil). However, only for the computation of coefficients of m_2 and c_2 , it is placed at distance Z_a ($Z_a = Z_d$) in front of the primary mirror vertex and the ray height Y_e at entrance pupil for the ray b is r_s (semi-diameter of secondary mirror physical aperture;

larger than the clear aperture, defined by intercept of pupil rim ray of edge of FOV of object) in the optical design program. The unsigned output value of tangent angle and ray intercept for Y -axis for the ray b at that dummy surface computed through ray trace tool of optical design software is substituted for coefficients m_2 and c_2 respectively.

Step 2: Determination of parameters of secondary mirror baffle

The parameters required for the design of secondary mirror baffle are shown in Fig. 2.3.

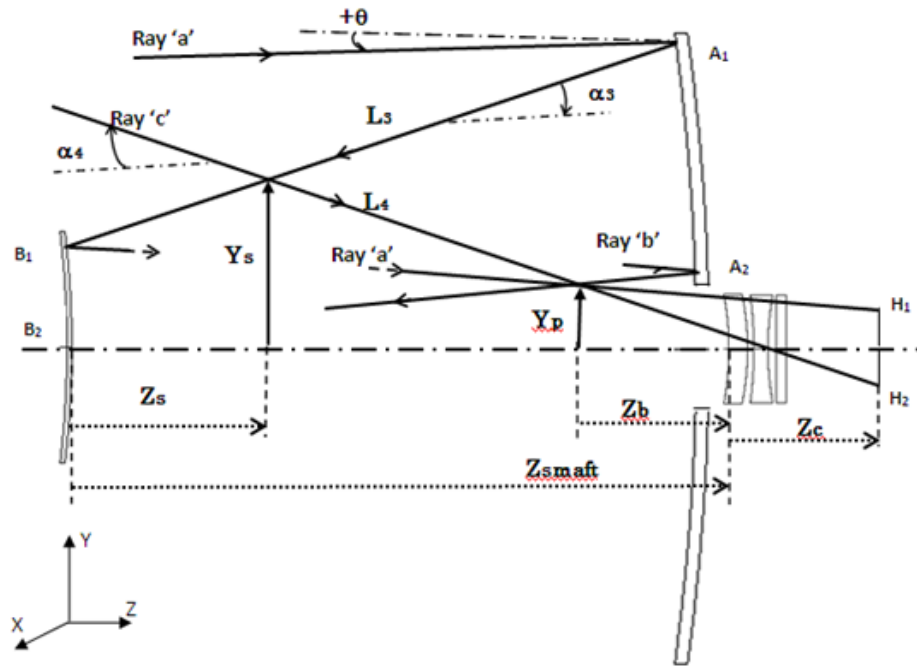


Fig. 2.3 Optical layout pertinent to the secondary mirror baffle parameters

The aim is to find Z_s (defines the location of the front end from the secondary mirror vertex plane) and Y_s (defines the semi-diameter of the front end cut-out) of the secondary mirror baffle. The imaging ray a originates from the positive edge of FOV of object and passes at the rim of entrance pupil of the telescope. It intersects at A_1 on the primary mirror and after reflection it strikes at

B_1 on the secondary mirror (shown in Fig. 2.3). The reflected ray from the secondary mirror strikes at H_1 on the image plane after passing through the aft-optics. Ray c is a typical direct ray of stray light enters the telescope and passes at the edge of the primary mirror baffle cut-out Y_p located at Z_b distance from the aft-optics front end (computed in the step:1). It strikes at H_2 on the image plane after passing through the aft-optics (shown in Fig. 2.3).

The necessary conditions for secondary mirror baffle are, (condition: 3) baffle should not block the ray segment L_3 of ray a between primary mirror and secondary mirror and (condition: 4) baffle should block the ray segment L_4 of the ray c that enters telescope and travels through the edge of primary mirror baffle towards the aft-optics (shown in Fig. 2.3). As mentioned earlier the ray segments are expressed in the form straight line equation. Therefore, L_3 is written as,

$$Y = m_3 \times Z + c_3 \quad (2.3a)$$

m_3 is the slope ($\tan(\alpha_3)$) of ray segment “ L_3 ” and c_3 is the intercept height from optic axis of the ray segment at the vertex plane of secondary mirror.

L_4 is written as,

$$Y = -m_4 \times Z + c_4 \quad (3b)$$

m_4 is the slope [$\tan(\alpha_4)$] of ray segment L_4 and c_4 is the intercept height from optic axis of the ray segment at the vertex plane of secondary mirror.

The conditions 3 and 4 are satisfied simultaneously at the intersection point of L_3 and L_4 . At the intersection point Eqs. (2.3a) = (2.3b) and also Z is denoted as Z_s . Hence,

$$Z_s = \frac{c_4 - c_3}{m_3 + m_4} \quad (2.4a)$$

When $Z=Z_s$ in eqn. 2.3b then $Y=Y_s$, thus

$$Y_s = -m_4 \times Z_s + c_4 \quad (2.4b)$$

The coefficients defined in Eq. 2.3a are computed with the optical design program in the following way. The coefficients m_3 and c_3 are computed by placing one dummy surface at zero distance from the secondary mirror before reflection in the sequential optical design data of the telescope. The unsigned output value of tangent angle and ray intercept for Y -axis for the ray a at that dummy surface computed through ray trace tool of optical design software are substituted for m_3 and c_3 respectively.

The coefficients of Eq. (2.3b) are computed in two steps. Step (i). The angle α_4 of ray segment L_4 of the ray c is computed through optical design scheme shown in Fig. 2.4. The aperture stop of semi-diameter Y_p is placed at Z_b . A ray of input angle α_4 is traced through the edge of the aperture stop (pupil) such that it intersects at H_2 on the image plane after refracting through the aft-optics, hence $m_4 = \tan (\alpha_4)$. Step (ii). The c_4 is calculated through the Eq. (2.5), by substituting the value of Y_p and Z_p from the step 1, and m_4 from step (i).

$$c_4 = Y_p + m_4 \times Z_p \quad (2.5)$$

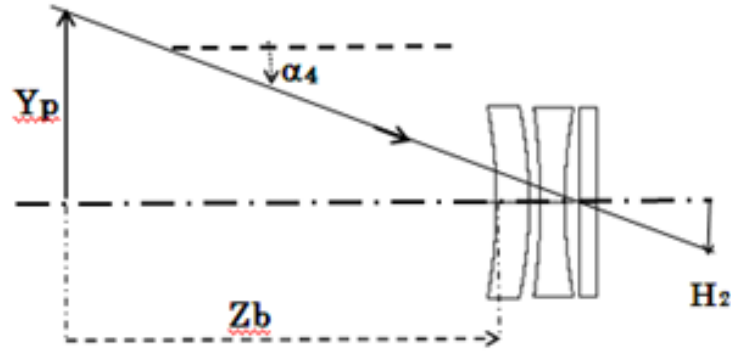


Fig. 2.4 Optical layout for determination of ray “c” parameters

One can see at the end of design steps: 1 and 2, the parameters of primary mirror baffle blocks direct rays of stray light of angle $\geq \alpha_4$ and the parameters of secondary mirror baffle blocks direct rays stray light of angle $\leq \alpha_4$. Also both the baffles parameters do not vignette the imaging rays.

2.2.2 Iterative Method (IM)

It is desirable to have baffles blocking the stray light over the required FOV with the minimum obstruction of the imaging light. This imposes the additional criterion of minimum obscuration to the imaging light on the baffle design. The minimum obscuration occurs when both baffles cause equal obscuration; in other words, $Y_e = Y_s$ (Hales, 1992). One can observe from the direct method of baffle design that for the initial value of axial obscuration $Ye_1 = r_s$ (step 1) leads to Ys_1 (step 2) and for the new value of $Ye_2 = Ys_1$ in the second iteration leads to Ys_2 which is $\neq Ye_2$, thus not satisfying the additional criterion. Because of this, the solution space that satisfies $Ye = Ys$ is not linear (Song et al, 2002). Therefore we propose to find the solution iteratively with the likely value that satisfies the baffle criteria. One can find the likely value by constructing

linear expression $Y_s = \alpha.Y_e + \beta$ with α (slope) and β (intercept with Y_s -axis) calculated from the above two results and solve it for Y_e at $Y_e = Y_s$. Therefore, from third iteration onwards the new value of Y_{e_n} is obtained from Eq. (2.6).

$$Y_{e_n} = \frac{\beta}{1 - \alpha} \quad (2.6)$$

$$\alpha = \frac{Y_{s_{n-1}} - Y_{e_{n-1}}}{Y_{e_{n-1}} - Y_{e_{n-2}}} \quad (2.7)$$

$$\beta = \frac{[Y_{e_{n-1}}^2 - Y_{e_{n-2}} \times Y_{s_{n-1}}]}{Y_{e_{n-1}} - Y_{e_{n-2}}} \quad (2.8)$$

where $n \geq 3$.

Eqs. (2.1- 2.6) are iterated till the convergence criterion $|(Y_{e_n} - Y_{s_n})| < \Delta$ is satisfied (with $Z_{a_n} = Z_d$ for $n = 1$ and $Z_{a_n} = Z_d - Z_{s_{n-1}}$ for $n \geq 2$). Where Y_{e_n} is the input obscuration of n th iteration, Y_{s_n} is the calculated semi- diameter of secondary mirror baffle Y_s of n th iteration, and Δ is acceptable difference (say, $< 10^{-2}$ mm). In reality, during iterations only the coefficients of L_1 , L_4 and value of Y_e are recomputed.

The slope m_4 can alternatively be found with the following method to reduce the design time. The m_4 can be calculated initially by neglecting the aft-optics in the ray path through Eq. (2.9a). The aft-optics nominally is a low negative powered system. For a given input ray angle the aft-optics deviates the ray to longer image height. When the iteration starts converging, find r , where r is the fraction of difference in ray angle without and with aft-optics required to

reach the image semi-height h to ray angle with aft-optics required to reach the image semi-height h (Fig. 2.4) at that iteration. For subsequent iterations, the m_4 is calculated through Eq. (2.9b),

$$m_4 = \left\{ \frac{Yp_n + h}{\left[Z_{smaft} - Zp_n + Z_c \right]} \right\} \quad (2.9a)$$

$$m_4 = \left\{ \frac{Yp_n + h}{\left[Z_{smaft} - Zp_n + Z_c \right]} \right\} \times 1 - r \quad (2.9b)$$

where Yp_n and Zp_n are n th iteration values of Yp and Zp respectively, and Z_c is the distance between the front of aft-optics and the image plane (shown in Fig. 2.3).

One can see that the baffle parameters determined with this method satisfy additional criterion of minimum obscuration along with the basic criterion of baffle mentioned in section 2.2.

2.3 Baffle design for a rectangular image format

It is obvious, in the case of a rectangular image format telescope, the image height along the length h_y (Y -axis, hence FOV θ_y) and the image height along the width h_x (X -axis, hence FOV θ_x) are different. Therefore, one expects different length and diameter for both the baffles along X and Y axes. Though the FOV is different along X and Y axes, for symmetry, the physical aperture of optical components are mostly kept circular commensurate with the larger FOV

(θ_y) rays. For easy implementation, we propose an approach for determination of baffle parameters, detailed in the following steps, that does not violate the basic baffle design criterion.

Step A: Determine parameters of the primary mirror baffle Z_p and Y_p and the secondary mirror baffle Z_{s_x} and Y_s along Y -axis with the iterative method (Sec 2.2.2), where Y_p and Y_s are semi-diameter of front end of primary mirror and secondary mirror baffles along Y axis at distance Z_p and Z_{s_x} from secondary mirror vertex plane respectively.

Step B: Determine semi-diameter X_p of the front end of primary mirror baffle along the X -axis, through Eq. (2.2b) by substituting the value of Z_p calculated in step A and the value of coefficients of ray segment L_1 computed from the ray redefined for FOV θ_x (as in Sec 2.2.1, step 1).

Step C: Determine of X_s semi-diameter of front cut-out of secondary mirror baffle along X -axis located at distance Z_{s_y} from secondary mirror vertex plane through Eqs. (2.4a) and (2.4b) by substituting the values of coefficients of ray segment L_3 computed from the ray redefined for the FOV θ_x and ray segment L_4 computed from the ray redefined for the FOV θ_x (as in Sec 2.2.1, step 2) and values of X_p and Z_p computed in the previous steps A and B.

This approach is still found to achieve obscuration along X direction close to the minimum (shown with a numerical example in Chapter 3). The resultant shape of the primary and secondary mirror baffles is rectangle and oversized to the requirement of blocking of direct rays of stray light. Smaller

effective obscuration can be achieved by redefining the corners of cut-out of the baffles.

The corner coordinates (Xp_c , Yp_c) of the primary mirror baffle are determined with a skew ray. The skew ray originates from the edge of FOV of object along X i.e. θ_x and Y axes i.e. θ_y passes through the pupil at polar coordinate $(R, 45^\circ)$ shown in Fig. 2.5. The skew ray after reflection at primary and secondary mirrors intersects on the front end of the primary mirror baffle located at distance Zp from the secondary mirror vertex plane at height Xp_c and Yp_c along X and Y axes respectively.

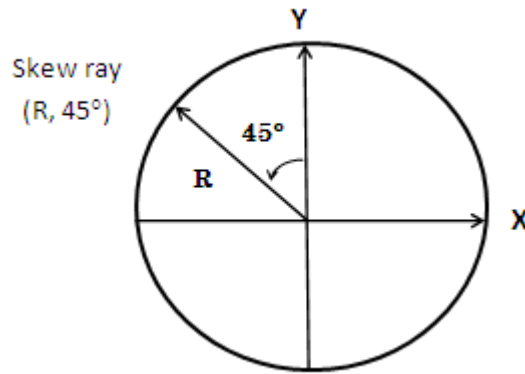


Fig. 2.5 Definition of skew ray at pupil

The ray intercept (Xp_c , Yp_c) on the front end of the primary mirror can be computed with the optical design software in the following way. A dummy surface placed at distance Zp from the secondary mirror vertex after reflection in the sequential optical design data of telescope. The value of intercept for X and Y axes at that dummy surface for the skew ray gives Xp_c and Yp_c . The final shape of the cut-out of front end of primary mirror baffle with pertinent details is shown in Fig. 2.6 and parameters defining it are calculated through Eq. (2.10).

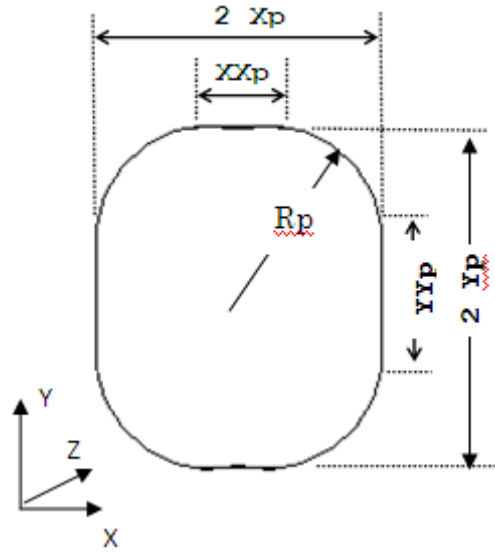


Fig. 2.6. Front view of primary mirror baffle

$$\left. \begin{aligned}
 R_p &= \sqrt{Y_{pc}^2 + X_{pc}^2} \\
 \text{If } R_p > Y_p &\text{ then} \\
 YY_p &= 2 \times \sqrt{R_p^2 - X_p^2} \\
 XX_p &= 2 \times \sqrt{R_p^2 - Y_p^2} \\
 \text{If } R_p < Y_p &\text{ then} \\
 R_p &= Y_p \\
 XX_p &= 0 \\
 YY_p &= 2 \times \sqrt{R_p^2 - X_p^2}
 \end{aligned} \right\} \quad (2.10)$$

The secondary mirror baffle corner coordinates (X_{s_c} , Y_{s_c}) are calculated at distance Z_{s_x} from the secondary mirror vertex through following two steps,

Step 1: Find the slope of L_4 through Eq. (2.9b) replacing Y_p with Xp_c and h with h_x . Again find the slope of L_4 through Eq. (2.9b) replacing Y' with Yp_c and h with h_y .

Step 2: Find the intercept Xs_c of L_4 on X-axis of the secondary mirror vertex plane through Eq. (2.5) replacing Y_p with Xp_c , Zp with $Zp-Zs_x$ and m_4 from step 1. Again find the intercept Ys_c of L_4 on Y-axis of the secondary mirror vertex plane through Eq. (2.5) replacing Y_p with Yp_c , Zp with $Zp-Zs_x$ and m_4 from step I.

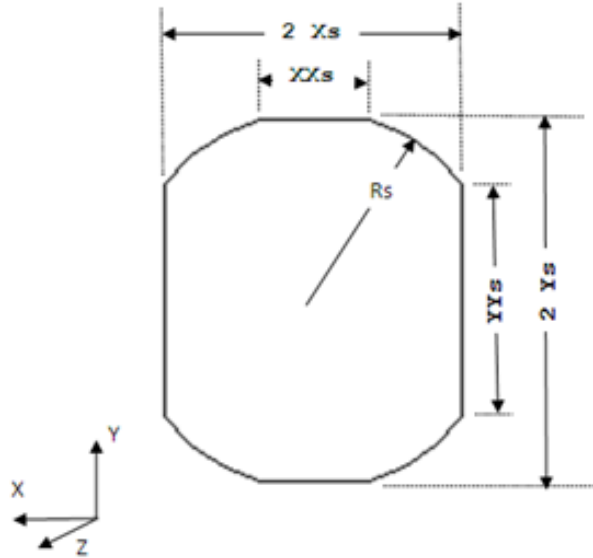


Fig. 2.7. Front view of the secondary mirror baffle

The typical projected shape of the front side of secondary mirror baffle with pertinent parameters is shown in Fig. 2.7 and the parameters of secondary mirror baffle are calculated through Eq. (2.11). Typical side and isometric views of secondary mirror baffle are shown in Figs. 2.8 and 2.9 respectively.

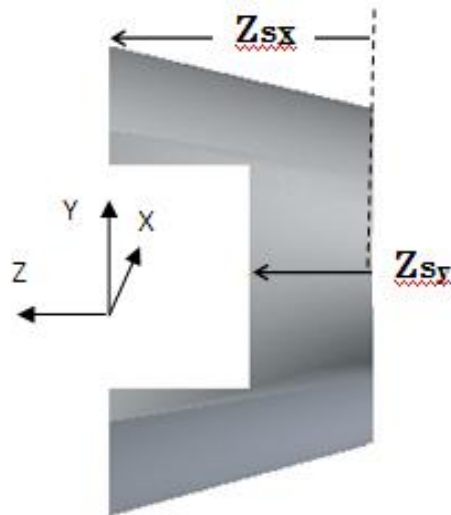


Fig. 2.8. Side view of the secondary mirror baffle



Fig. 2.9. Isometric view of the secondary mirror baffle

$$\begin{aligned}
&Rs = \sqrt{YSc^2 + XSc^2} \\
&\text{If } Rs > Ys \text{ then} \\
&YYs = 2 \times \sqrt{Rs^2 - Xs^2} \\
&XXs = 2 \times \sqrt{Rs^2 - Ys^2} \\
&\text{If } Rs < Ys, \text{ then} \\
&Rs = Ys \\
&XXs = 0 \\
&YYs = 2 \times \sqrt{Rs^2 - Xs^2}
\end{aligned}
\tag{2.11}$$

2.4 Design of Vanes for the primary mirror baffle

The baffle for a typical RC telescope though it is calculated from the vertex of primary mirror, extended beyond the rear surface of the primary mirror for ease of mounting. In the case of modified RC telescope it is preferable to extend the length of the baffle nearer to the aft-lens assembly to avoid reflections from primary mirror central core and other mechanical elements. The primary mirror baffle can be i. tubular or ii. converging conical or iii. diverging conical structure. To reduce the stray light contribution from the inner walls of the primary mirror baffle, annular light stops called vanes are required. Tubular structure is preferred for ease of fabrication, assembly with main telescope structure and placement of vanes in it. Vanes are placed such that ray entering the

front port of primary mirror baffle will not reach the image plane after single reflection from inner walls of the baffle as shown in Fig 2.10.

The objective of the vane design is to block the light rays illuminating the inner wall of the baffle from reaching the image plane after single reflection (first order secondary rays) and do not vignette the imaging rays (FOV). The design of vanes is to find the inner and outer diameter of the annular vanes and their position along the length of primary mirror baffle.

In the modified RC telescope configuration, the presence of the aft-lens es deviate the ray further away from the optic axis than its absence. Without loss of generality, the spacing between the front element of the aft-lens and the image plane is considered as air space with a nominally reduced deviation of ray. The position of the vanes is calculated for the maximum FOV. The vanes are calculated backwards starting from the primary mirror baffle end nearer to the image plane and towards the baffle other end in the sequence as shown in Fig. 2.10. The parameters of the vanes are calculated through the following steps:

1. A line drawn from the front end of the baffle to the radial opening of the vane at the back end defines the FOV line.
2. A ray segment R_1 is drawn from H_2 to PB and intercepts at the inner wall of the baffle at a distance from the rear end of the baffle dV_{Im} .
3. After reflection from the inner wall the ray segment R_{1p} intercepts the FOV line at dV_l from the rear of the baffle defining the position of the vane.
4. At this position the vane inner radius V_{Ir} is calculated.

5. A ray segment R_2 is drawn from H_2 to the inner radius of vane 1 (V_{1r}) and intercepts at the inner wall of the baffle at dV_{2m} from the vane 1.
6. Steps 3 to 5 are repeated till vanes position reaches the front end of the baffle.

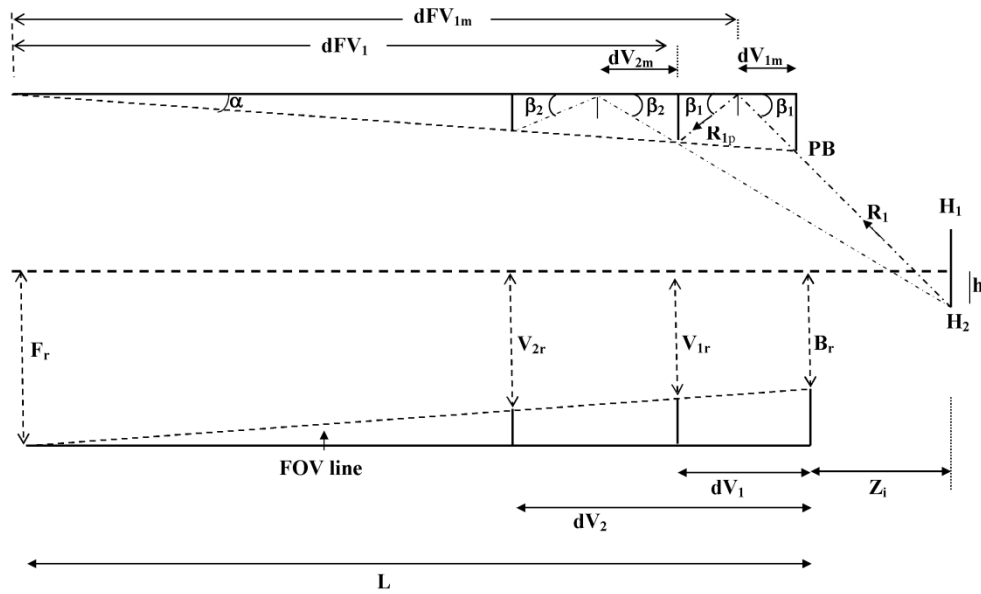


Fig. 2.10. Placement of vanes in the primary mirror baffle

The expressions governing the design of parameters of vanes are given in Eq. (2.12), where $k= 0$ to n (n is the vane near the front end of the baffle)

$$\left. \begin{aligned}
 dV_0 &= 0 \\
 V_{0r} &= Br \\
 \beta_k &= \frac{(h + V_{k-1})}{(Z_i + dV_{k-1})} \\
 dV_{km} &= \frac{(F_r - V_{k-1}r)}{\beta_k} \\
 dFV_{km} &= L - dV_{km} \\
 tV_{km} &= \frac{(\alpha dFV_{km})}{(\alpha + \beta_k)} \\
 dFV_k &= dFV_{km} - tV_{km} \\
 V_{kr} &= F_r - \alpha dFV_k \\
 dV_k &= L - dFV_k
 \end{aligned} \right\} \quad (2.12)$$

2.5 Summary

We have developed a new method of baffle design (Direct Method), not limited to the FOV, for blocking the direct rays of stray light of a modified RC telescope. We have also developed another method of baffle design (Iterative Method) that in addition to blocking of direct rays of stray light results in the minimum baffle obscuration. These methods are based on combination of results of commercial optical design program and analytical relations developed

herewith. Since these methods employ actual ray coordinates, the calculated baffle parameters are accurate. The iterative method of baffle design is simple and easy to adapt and also that will bring a marked improvement in the achievable MTF as against that of the DM due to the minimum effective baffle obscuration. We have also described a method of baffle design for a rectangular image format modified RC telescope. Adopting the iterative method one can design baffles along with the optical design of telescope. Also this method can be applied to other axial two-mirror-based telescope and derivatives. We have then described a method of design of glare stop (vane) for the primary mirror baffle to stop the first order reflection from the inner wall.

Portion of the work is published in

“Iterative method of baffle design for modified Ritchey–Chretien telescope,” *Appl. Opt.*, (2013), **52**(6): 1240-1247.

CHAPTER 3

DESIGN, MODELLING AND EVALUATION OF STRAY LIGHT SHIELD FOR A MODIFIED RC TELESCOPE

3.1 Introduction

In the previous chapter, we have developed a baffle design method for a rectangular image format modified RC telescope. It has been described that the parameters of baffles computed are able to restrict the direct rays of stray light and also first order reflected rays from the inner wall of the primary mirror baffle. Here, we have quantified the performance of the baffle with a realistic numerical example. For this purpose the telescope and baffles are modeled in the ZEMAX[®] optical design program (ZEMAX[®], 2009). The stray light analysis is carried out using the non-sequential mode and the imaging performance analysis i.e., the MTF is computed using the sequential mode of ZEMAX[®].

3.2 Numerical example

We have applied the baffle design methods to a F/8, 5.6m, $r_s=101$ mm, modified RC telescope with 1 m separation between mirrors and 1.3 m total length operating at visible spectrum having a 40 x 120 mm ($0.2^\circ \times 0.6^\circ$) rectangular image format (shown in Fig. 3.1).

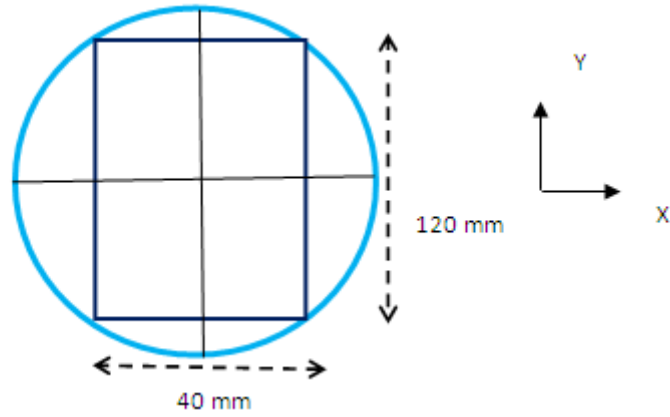


Fig. 3.1. Definition of a rectangular image format

3.3 Design of baffles

The computations required for the baffle design are carried out with the optical design program ZEMAX[®]. The optical layout of the telescope is defined in the sequential mode of the ZEMAX[®] and the required rays' coordinates are obtained through the ray trace routine of ZEMAX[®]. The baffle parameters are computed using the DM and the IM methods. In the case of IM, the baffle parameters are converged in ten iterations to $|Y_e - Y_s| < 10^{-3}$ mm. The convergence of the iterations is shown in Fig. 3.2.

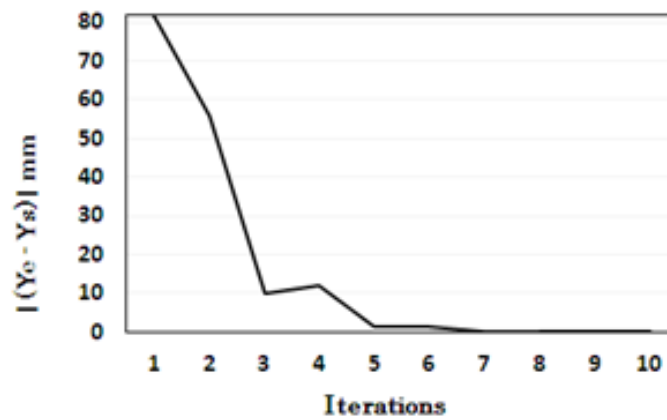


Fig. 3.2. Convergence of iteration for the baffle parameters

Tables 3.1 and 3.2 show comparison of the parameters of baffles obtained with the IM and the DM. The cut-out dimension X_s of the secondary mirror baffle is computed using the approach discussed in Chapter 2; Sec 3. and the iterative method. The difference in cut-out dimension X_s of the secondary mirror baffle calculated between the approach proposed in Chapter 2 and the IM is found to be $\sim 0.9\%$ (1 in 105 mm). Therefore, the approach suggested for rectangular FOV telescope still closely satisfies the criterion of baffle design. By virtue of analytical solutions involved in the design of baffles, satisfying the necessary criterion of baffles design, the parameters of the baffles ensure blocking of the direct rays of light. The vanes of the primary mirror baffle are computed and parameters are given in table 3.3. We have described modelling of the baffle and the performance evaluation of it in the following sections.

Table 3.1: Comparison of parameters of the primary mirror baffles

Parameters	Primary mirror baffle by the IM (mm)	Primary mirror baffle by the DM (mm)
$2Y_p$	165.096	148.464
$2X_p$	128.476	88.162
R_p	82.516	74.732 ($R_p < Y_p$)
YY_p	103.685	120.693
XX_p	0	0
$Z_d - Z_p$	516.145	201.738

Table 3.2: Comparison of parameters of the secondary mirror baffle

Parameters	Secondary mirror baffle by the IM (mm)	Secondary mirror baffle by the DM (mm)
$2Y_s$	286.292	363.334
$2X_s$	222.275	270.702
R_s	156.582	180.118
$R_s < Y_s$	$R_s = 156.582$	$R_s = 182.883$
YY_s	220.604	272.165
XX_s	126.921	0
Z_{s_y}	66.182	106.629
Z_{s_x}	162.793	309.207

Table 3.3: Dimensional details of the primary mirror baffle with vanes

S.No	2.Yp (mm)	2.Xp (mm)	Rp (mm)	XXp (mm)	YYp (mm)	Distance from the previous vane (mm)
Front end	165.096	128.476	82.516	0.0	103.685	0
1	164.691	127.782	82.325	0.0	103.832	6.55
2	164.066	126.710	82.029	0.0	104.209	10.13
3	163.177	125.186	81.610	3.721	104.733	14.38
4	161.931	123.049	81.024	6.154	105.444	20.17
5	160.215	120.107	80.221	8.528	106.376	27.78
6	157.909	116.152	79.148	11.079	107.548	37.32
7	154.910	111.012	77.767	13.903	108.935	48.52
8	151.176	104.609	76.066	17.025	110.458	60.44
9	146.764	97.044	74.088	20.405	111.976	71.41
10	141.866	88.645	71.935	23.929	113.316	79.27
11	136.790	79.941	69.756	27.422	114.336	82.16
12	131.890	71.541	67.707	30.693	114.974	79.29
Back end	127.476	63.972	65.911	33.572	115.260	71.44

3.4 Modelling of baffles

The quantification of the performance of the baffles and vanes for the direct rays of stray light and first order reflection from the inner walls of the primary mirror baffle are carried out using the non-sequential mode of the ZEMAX[®]. The baffle parameters are modelled using the NSC and user defined objects of ZEMAX[®]. The three dimensional shapes of the baffles are constructed with the combination of several NSCs in the ZEMAX[®]. These NSC include standard surfaces, annular volume, annuls, Toroidal surfaces, cylindrical, rectangular volumes etc. Some complicated shapes such as the primary mirror baffle vanes and back of secondary mirror baffles are constructed using the UDA files; these files consist of two dimensional shapes. The entire three dimensional baffle elements of telescope are made of NSC objects as shown Fig. 3.3. In the model, the larger FOV direction is kept along X axis and optic axis is along Z.

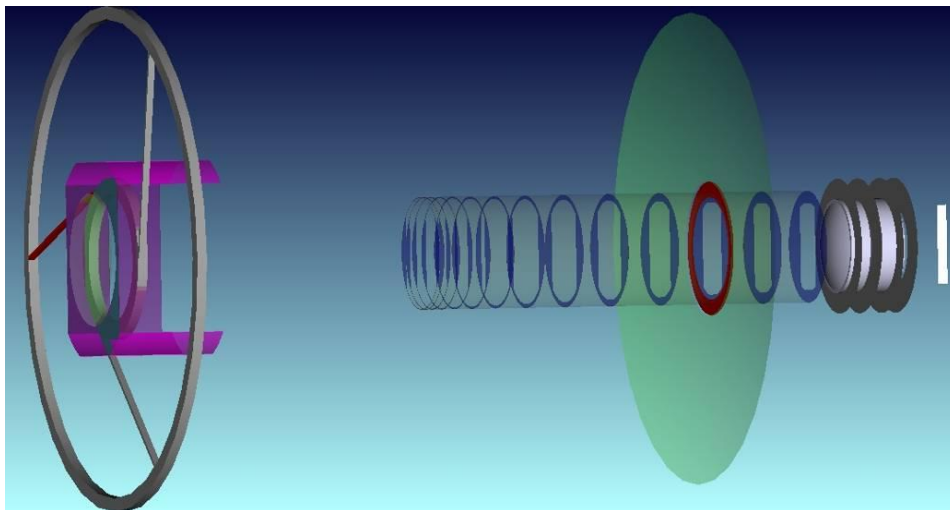


Fig. 3.3 Baffles modelled using Zemax NSC

The primary mirror baffle with vanes is shown in Fig. 3.4 and the secondary mirror baffle is shown in Fig. 3.5.

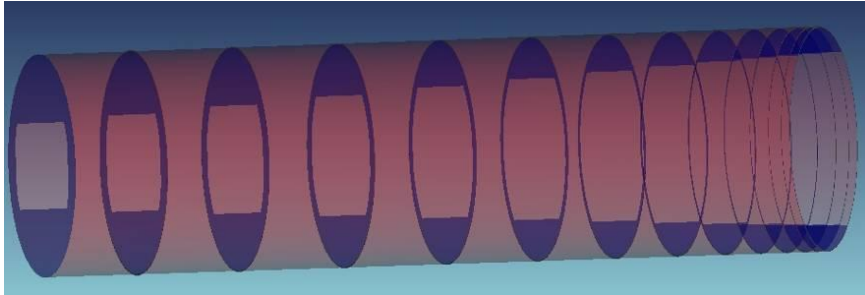


Fig. 3.4 Model of the primary mirror baffle with vanes

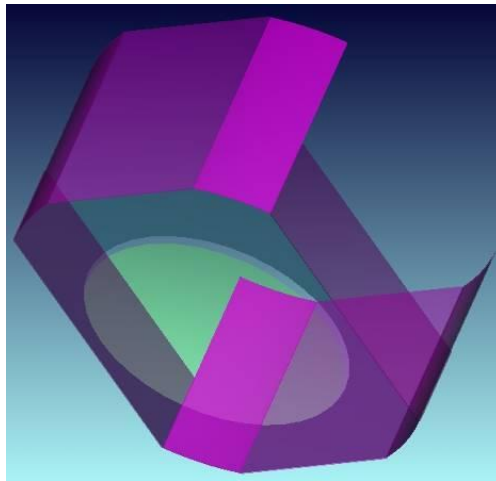


Fig. 3.5 Model of the secondary mirror baffle

All the NSC object positions are defined with respect to the primary mirror vertex coordinate. The primary mirror baffle is constructed using the NSC objects and the UDA. The cylindrical tube of the baffle is constructed using the NSC object cone having the same diameter at both ends. Two concentric cylindrical tube having a radius difference equivalent to the thickness of the primary mirror baffle cylinder is modelled. The gap between the two concentric

cylinders is blocked by the absorbing NSC annulus object having annulus inner and outer radii equivalent to the baffle cylinder object. The vanes of the baffle are created with the UDA. The secondary mirror baffle is constructed in three parts. The rear part of the secondary baffle is constructed with the UDA, curved projected corners are constructed with rectangular torus surface NSC object and sides are constructed with rectangular volume NSC object. The construction parameters of baffles and vanes are given in appendix-1.

3.5 Modelling of source and detector

The light source is constructed with the NSC source ellipse. This source has the property of giving a collimated output light over the defined aperture. The rays emitted from this source are uniformly distributed within the aperture grid. In each of the non-sequential ray tracing trail a new set of random and uniformly distributed rays are generated over the aperture grid. The radius of this source ellipse is kept with an adequate margin to cover the entire aperture and also the required FOV. One million rays originating from the source ellipsis is used for the analysis. The light source is placed behind the secondary mirror. To detect the light ray reaching the image plane, an NSC detector rectangle is placed at the focal plane with a size equivalent to the rectangular image format. The detector rectangle absorbs the rays impinge on it and gives the number of rays or power fall on it.

3.6 Stray light analysis

In the non-sequential ray tracing, a ray reflects from a mirror or transmits from a lens the total energy is retained by the ray; no losses are incorporated as

the parent ray does not split into several child rays. All the mechanical elements such as baffles and vanes are made as perfect absorbers. When a ray hits these mechanical elements the ray gets absorbed or gets terminated. Any ray reaching the rectangular detector has to be either a direct ray or it has to traverse the active imaging light path of the telescope via primary, secondary mirrors and relay lenses. If we make both the mirrors as absorbing materials, then only the direct path rays will reach to the detector plane. In order to generate various field of view angles of light rays, source is tilted with respect to the optic axis of the telescope. The light rays with field angles ranging from 0° to 20° with a small step size of 0.1° are traced in X , Y and XY directions of the telescope; as Z being the optical axis. The rays traced through the telescope for the FOV of 0.5° and 11° are shown in Figs. 3.6 and 3.7 respectively. In the Fig. 3.7, it is clear that the non-FOV rays do not reach the detector plane and only the FOV rays reach the detector plane.

Fig. 3.6 Non-sequential ray trace for the FOV 0.5°



Fig. 3.7 Non-sequential ray trace for the FOV 11°

The number rays reaching the detector are normalized to the on- axis FOV. The normalized ray hits for various FOV angles scanned in X , Y and XY directions are given in tables 3.4 to 3.6.

Table 3.4: Ray trace for the field angles in the larger FOV(cross track) direction.

field value	Normalised ray hits on the detectors
20° to 0.7° with steps of 0.1°	No ray hits
0.6°	0.969
0.5°	0.984
0.4°	0.994
0.3°	0.999
0.2°	0.998
0.1°	0.999
0°	1.000

Table 3.5: Ray trace for the field angles in the smaller FOV (along) direction.

Y- field value	Normalised power received on the detectors
20° to 0.3° with steps of 0.1°	No hits or zero power
0.2°	0.9995
0.1°	0.9998
0°	1.0000

Table 3.6 Ray trace for the field angles in the diagonal FOV direction.

X- field value	Y- field value	Normalised power received on the detectors
20° to 0.3° with step size of 0.1°		No hits or zero power
0.2°	0.2°	1.000
0.1°	0.1°	1.000
0°	0°	1.000

For the evaluation of reflections from the inner walls of the primary mirror baffle, the inner cylindrical baffle NSC object is set to 7% reflectivity. The light transmission characteristics of all other elements of the telescopes are kept same as in the direct ray of stray light analysis. The *ray split tracing* is carried out. In this ray trace, the input unit power (1 watt) is divided equally among all rays and every time a ray hits the surface of the baffle, secondary rays are produced with modified energies depending on the reflection properties of the surface. The ray trace is performed over the entire span of FOV (0° to 20°). A ray is terminated from the trace once its relative power after reflections reduces to 1/1000th of it from the light source input. The threshold output power at the detector rectangle is kept at 1/10,000th of the power of the on-axis FOV at the detector; which

corresponds to 1 order of magnitude less than the 1 level of 10-bit digitization. The normalized ray power reaching the detector plane with and without vanes is shown in Fig. 3.8. The normalization is carried out with respect to the on- axis FOV. The flat line along the field axis in Fig. 3.8 shows that no reflected ray power reaches the detector. Though, in the earlier analysis, at least 3 internal reflections are possible before a ray is terminated to emphasis the efficiency of the vanes further for the multiple internal reflections, the analysis is carried out for 40% reflectivity and no significant power received at the output of the detector rectangle.

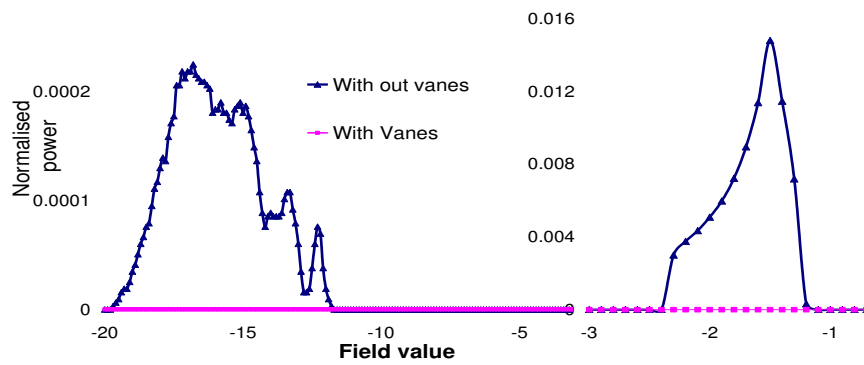


Fig. 3.8 Plot of normalized light power reaching the detector plane with and without the primary baffle vanes

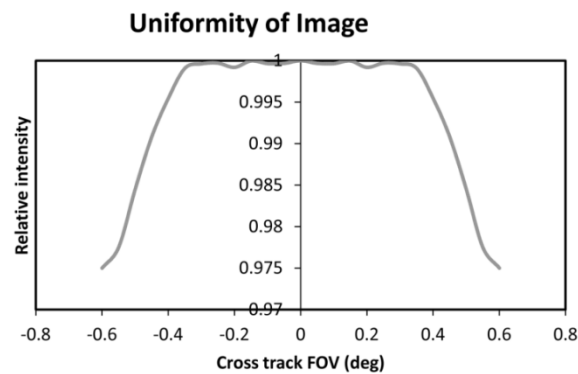


Fig. 3.9 Plot of non-uniformity of light across the image plane for ($\pm 0.6^\circ$ cross-track, 0.18° along track) coordinate

We have also evaluated the non-uniformity in the intensity across the length at one extreme width of the detector plane ($\pm 60, 19$ mm) and presented in Fig. 3.9. The ripples on flat top of the uniformity curve are due to statistical variation of number of rays traced in each ray trace execution.

3.7 Imaging performance analysis

Imaging performance of the optical system at various spatial resolutions (frequencies) is quantified by the modulation transfer function. The MTF of the axially obscured telescope is less than that of the unobscured telescope and further reduction occurs due to the increase in the baffle obscuration. The obscuration due to the baffle parameters (tables 1 and 2) of various methods viz., IM and DM are simulated in the sequential mode of Zemax using appropriately placed used defined apertures and the entrance port view of the telescope is shown in Fig. 3.10.

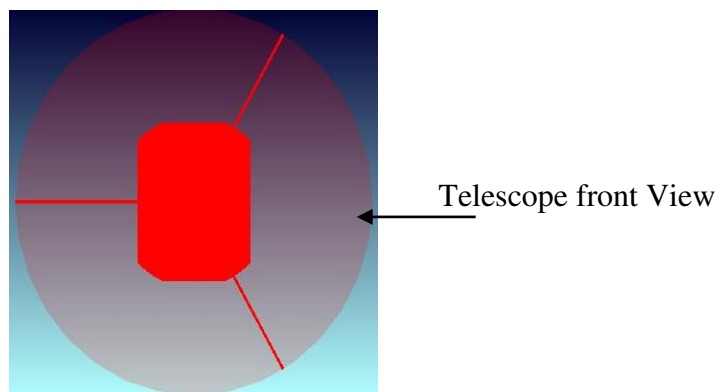


Fig. 3.10 Modelling of the effective obscuration telescope with baffles

The on-axis polychromatic MTF (tangential and sagittal) is plotted against the normalized spatial frequencies for the cases 1) nominal telescope, 2) DM and 3) IM; is shown in figs. 3.11 and 3.12 respectively. It can be noticed that

there is remarkable improvement in the MTF between low and mid spatial frequencies in the case of iterative method of baffle design in comparison to the direct method, due to minimum effective obscuration.

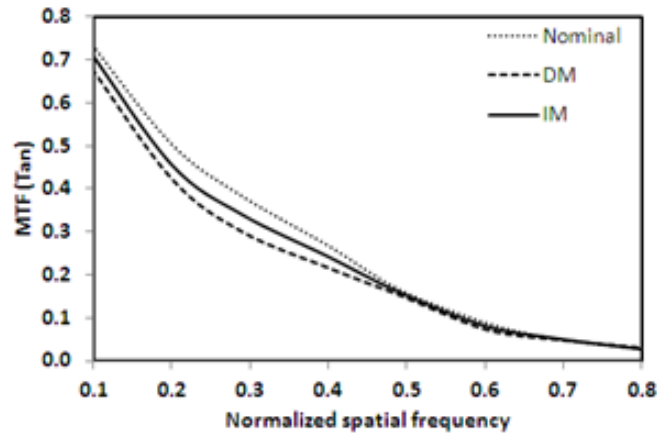


Fig. 3.11 Plot of comparison of the MTF (Tangential) for various cases

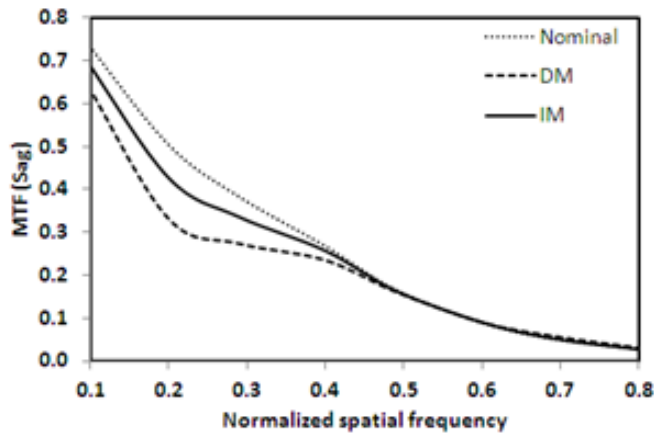


Fig. 3.12 Plot of comparison of MTF (Sagittal) for various cases

3.8 Summary

We have applied the proposed baffle design techniques on a modified F/8, F=5.6 m RC telescope. In order to evaluate the performance of the designed baffle, baffles are modelled using ZEMAX[®] optical design program. The baffles are modelled using the NSC and the UDA files of the ZEMAX[®]. The stray light

analysis carried out using the NS mode. It is found that except the FOV rays, no non-FOV rays are directly reaching the detector plane. Also the efficiency of the vanes of the primary mirror baffle is evaluated. It is also observed that the vanes efficiently stop the internal light reflections from the inner wall of the cylindrical primary mirror baffle reaching the detector plane. The imaging performance of the telescope is evaluated in the sequential mode having the obscuration of baffles modelled with the UDA. The results show that there is remarkable improvement on the MTF between low and mid spatial frequencies with the iterative method in comparison to the direct method of baffle design; due to minimum effective obscuration. To conclude that we have investigated the limitations of the earlier methods of baffle design and developed new methods to overcome it.

CHAPTER 4

DIRECT BONDED MOUNTING OF OPTICAL COMPONENT: AN EXPERIMENTAL STUDY

4.1 Introduction

The mechanical stress on the optical component during its assembly distorts the optical surface, which in turn degrades the image formed by the optical system. Figs. 4.1 and 4.2 show the interferogram, spot size and the MTF at 70 lp/mm for a free and a stressed mirror condition respectively. Unlike plane optical surface elements, powered optical elements like mirrors, lenses etc are required to be positioned with tight tolerance without distorting the optical surface. In space- borne high resolution systems, the requirement on the surface figure tolerance and the positional tolerances are more stringent. It means the optical components shall be held rigid (not to allow any positional changes) and shall also be flexible (not to allow any surface distortion). This may be partly a necessity and partly to overcome other uncertainties in the overall system built-up. This type of requirement is accomplished by semi-kinematic mounts called flexure (Yoder 2006a; Yoder 2006b; Fitzsimmons et al., 2008; Kihm et al. 2010). Any mechanical disturbance results in a rigid body motion not in a surface distortion. The flexure is directly bonded to the mirror with an adhesive. The out-gassing of adhesive materials near the optical surface occurs in vacuum (in space) gets deposited on the reflective coated mirror surface. The deposited material on the mirror surface reduces the light transmission characteristics of the optical

system. Therefore, the adhesive for space optics is generally identified on the basis of low out-gassing and high lap shear strength.

Adhesives are selected on the basis of heritage of space programs (IRS 1C CDR, 1994) or from the declared properties (Technical data sheet Epotek-301, 1994; Technical data sheet 3M 2216 B/A gray, 2010). The changes in either surface figure or position or both of an optical element result in the performance degradation of the optical system. It was reported, the adhesive shows surface distortion upon cure (Wimperis, 1984). Surface distortion due to adhesive upon cure can be removed by post-bond figuring (Ohl et al., FUSE report; <http://fuse.pha.jhu.edu>.) or reduced by relief bond approach (Senthil et al, 2001). Surface distortions occur during the advance stages of optical system development and during its field operation cannot be corrected. Many space-qualified adhesives are available and their characteristics affecting the performance of optics are not well defined. Nevertheless, some studies on certain adhesives were reported (Daly, 2001) but more of the positional changes of optics within its mount. Theoretical study of mirror surface deformation based on the available adhesive mechanical properties and flexure design was reported by (Doyle, 2002; Pateric et al, 2011; Seo et al, 2007; Vreugd et al., 2012) using the FEM. However, there are no detailed experimental studies reported in the scientific and technical literatures, in particular, on the adhesive-induced optical surface deformation and their relation to the adhesive property. Therefore, it is necessary to understand as well as evaluate the performance of direct bonded assembly experimentally. Cases and parameters that are not reported elsewhere for adhesives Epotek-301 and 3M 2216 B/A gray are experimentally studied and discussed here. We have also attempted

from the results, to establish an empirical relation, with the known properties of adhesives of various space qualified adhesives that will help to identify adhesives for the space- borne high resolution optics.

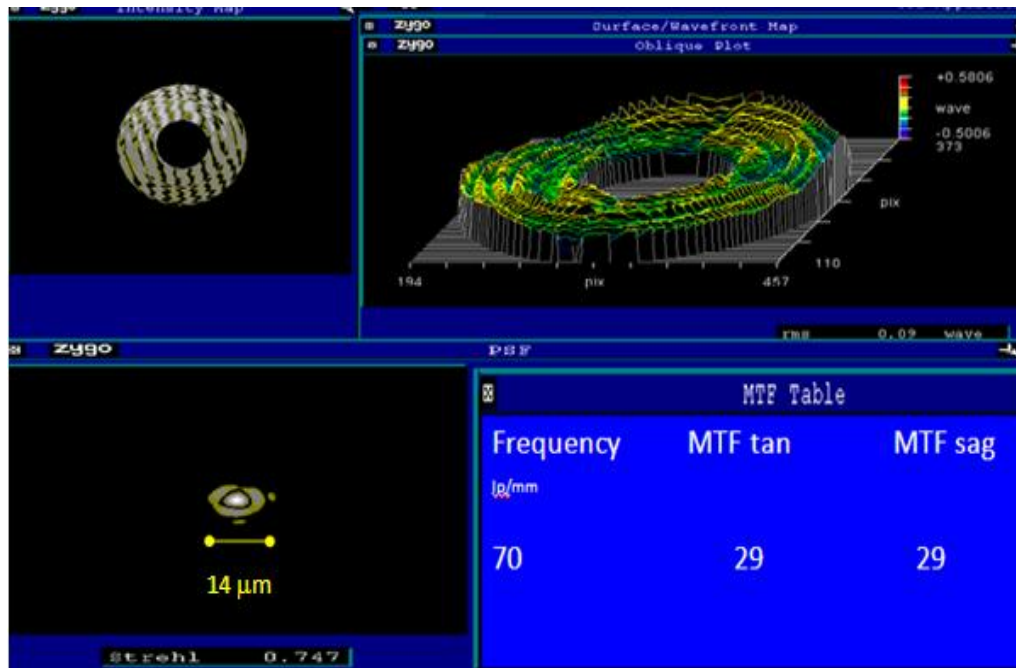


Fig. 4.1 Interferogram, surface plot, spot size and MTF of free mirror

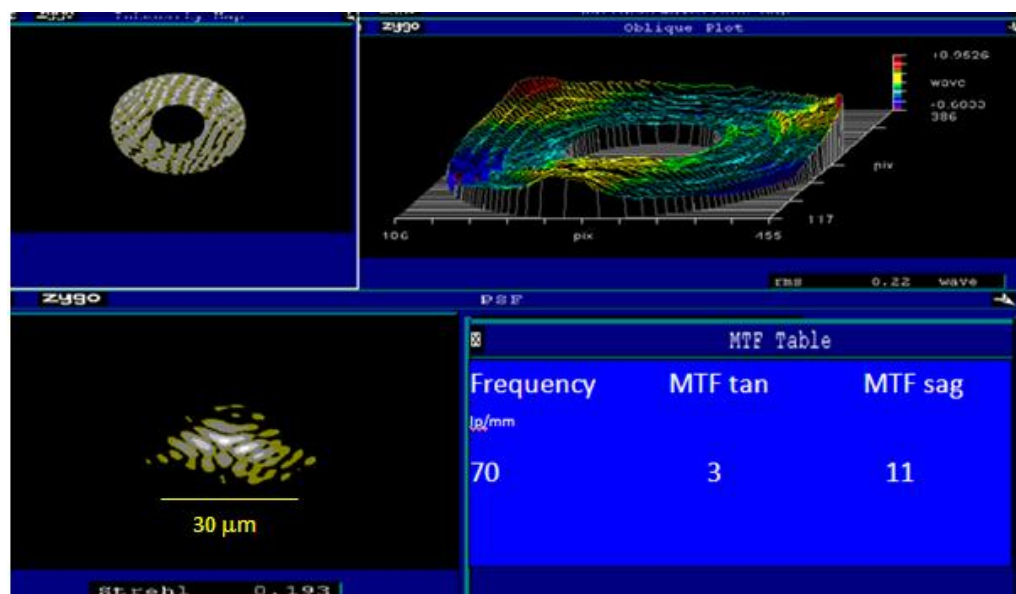


Fig. 4.2 Interferogram, surface plot, spot size and MTF of stressed mirror

4.2 Direct bonded optical mount

Mechanical mounts are used as an interface between the optical components and the instrument main structure. Various mount designs (Rogatto, 1993) namely direct adhesive bonded, semi-flexible bonded, shimmed, seat and retainer typed mounts are in usage depending upon the requirements. The direct bonded mounts are used to realize the semi-kinematic mounts. The mount is directly bonded to the mirror using adhesive. The direct bonded mount gives design flexibility in terms of isolating optical element from distortion due to thermo-mechanical effects of the instrument main structure. It also enables optical engineer to hold the component more precisely with respect to the required coordinates. In direct bonded mount, in-plane and out-of-plane linear and angular displacements are controlled to the requirement and subsequently adhesive is applied to the bond interface. The adhesive for space borne optical systems shall have properties of low out-gassing and insensitive to humidity. Out-gassing molecules can deposit on the cold optical surfaces and get baked on exposure to the sun or heat. These deposits can significantly degrade the light transmittance and the spectral characteristics of optical system. Hence the outgas molecules from the adhesive shall be within the permissible limit (NASA report; <http://www.nasa.gov/offices/oc/e/llis/0778.html>). Epoxy based adhesives, widely used for space applications are come in two parts and cure to form bond interface either at room temperature or at elevated temperature. The curing of optical assembly is preferred at room temperature which is equivalent to the operating temperature; to minimize the thermal induced stress on the optical assembly due to the difference in operating and curing temperature.

4.3 Experimental details

In this section we discuss the sample details and the evaluation method.

4.3.1 Sample Details

The samples are prepared with the adhesives Epotek 301 and 3M 2216 B/A gray and are evaluated for the parameters, viz., (i) Optical surface distortion after curing and after thermal exposure, (ii) Lap shear strength and (iii) Out-gas properties. The general properties of those adhesives are given in table 4.1 and 4.2 respectively.

For the evaluation of optical surface distortion, an optical flat diameter (ϕ) 125 mm with its front face polished to better than $\lambda/50$ rms (wavelength (λ) = 633nm) and the bonding location at its rear face center, that has Al_2O_3 -303 surface finish (to eliminate uneven adhesive contact and stress concentration), is identified. The rear face-optical mountings are preferred to the periphery mounting to minimize overall system lateral dimensions. The thickness to diameter aspect ratio of the optical flat is kept at 1:6 and 1:10 as shown in Figs. 4.3 and 4.4. Here, the 1:10 aspect ratio is defined as the thickness of $1/10^{\text{th}}$ of diameter at bond area (ϕ 52 mm) compared to other locations by scooping out the material. The mechanical mount is an invar cylindrical flexure of 153 mm long with three lugs for mounting to instrument structure; lugs are left free. Figures 4.3 to 4.5 show the schematic of the optical flats and opto-mechanical assembly. To perform the relief bond, grooves of 1 mm deep are machined on the bond pad interface of the mount as shown in fig. 4.6. The thickness to diameter aspect ratio of the optical flat is kept at 1:6 and 1:10 for Epotek-301 and 1:10 for 3M 2216

B/A gray. Additional samples for Epotek-301 are prepared for surface evaluation with relief pattern on bond area.

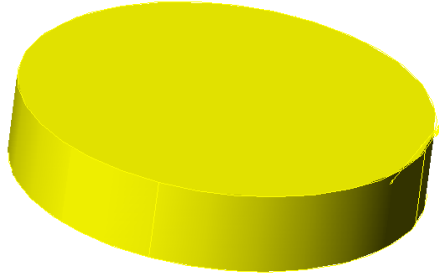


Fig. 4.3 1:6 aspect ratio optical flat

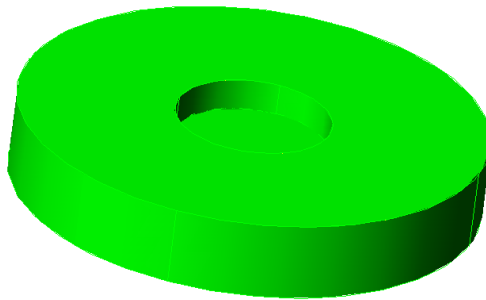


Fig. 4.4 1:10 aspect ratio optical flat

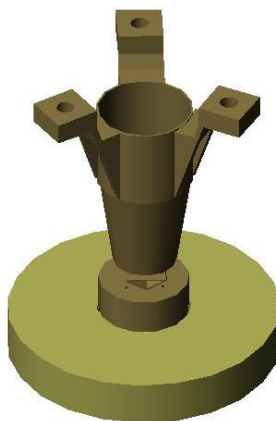


Fig. 4.5 Optical flat with the mount

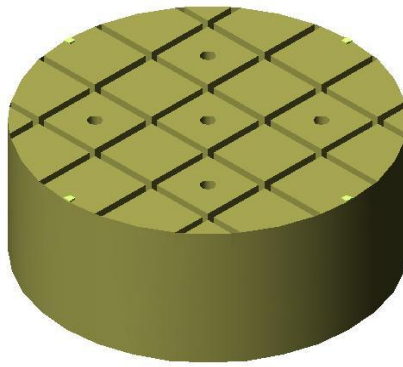


Fig. 4.6 Schematic of a relief bond pad

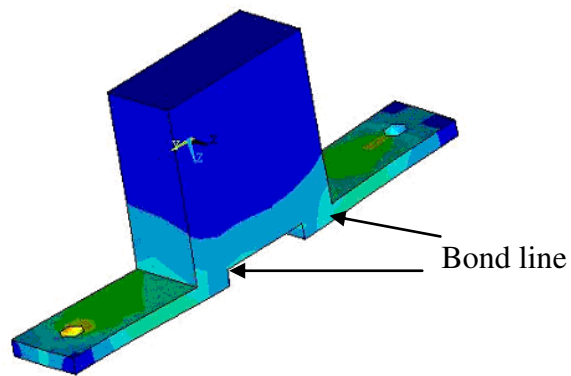


Fig. 4.7a Schematic of a lap shear sample



Fig. 4.7b Photograph of lap shear and outgas samples

The bonding portion of the flexure is $\phi=50$ mm circular pad, having surface finish similar to that of glass interface, with 150 ± 25 μm high elevated button on periphery of the bond pad to control bond line thickness. The bonded assemblies of both adhesives are cured for 10 days at $20\pm 3^\circ\text{C}$, relative humidity $50\pm 5\%$, and at ambient atmospheric pressure. For lap shear strength evaluation glass block as shown in the Fig. 4.7a of same material having similar surface finish of optical flat and bond line thickness is prepared during the time of optical assembly realization. Fig. 4.7b shows the photograph of the lap shear sample. The dimension details of the lap shear sample are shown in Fig. 4.7c. Also about 4 grams of adhesive buttons cured on clean teflon sheet (shown in Fig. 4.7b) are used for the TML and the CVCM.

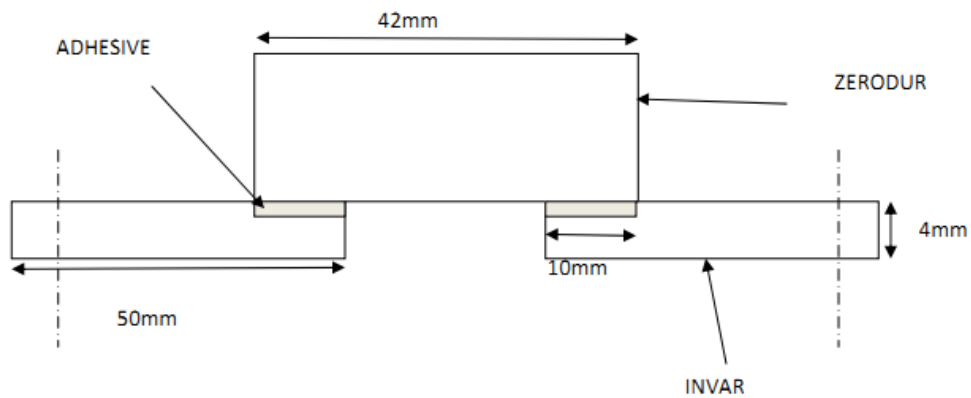


Fig. 4.7c Details of lap shear test sample

Table 4.1: Properties of adhesive Epotek-301

Parameter	Value
Number of components	2
Mix ratio	Part “A” 20% and Part “B” 5 % By weight
Cure schedule	1 hour at 65 °C 24 hrs at room temperature
Bond line thickness	0.100 mm
Lap shear strength	1700 psi (Al to Al)
Shore D hardness	81
Total Mass Loss (TML)	1.08%
Volatile condensable materials	0%
Viscosity at 25 °C Part A and B mixed	100 cps
Shelf life	1 years
Pot life (100g)	30 min
Glass transition temperature Tg	48 °C (elevated cure)
Transmission	>97% (320 to 900nm) >80% (910 to 2600 nm)
Coefficient of thermal expansion	50x 10 ⁻⁶ in/in/°C Below 40 °C 125x 10 ⁻⁶ in/in/°C Above 40 °C

Table 4.2: Properties of adhesive 3M 2216 B/A gray

Parameter	Value
Number of components	2
Color	gray
Mix ratio	Part “A” 7% and Part “B” 5 % by weight
Bond line thickness	0.125 mm
Cure schedule	2 hour at 66 °C 7 days at room temperature
Lap shear strength	3200 psi (Al to Al)
Shore D hardness	50-65
Total Mass Loss (TML)	0.77%
Volatile condensable materials	0.04%
Viscosity at 25 °C Part A and B mixed	100,000 cps
Shelf life	2 years
Pot life (100g)	90 min
Coefficient of thermal expansion	102x 10 ⁻⁶ in/in/°C Between 0-40°C 134x 10 ⁻⁶ in/in/°C Between 40-80°C

4.3.2 Evaluation Method

An experimental setup to evaluate the optical surface distortion comprises a phase shifting interferometer and a high quality 45° fold mirror are arranged as shown in the Fig 4.8.

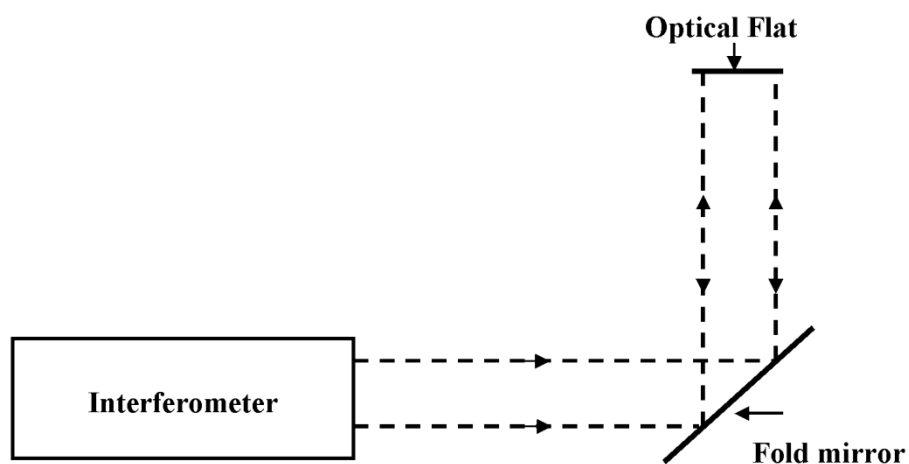


Fig. 4.8 Experimental set up for the surface figure evaluation

The optical flat is rested along its periphery on a soft teflon ring as shown in Fig. 4.9, to overcome uneven resting as well as distortion due to hard contact, with the polished surface facing the incoming light as shown in Fig. 4.10.

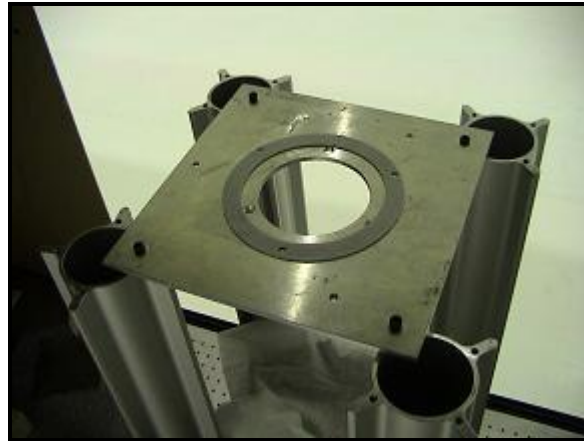


Fig. 4.9 Optical flat resting bed on the experimental setup



Fig. 4.10 Photograph of the experimental setup for the surface evaluation

The optical assembly and the lap shear samples are exposed to thermal cycling, hot soak and cold soak at 50% RH and typical thermal exposures are shown in Figs.4.11 to 4.13.

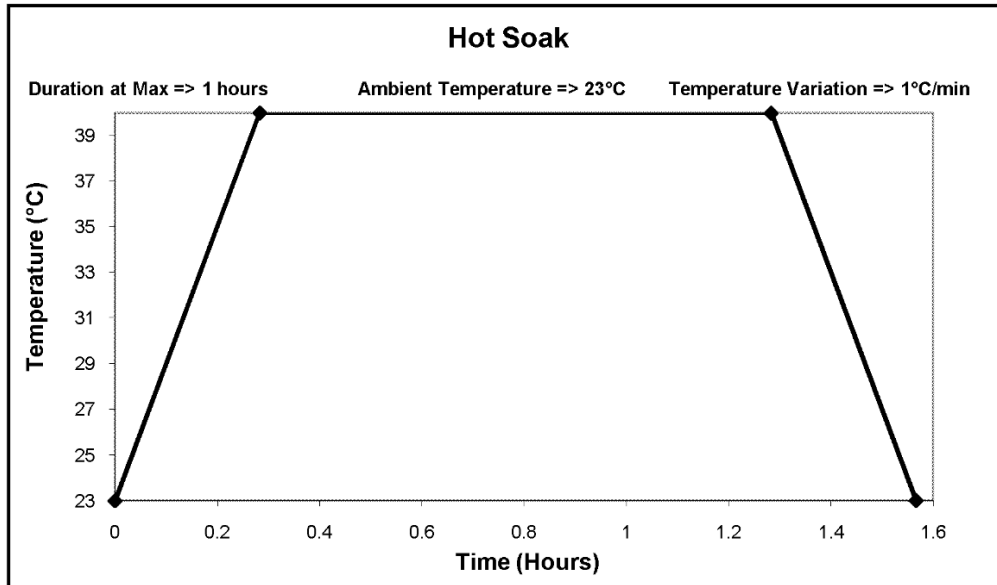


Fig. 4.11 Details of hot soak

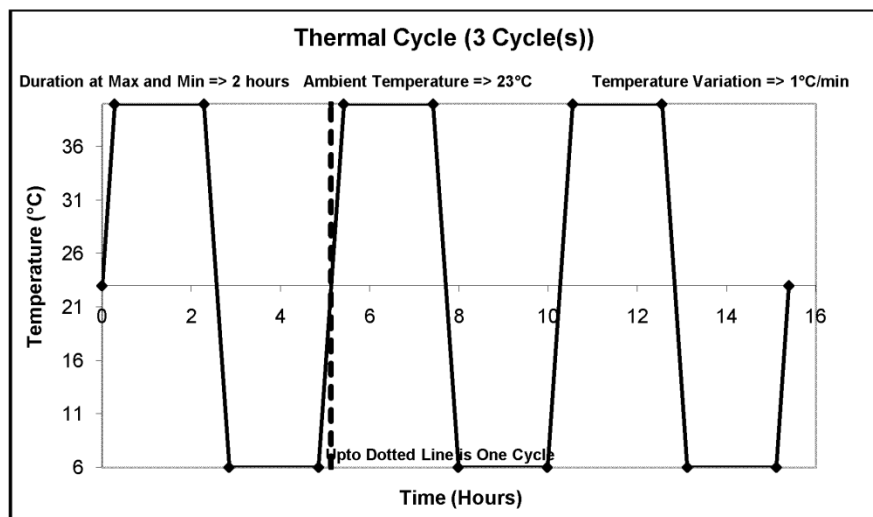


Fig. 4.12 Details of thermal cycle

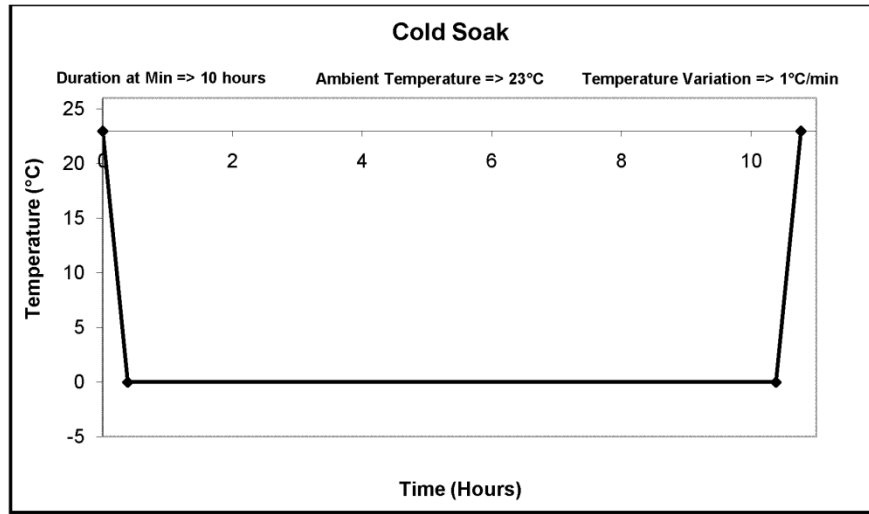


Fig. 4.13 Details of cold soak

Bonding, curing and thermal cycling of optical assemblies and lap shear test samples are carried out at ambient atmospheric pressure. The out-gas property of adhesive is estimated is carried out on the sample by subjecting it to the prescribed test condition of 10^{-6} Torr at a temperature of 125°C for 24 hours. The surface figure of the optical assembly is evaluated after curing as well as after thermal cycling in terms of root mean square error (rms) and power (surface curvature) as described in the equations 4.1 and 4.2. The interferometer test is carried out on the optical flats at $20 \pm 3^{\circ}\text{C}$, 50% RH and at ambient atmosphere pressure.

$$\text{Rms error} = (\sum Z_n^2 / n)^{1/2} \quad (4.1)$$

$$Z(X,Y) = C_0 + C_1X + C_2Y + C_3 (X^2 + Y^2)$$

$$\text{Power} = C_3 (X^2 + Y^2) \quad (4.2)$$

where, Z is out of plane deviation w.r.t reference plane, X and Y are surface Cartesian coordinates, n is number of sampled points and C_n are fitted coefficients,

The estimation of lap shear strength of the sample is carried out using an INSTRON 8031 tensile testing machine with a slow shearing rate approximately 0.15-0.25 mm/min at room temperature. The acceptance criteria on various parameters for an high resolution optics are given in table 4.3.

Table 4.3: Acceptance criteria on various parameters

Surface figure (rms)	Lap shear strength Kg / mm^2	CVCM	TML
$< 0.025(\lambda)$	> 0.8	$< 0.1\%$	$< 1.0\%$

4.4 Results

The initial (before bond) value of surface figure for 1:6 and 1:10 aspect ratio optical flats are evaluated with the flexure resting on bond area. The surface figure of optical flat (before bond) pre-bond for 1:6 aspect ratio is $\text{rms} = 0.020\lambda$ and $\text{power} = -0.008\lambda$ and for 1:10 aspect ratio is $\text{rms} = 0.020\lambda$ and $\text{power} = -0.028\lambda$ with instrument repeatability of 0.005λ rms respectively.

4.4.1 Surface distortion due to Epotek-301

The Epotek-301 forms a transparent layer after curing. The results of surface figure evaluation of assemblies with Epotek-301 are summarized in table

4.4. There is a degradation of surface figure upon adhesive curing. The post cure surface distortion decreases from 0.14λ rms to 0.04λ rms for an aspect ratio change of 1:10 to 1:6. By adopting relief bond area concept the surface distortion is reduced further to 0.03λ rms. However, there is a change in the nature and the magnitude of distortion of surface after exposing to temperature of $+40^{\circ}\text{C}$. It is curious to note that the concave surface distortion upon curing changed to convex upon post thermal. This phenomenon is consistently observed with different samples and also with different aspect ratio as given in table 4.4. It is also observed that if the temperature exposure of the relief area bonded assembly is kept within the range of 0° to $+35^{\circ}\text{C}$, the inversion of surface distortion profile is minimum between the post cure and the post thermal exposure.

Table 4.4: Surface figure of the bonded optical assembly of Epotek-301

Cases	Post cure (rms) λ	Post cure (power) λ	Post thermal (rms) λ	Post thermal (power) λ
Epotek-301 (1:10 aspect ratio exposed to 0° to $+40^{\circ}\text{C}$) 1 st thermal cycle	0.139	0.383	0.101	-0.295
Epotek-301 (1:10 aspect ratio exposed to 0° to $+40^{\circ}\text{C}$) 2 nd thermal cycle	0.139	0.383	0.171	-0.540
Epotek-301 (1:10 aspect ratio with relief bond exposed to 0° to $+40^{\circ}\text{C}$) 1 st thermal cycle	0.090	0.230	0.106	-0.314
Epotek-301 (1:10 aspect ratio with relief bond exposed to 0°	0.090	0.230	0.149	-0.462

to +40°C) 2 nd thermal cycle				
Epotek-301 (1:10 aspect ratio with relief bond cold soak at 0°C after 2 nd thermal cycle)	0.090	0.230	0.141	-0.441
Epotek-301 (1:10 aspect ratio with relief bond cold soak at -20°C after 1 st cold soak)	0.090	0.230	0.132	-0.374
Epotek-301 (1:6 aspect ratio 0° to +40°C thermal cycle)	0.041	0.073	0.134	-0.448
Epotek-301 (1:6 aspect ratio with relief bond exposed to 10° to +35°C thermal cycle)	0.034	0.053	0.029	-0.053
Epotek-301 (1:6 aspect ratio with relief bond exposed to 0° to +40°C thermal cycle)	0.034	0.053	0.078	-0.241
Epotek-301 (1:6 aspect ratio with relief bond exposed to 0° to +40°C thermal cycle)	0.034	0.053	0.085	-0.296

4.4.2 Surface distortion due to 3M 2216 B/A gray

The bonded assembly of 3M2216 B/A gray experienced an optical surface distortion of 0.020λ rms upon curing even with an aspect ratio of 1:10 and distortion of 0.025λ rms over the temperature exposure of 0° to +45°C. The results of surface figure evaluation for 3M 2216 B/A gray assemblies are summarized in table 4.5. The surface distortion in the case of 3M 2216 B/A gray

with primer is similar to that of without primer and the surface distortion is 0.022λ rms after subjecting to temperature range of $+5^\circ$ to $+40^\circ\text{C}$.

Table 4.5: Surface figure of the bonded optical assembly with 3M 2216 B/A gray

Cases	Post cure (rms) λ	Post cure (power) λ	Post thermal (rms) λ	Post thermal (power) λ
3M-2216 B/A gray (1:10 aspect ratio exposed to hot soak $+60^\circ\text{C}$)	0.020	0.017	0.020	0.014
3M-2216 B/A gray (1:10 aspect ratio exposed to $+5^\circ$ to $+40^\circ\text{C}$) thermal cycle	0.020	0.017	0.021	0.016
3M-2216 B/A gray (1:10 aspect ratio exposed to 0° to $+45^\circ\text{C}$) thermal cycle	0.020	0.017	0.025	0.025

Typical surface plot for pre-bond optical flat is shown in Fig 4.14 and surface plots for post cure and post thermal cycle for Epotek-301 and for 3M2216 B/A gray are shown in Figs. 4.15 - 4.18 respectively.

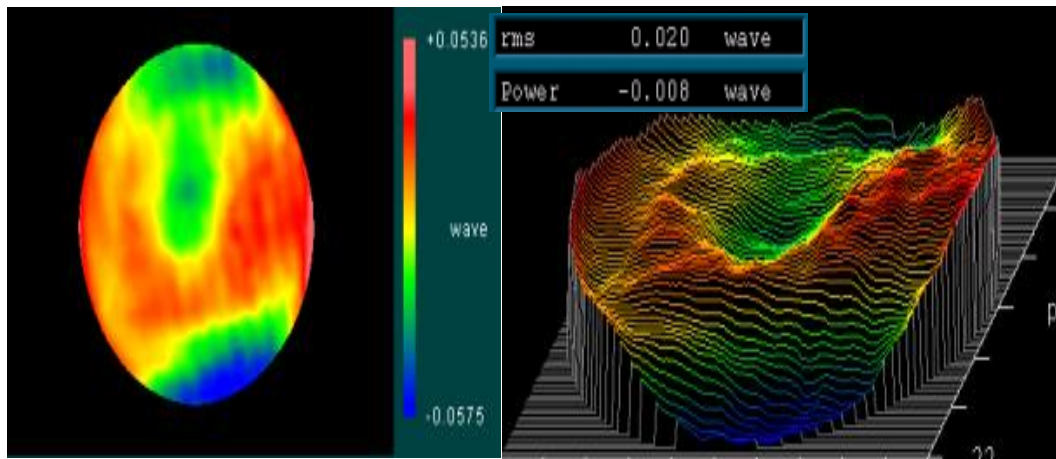


Fig. 4.14 Optical flat in free condition

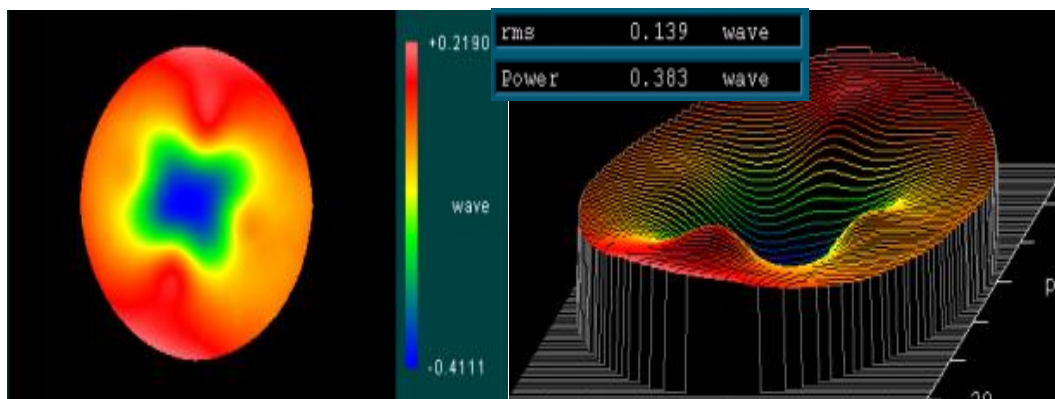


Fig. 4.15 Optical assembly with Epotek-301 upon cure

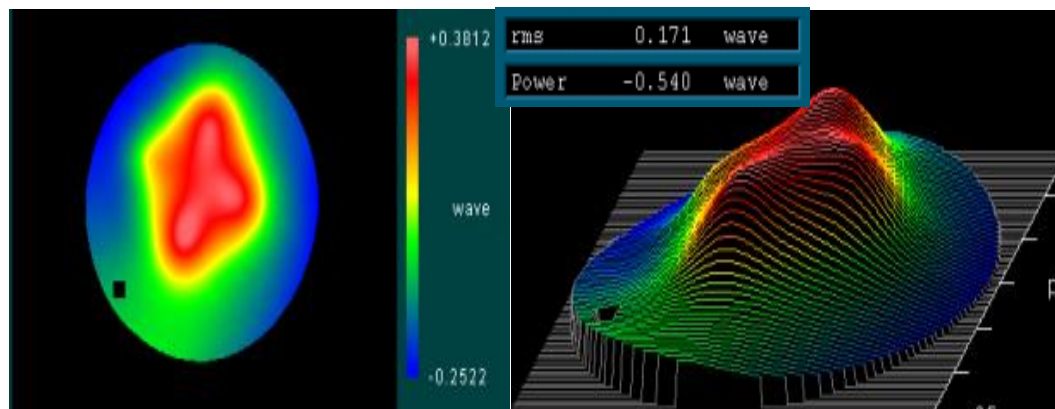


Fig. 4.16 Optical assembly with Epotek-301 upon thermal exposure (test at RT)

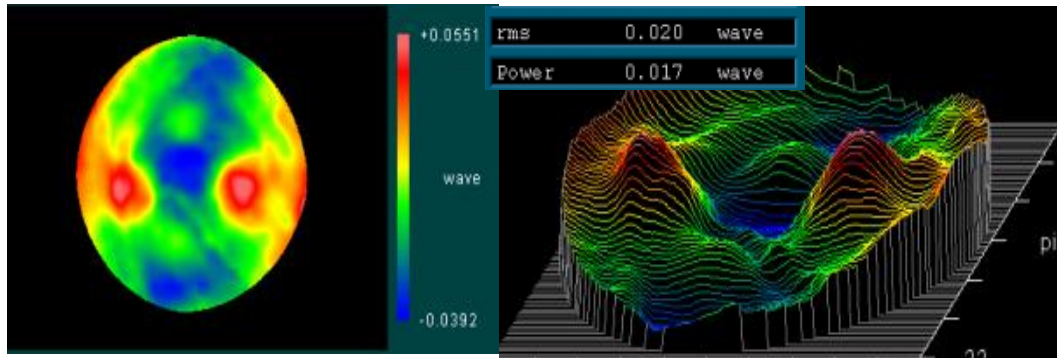


Fig. 4.17 Optical assembly with 3M 2216 B/A gray upon cure

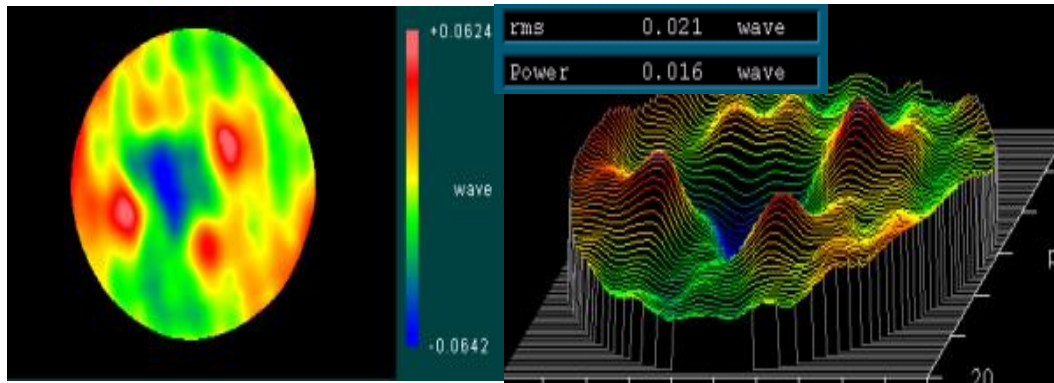


Fig. 4.18. Optical assembly with 3M 2216 B/A gray upon thermal exposure (test at RT)

4.4.3 Lap Shear Strength and Out-gas properties

The observed lap shear strength and out-gas results are given in table 4.6. A typical low thermal expansion glass possesses yield strength of $\sim 1 \text{ kg/mm}^2$. It is found that the lap shear strength of assemblies of Epotek-301 is greater than the yield strength of LTE glass and whereas the lap shear strength of 3M 2216 B/A gray is almost one-half of the yield strength of LTE glass. The reduction in lap shear strength requires larger bond area on the optical assembly and for a pre-defined bond area and load conditions, the stress at adhesive-glass interface may

exceed the lap shear strength of adhesive resulting in the detachment of glass from flexure mount. The lap shear strength of the 3M 2216 gray is found to be increased from 0.55 to 0.83 kg/mm² with the application of structural primer 3M-3901 at the bond interfaces prior to bonding. The out-gas properties of both adhesives meet the acceptance criteria as mentioned in table 4.3.

Table 4.6: Results of mean value of lap shear strength, CVCM and TML

Cases	Lap shear strength (Kg/mm ²)	CVCM %	TML %
Epotek-301	> 1*	0.001	0.81
3M-2216 B/A Gray	0.55	0.01	0.84
3M-2216 B/A Gray with primer	0.83	0.005	0.81

*glass breaks, adhesive intact between glass and mount.

4.5 Discussion

The bonded optical assembly of Epotek 301 has shown surface distortion as concave profile upon cure and as convex profile upon exposure to elevated temperature; tested at RT. The smaller aspect ratio bonded assembly has shown a pronounced surface distortion and the surface distortion reduces for the relief bond pattern assembly. However the bonded optical assembly of 3M 2216 B/A gray does not show any appreciable surface distortion. The lap shear strength of Epotek-301 is more than that of the 3M 2216 B/A gray.

Epotek-301 and 3M 2216 B/A gray are low viscous (100 cps) and high viscous (~100,000 cps) two part adhesives respectively. Low viscous adhesives have higher ability to wet the substrate and hence tend to have high adhesion. The observed high lap shear strength of Epotek-301 can be attributed to its low

viscosity. All adhesives shrink in volume during curing. Epoxies typically have about shrinkage of 3% to 5% and Young's modulus of about 100 to 1500 MPa upon cure. The stress on optical element, in general, is a function of shrinkage of adhesive upon curing and its Young's modulus (Bachmann, 2001).

Curing of adhesive is a process of forming cross linkages between polymers called cohesion and between adhesive and the substrate called adhesion. One of the ways the surface distortion upon cure can be explained by phenomena of initial formation of strong adhesion and later (cohesion) shrinkage of adhesive upon curing. The shrinkage may pull the optical surface at bond area towards the adhesive core and hence the expected nature of surface distortion is a valley (concavity) upon curing. Completely cured adhesive shall have the thermo-elastic behaviour of solid (compress on cooling and expand on heating from the RT) governed by its CTE and expected to retain the surface distortion occurred upon cure on returning to the RT. In the case of semi-cured adhesive, it is expected that further curing as well as shrinkage shall occur and lead to further deepening of the valley on exposure to hot temperature and return to the RT. Surprisingly, the observation for Epotek 301 assembly is hill (convexity) on return to the RT after exposure to +40°C. The magnitude of hill remains similar on further subjecting the bonded assembly to similar extent of cold temperature from the RT as well as further thermal cycling over similar extent of hot and cold temperatures. It is inferred that the downward pull upon cure (Fig. 4.19a) and upward push (Fig. 4.19b) upon exposure to higher temperature of optical assembly occur along the adhesive bond line. The shrinkage induced stress phenomenon is able to explain the surface distortion upon cure and it could not account for the phenomena that

cause the change in nature of surface distortion on exposure to a temperature higher than the RT. It is known that the adhesive undergoes a phase transition from glass to rubbery state above certain temperature called glass transition temperature T_g . The T_g of Epotek 301 is 48 °C for elevated curing (Technical datasheet Epo-tek 301, 1994) and 40° C (Daly, 2001) for 3M 2216 B/A gray. It is understood that upon cooling from the T_g , the mechanical and thermal properties of adhesive does not remain the same that of before heating (post-cure) to the T_g . Hence, the cause of the surface distortion due to thermal exposure may be attributed to this. However the change in the properties of adhesive on thermal exposure and its impact on surface figure profile shall be investigated in future as a new topic of research.

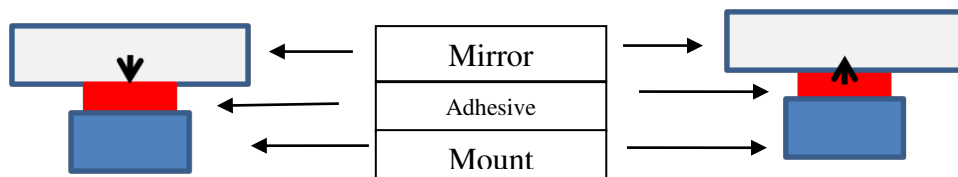


Fig. 4.19a Surface distortion phenomenon upon cure

Fig. 4.19b Surface distortion phenomenon upon exposure to 40°C (tested at RT)

Among the two space-qualified adhesives that have been chosen for the experiment, one of the adhesives (Epotek-301) has shown a peculiar phenomenon on the surface distortion. In order to establish an empirical relation that helps to identify adhesives for the space-borne high resolution optics on the basis of known properties, an extensive survey is carried out to find similar observations reported elsewhere on any other space-qualified adhesives. It is found that the

phenomenon similar to Epotek-301 assembly was observed on the mirror of Far Ultraviolet Spectroscopic Explorer (FUSE) bonded with Hysol EA9396 (Ohl et al, <http://fuse.pha.jhu.edu>). The mirror assembly had shown inversion of the initial surface distortion profile upon heating > 60°C (near to Tg of Hysol EA 9396). Table 4.7 shows the comparison of the salient properties of adhesive of Epotek 301, 3M 2216 B/A gray and Hysol EA 9396 (Technical datasheet Hysol EA 9396, 2002).

Table 4.7: Comparison of the salient properties of adhesives

Parameter	Epotek 301	3M 2216 B/A gray	Hysol EA 9396
CTE (ppm)	50 < Tg 125 > Tg	102 (0 to 40°C) 134(40 to 80°C)	70.7 at 40°C 108 at 100°C
Viscosity (cps)	100	100,000	3500
Tg	48 °C*	40°C	77°C
Shore D hardness	81	50 to 60	80
Lap shear (psi) Al-Al (surface etched)	1700	1850	4200

*Elevated temperature curing.

On comparison of all three adhesives, adhesives Epotek 301 and Hysol EA 9396 that have shown similar surface distortion phenomenon are having distinctly following aspects in common 1. low viscosity 2. high Shore D hardness and 3. inversion of the surface distortion profile near and above Tg.

Hence, it has been hypothesized that the adhesive of low viscous and high shore D hardness has more tendency to distort the optical surface upon cure and also the bonded assembly of those adhesives on exposure to temperature near and above Tg has a tendency to show inversion of the initial distortion profile

upon tested at room temperature. Properties namely viscosity, shore D hardness and Tg can be used initially as a main properties to identify the probable candidate among the declared space-qualified adhesives for the high resolution optical assembly.

4.6 New method to reduce surface distortion

In the case of Epotek-301, we propose thermal exposure approach as an alternate method to reduce the surface distortion of optics after bonding. There is a distinct sign change in the power of the surface indicating the change in the surface type i.e., from concave after curing to convex after thermal exposure shown in Figs. 4.15 and 4.16. It can be inferred that the surface distortion occur after curing for various aspect ratios can be reduced or eliminated by cycling over an appropriate temperature range (case: 8, Table 4.4, temperature range 0° to +35°C). This method may be adopted for applications where Epotek-301 used for the direct bonded mount, provided the assembly is not exposed to temperatures higher than that of exposed for the distortion reduction. Here we have suggested a thermal assisted method to reduce the adhesive-induced surface distortion upon curing for Epotek-301. However it is advised to find out the appropriate temperature range to reduce the surface distortion for the intended optical assembly.

4.7 Summary

We have here identified cases where bonded assembly of adhesive Epotek-301 fails to meet the surface figure requirement and to our knowledge that was not reported elsewhere. From the experimental results, we have also proposed

a new method i.e., thermal assisted method to reduce the surface distortion occurs upon curing against the conventional post cure polishing of the optical components. By analyzing the results of available adhesives, we hypothesize that the adhesive that is low viscous and high shore D hardness has more tendency to distort the mirror surface upon cure and also the bonded assembly of those adhesives on exposure to temperature near and above T_g has a tendency to show inversion of initial distortion profile upon tested at room temperature. Hence from those properties of adhesives one can identify the adhesive for space-borne high resolution optical system. We have found that the 3M 2216 B/A gray with primer 3901 meets the requirement of optical assemblies for visible-infrared spectrum, exposed to a temperature range of $+5^\circ$ to $+40^\circ\text{C}$ and operating at $20 \pm 3^\circ\text{C}$. The observations reported here also brings out one among the (peculiar) possibilities of degradation of image due to the distortion of optical surface occur during the development of the optical assembly.

Portion of the work is published in

“Adhesive for optical component: an implementation study,” *J. Opt.*, Springer (2012), **40**(12): 81-88.

CHAPTER 5

DESIGN OF WAVEFRONT SENSOR FOR OPTICAL SYSTEM TESTING AT EOM

5.1 Introduction

Large aperture optical system experiences gravity induced surface distortion and the profile of surface distortion varies with the holding configuration about the gravity vector. The assembly-induced and the misalignment-induced wavefront distortion are super-imposed on the gravity-induced wavefront distortion. In those cases, it is required to evaluate the optical system in terms of wavefront error and also express the wavefront distortion on a suitable set of polynomial basis; to get more insight into the nature of error in the optical system. Therefore, the alignment and testing of a high resolution optical system (telescope) is carried out using an interferometer in a retro-reflected mode as shown in Fig. 5.1 (Figoski, 1999; Gaudin-Delrieu et al, 2008; Geyl, 1994).

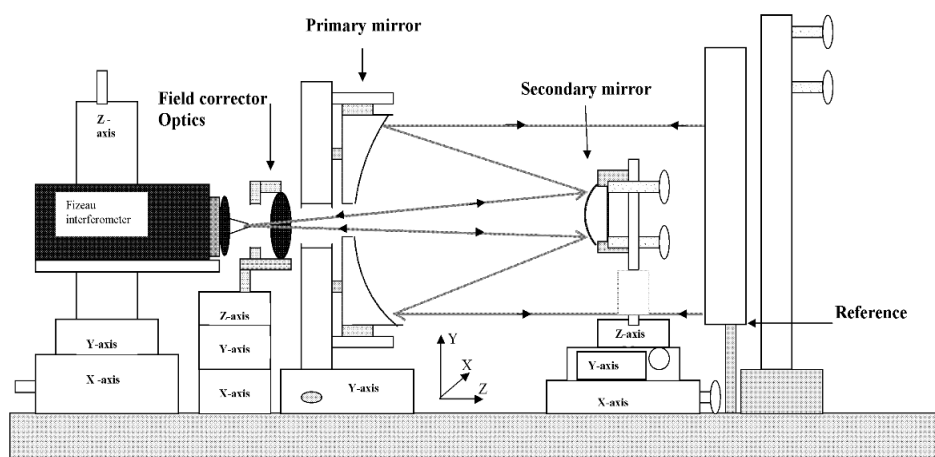


Fig. 5.1 Sketch of the Fizeau interferometer test of the optical system

In the interferometer aided test configuration, the focus of the converging beam generated using a transmission sphere attached to the interferometer is matched to the focus of the optical system. The collimated beam emerges from the optical system is retro-reflected in to the optical system using a reference flat. The optical system is evaluated on the basis of the wavefront error obtained through the interference of the reference wavefront and the retro-reflected wavefront of the optical system. In most cases, the conventional retro-reflected mode of interferometer test is not possible at the electro optical module due to the blockage of focal plane by the CCD and other processing electronics packages of the EOM. In general, in an earth observation system the CCD do not occupy entire FOV of the optical system, hence there are unoccupied portion of the FOV which can be utilized for the testing of the optical system. In this work, it is aimed at to identify a wavefront sensor which is compact, able to test the optical system in terms of wavefront during the EOM development and forms an integral part of the EOM. Tailoring of any of the earlier reported optical test methods to suit the necessary requirements is also investigated.

We have investigated a few of the test methods (Wyant, 1987; Geary, 1995) that were reported earlier for the testing of the optical system namely, (1) Polarization Shearing Interferometer (PSI) with Babinet Compensator (BC), (2) Curvature sensor and (3) Shack –Hartmann wavefront sensor (SH WFS).

The polarization shearing interferometer with Babinet Compensator (Saxena, 1979) is based on the principle of wavefront shearing techniques using polarization to obtain the wavefront distortion. Two crossed Babinet compensator

based polarization shearing interferometer configuration (Saxena et al, 1980) are used for simultaneous evaluation of wavefront in the two orthogonal directions. In this configuration, image relay optics is required to image the interference pattern on to a detector. The placement of the Babinet compensator inside the focus may interfere with the usable FOV of the optical system and also the measurement of wavefront distortion is sensitive to vibration occur during the data acquisition.

The curvature sensor (Rodier, 1988) determines the wavefront distortion by making wavefront curvature measurement at two locations, one before focus called intrafocal image and the other outside focus called extrafocal image. From the intensity distributions differences at two image planes are used to determine the wavefront distortion. This method needs movement of the detector to carry out in and out of focus measurement. Arriving at this type of measurement configuration at the focal plane optical system in the EOM is difficult and not desirable.

The Shack-Hartmann Wavefront sensor (Platt and Shack, 2001) determines the wavefront distortion from the measurement of wavefront slope (Southwell, 1980; Lane et al, 1992; Malacara et al, 1992; Jiang et al., 2005). It is compact and can be placed outside the focal plane. The Shack-Hartmann wavefront sensor uses small portion of the large FOV of the telescope, and is vibration insensitive and can be integrated with the EOM.

5.2 Principle of SH WFS

In Shack-Hartmann wavefront sensor, the wavefront is analyzed by dividing the incoming wavefront into a small areas and measuring the wavefront

slope over those areas. The Shack-Hartmann wavefront sensor has been revolutionized by the advent of microlens array and high speed detector elements fabrication technologies.

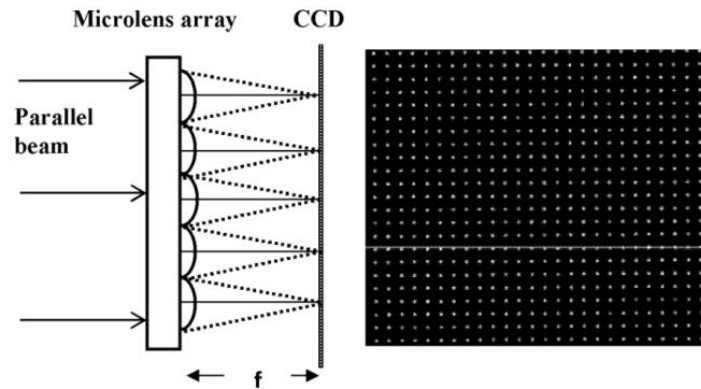


Fig. 5.2 Image spot corresponds to sampling of incident wavefront by the SH WFS

The presence of aberration in the wavefront alters the local slope of the wavefront. In the Shack-Hartmann wavefront sensor, an incoming wavefront is spatially sampled by the MLA. The MLA (of focal length f_{MLA}) in turn forms light spot at its focal plane. These light spots are recorded by area array detector elements kept at the focal plane of the lenslet array (shown in Fig. 5.2). The displacement (Δd) of the focal spot with respect to focal spot location of an unaberrated wavefront corresponds to the mean local wavefront tilt θ across that lenslet aperture as shown in Fig 5.3. The local slope of the wavefront can be expressed as,

$$\tan(\theta) \approx \theta = \frac{\Delta d}{f_{MLA}} \quad (5.1)$$

Once the wavefront slope is obtained the wavefront can be reconstructed using various numerical integration methods. Since we are interested in the evaluation of lower order wavefront aberration, the modal reconstruction method suits well (Dyson; 2011). In the modal reconstruction the wavefront phase (path difference) is expressed by a set of polynomials,

$$W_\phi = \sum_k a_k Z_k(x, y) \quad (5.2)$$

where a_k is the coefficients of the polynomial and Z_k is the polynomial basis functions (modes).

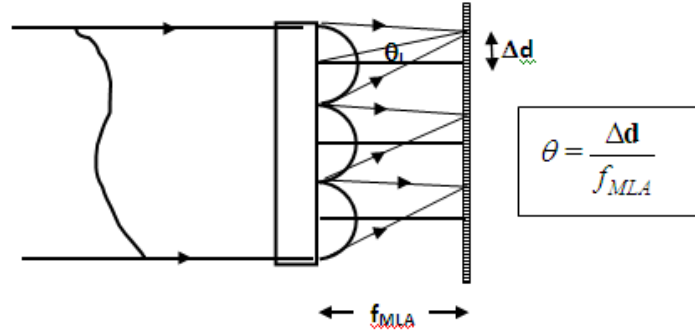


Fig. 5.3 Displacement of image spot due to change of local wavefront tilt

The SH WFS determines the gradient of the incident wavefront along x and y directions as $\theta_x = \frac{\partial W}{\partial y}$ and $\theta_y = \frac{\partial W}{\partial x}$ respectively corresponding at various n positions on the wavefront defined by the MLA coordinates. There are total $N=2n$ slope values corresponding to x and y directions determined from the n measured positions and from Eq. (5.2) it can be expressed as set of linear equations,

$$\left. \frac{\partial W}{\partial x} \right|_n = \sum_k a_k \left. \frac{\partial Z_k}{\partial x} \right|_n \quad (5.3)$$

$$\left. \frac{\partial W}{\partial y} \right|_n = \sum_k a_k \left. \frac{\partial Z_k}{\partial y} \right|_n \quad (5.4)$$

This can be written in more general form as

$$s = [\Delta Z]. a \quad (5.5)$$

where s is the slope vector, ΔZ is the first derivative of the polynomial basis function (mode) and a is the coefficient of mode. There are number of polynomial basis functions those can be used as modal functions. The basis sets may not be orthogonal but it should be linearly independent functions. One can overcome the lacuna of the orthogonality of the basis sets by expressing the wavefront phase using all the required modal coefficients. By defining the merit function as the sum of the squares of the differences between the actual value and the estimated value of s from the $[\Delta Z].a$, the elements of the modal coefficient vector a can be determined using the least squares method.

5.3 Polynomial representation of wavefront

The aim of the optical testing is to evaluate the image forming characteristics of the optical system. The imaging forming characteristics of the optical system can be derived from the knowledge of wavefront at the exit pupil. If the wavefront is continuous and smooth then it can expressed by a suitable set of basis function (Malacara, 1992). The aberration polynomial are used to express the wavefront distortion occur due to optical aberration. The wavefront distortion due to the primary aberration is expressed as (Malacara, 1994),

$$W(x, y) = A(x^2 + y^2)^2 + B(x^2 + y^2) + C(x + 3y^2) + D(x^2 + y^2) + Ey + Fx + G \quad (5.6)$$

A = spherical aberration coefficient

B = coma coefficient

C = astigmatism coefficient

D = defocusing coefficient

E = tilt about the x axis

F = tilt about the y axis

G = constant or piston term

The general form to express the wavefront that includes all the high order aberrations is,

$$W(x, y) = \sum_{i=0}^k \sum_{j=0}^i c_{ij} x^j y^{(i-j)} \quad (5.7)$$

5.3.1 Zernike polynomial representation

The wavefront aberration over a circular pupil can be conveniently expressed by the Zernike polynomials. Individual terms of the Zernike polynomials are easily correlated to the classical aberrations of the optical system. In the Zernike polynomial the non-rotationally symmetric aberrations namely coma and astigmatism are decomposed into two components along the orthogonal axes (x and y axes) of the optical system and z axis being the optical axis. However those orthogonal components can be combined to form the classical Siedel aberrations (Malacara 1992). Also the Zernike polynomials are orthogonal polynomial over the circular aperture (Lakshminarayanan et al, 2011; Mahajan, 1981; Dai et al, 2008), which means the inclusion or exclusion of a particular term of the polynomial do not affect the coefficient of the other terms of the polynomial. The Zernike coefficients can be determined from the wavefront slope measurements by least squares fitting of the derivatives of Zernike polynomial

after orthogonalisation as described in (Mahajan, 2013). The wavefront at the exit pupil can be expressed as a linear combination of Zernike circular polynomial as,

$$W(\rho, \theta) = \sum_{n=0}^k \sum_{m=0}^n A_{nm} U_{nm} \quad (5.8)$$

$$U_{nm} = R_n^{n-2m} \begin{cases} \sin \\ \cos \end{cases} (n-2m) \theta \quad (5.9)$$

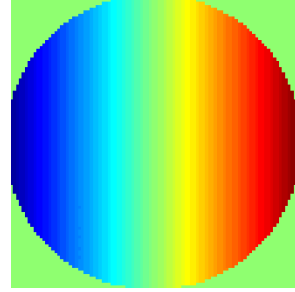
where n is the degree of polynomial and m is the azimuth frequency. The sine function is used for $(n-2m) > 0$ and the cosine function for $(n-2m) < 0$. A positive number m was defined as

$$m = \frac{n-l}{2} \quad (5.10)$$

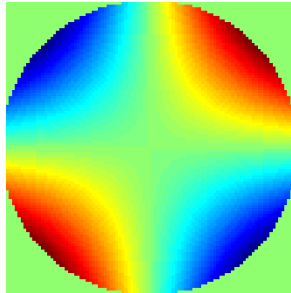
$(n-l)$ is always an even number, and that $n > l$.



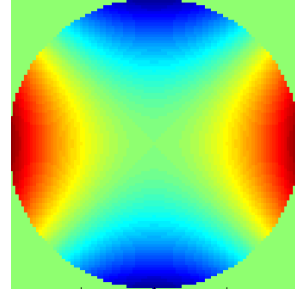
5.4a Tilt about x



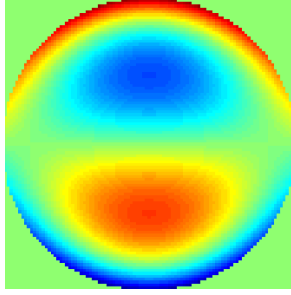
5.4b Tilt about y



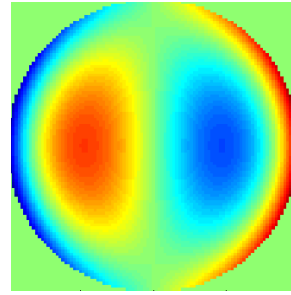
5.4c Astig $\pm 45^\circ$



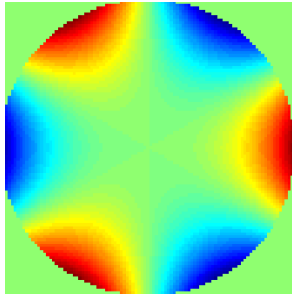
5.4d Astig $0 / 90^\circ$



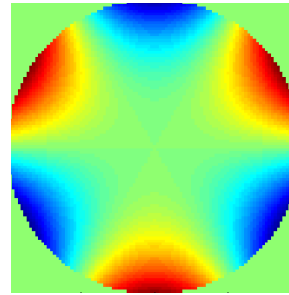
5.4e Coma X



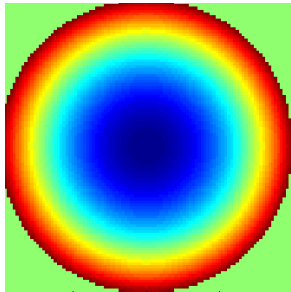
5.4f Coma Y



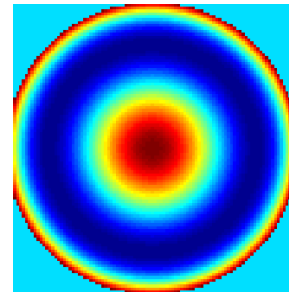
5.4g Trefoil base at x



5.4h Trefoil base at y



5.4i Focus



5.4j Spherical

5.4 Contour plot of various Zernike polynomial modal coefficients

Figures 5.4a to 5.4k are the graphical representations of the lower-order modes of Zernike circular polynomials. The lower-order Zernike circular polynomial is presented in table 5.1.

Table 5.1: Lower-order Zernike circular polynomials

n	m	Zernike polynomial in polar coordinates	Zernike polynomial in Cartesian coordinates	Aberration
0	0	1	1	Piston
1	0	$\rho \sin \theta$	x	Tilt about y
1	1	$\rho \cos \theta$	y	Tilt about x
2	0	$\rho^2 \sin 2\theta$	$2xy$	Astig with axis $\pm 45^\circ$
2	1	$2\rho^2 - 1$	$-1 + 2y^2 + 2x^2$	Focus shift
2	2	$\rho^2 \cos 2\theta$	$y^2 - x^2$	Astig with axis $0^\circ/90^\circ$
3	0	$\rho^3 \sin 3\theta$	$3xy^2 - x^3$	Trefoil base on x
3	1	$(3\rho^3 - 2\rho) \sin \theta$	$-2x + 3xy^2 + 3x^3$	Coma along x
3	2	$(3\rho^3 - 2\rho) \cos \theta$	$-2y + 3xy^2 + 3y^3$	Coma along y
3	3	$\rho^3 \cos 3\theta$	$y^3 - 3x^2y$	Trefoil base on y
4	2	$6\rho^4 - 6\rho^2 + 1$	$1 - 6y^2 - 6x^2 + 6y^4 + 12x^2y^2 + 6x^4$	spherical aberration

The first derivatives ΔZ of lower-order Zernike polynomials can be conveniently expressed as in table 5.2. Hence, the Zernike polynomials are used as the modal basis function in Eq. (5.2).

Table 5.2: First derivatives of the lower-order Zernike circular polynomials

Zernike polynomial x derivative	Zernike polynomial y derivative	Aberration
0	0	Piston
1	0	Tilt about y
0	1	Tilt about x
2y	2x	Astig with axis $\pm 45^\circ$
2(2x)	2(2y)	Focus shift
-2x	2y	Astig with axis $0^\circ/90^\circ$
$3y^2-3x^2$	6xy	Trefoil base on x
$3(3x^2+y^2-1)$	3(2xy)	Coma along x
3(2xy)	$3(x^2+3y^2-1)$	Coma along y
-6xy	$3y^2-3x^2$	Trefoil base on y
$2(12x^3+12xy^2-8x)$	$2(12y^3+12xy^2-8y)$	spherical aberration

5.4 Proposed test scheme at EOM

At the integrated electro optical module, the rear of the focal plane of optical system is populated with detector and its associated electronics. Nevertheless, certain small portion of unused FOV of the focal plane of the optical system can be used for the Shack-Hartmann wavefront sensor based evaluation. A collimator that is generally used for the contrast evaluation method and for the determination of detector plane of the optical system in the EOM is utilized for this proposed scheme. The outline of the proposed test set is shown in

Fig. 5.5. The optical system converge the incident parallel beam from the collimator to the focal plane. The proposed SH WFS is required to evaluate the converging wavefront at the focal plane of optical system. Since the SH WFS requires a collimated wavefront at the MLA, the converging beam is collimated using a convex lens. The convex lens and the SH WFS are placed behind the focal plane at an appropriate location in the EOM within the corrected FOV (space between the two CCD lines as the case shown in Fig. 5.5). The angular position of the EOM with respect to the collimator can be re-established at any time using the optical alignment cube of the EOM.

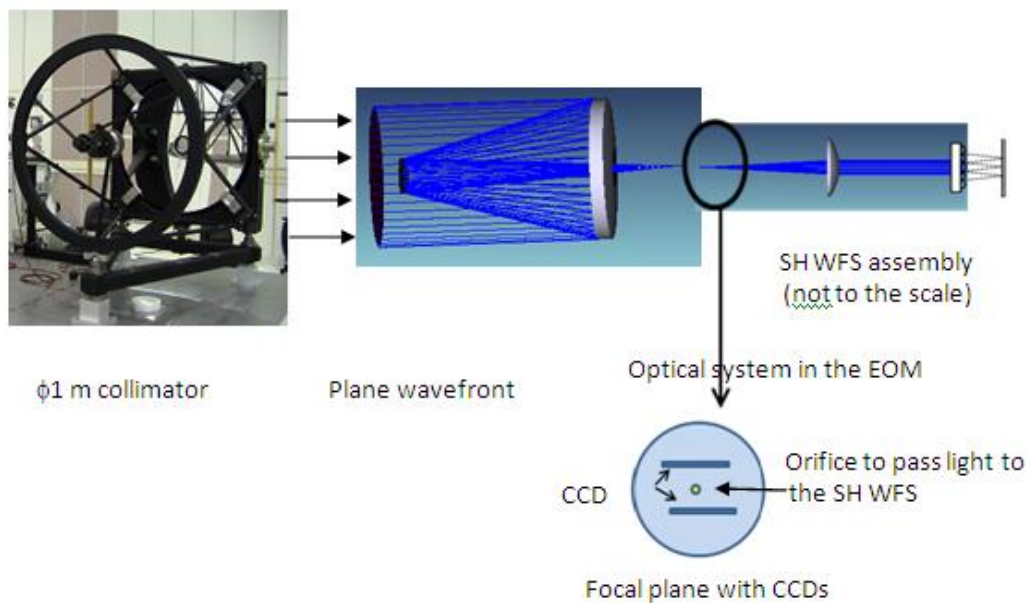


Fig. 5.5 Outline of the proposed EOM test set with the SH WFS

5.5 Design of SH WFS

Typical wavefront deformations of a large aperture optical system ($\sim \phi=700$ mm) held by three rear flexure mounts with gravity vectors along axial and radial directions are shown in Figs. 5.6b and 5.6c respectively against the zero gravity condition as in Fig. 5.6a. On ground, the assembly and misalignment

induced wavefront distortion of optical system are super-imposed on the gravity induced wavefront distortion. Hence, the envisaged SH WFS shall be tailored to meet all those requirements. As the variations on the wavefront of these types of optical systems are smooth, it can be fully expressed by lower-order aberrations. Though numerous modes form the lower-order wave aberrations, the significant lower order modes and their magnitude can be estimated through optical and opto-mechanical simulations (Geary, 2002; Doyle et al, 2002). Primarily the SH WFS is required to monitor the significant changes in the wavefront error and hence, the coefficients of Zernike polynomial modes of an aligned optical system during various qualification tests. Therefore, the primary design goals of the SH WFS are,

1. The significant modes considered here for the wavefront reconstruction are the first ten modes (excluding piston) of the fringe Zernike polynomial.
2. The minimum magnitude of measurement (dynamic range) of wavefront deformation shall be at least 1.25 times of the estimated magnitude of various modes through optical and opto-mechanical simulations viz. defocus ~ 200 nm and component astigmatism (x or y) or trefoil (x or y) ~ 633 nm depends on the gravity vector otherwise ~ 63 nm.
3. The maximum determination uncertainty of any of the coefficients of Zernike polynomial modes shall be < 25 nm.

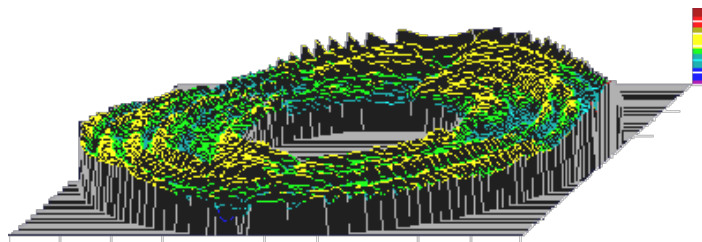


Fig. 5.6a Surface plot of wavefront deformation at zero 'g'

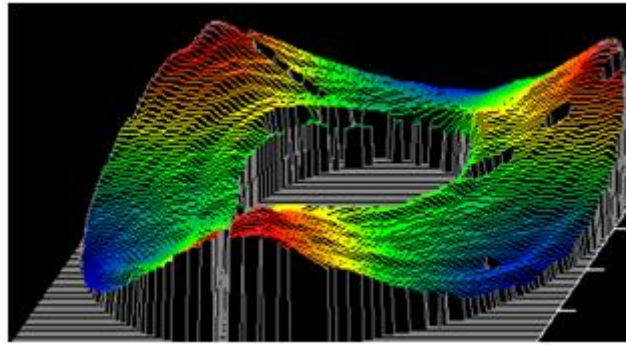


Fig. 5.6b Surface plot of trefoil deformation of wavefront

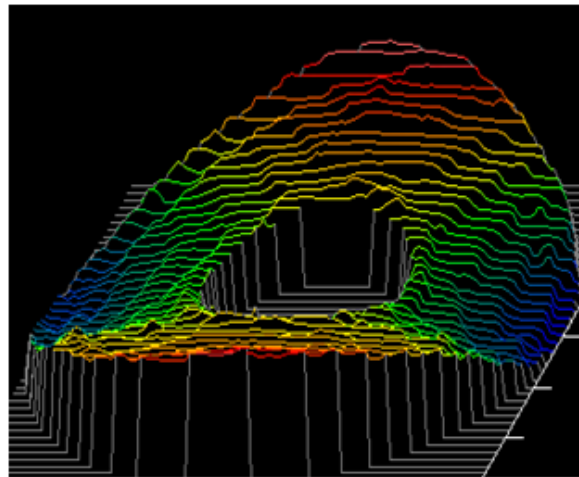


Fig. 5.6c Surface plot of astigmatic deformation of wavefront

The design of an SH WFS is all about defining the parameters of the SH WFS to meet the required goals. In the SH WFS, the wavefront is sampled by the MLA and the spatial sampling of wavefront depends on the aperture size (pitch) and number of the microlenses (samples) of the MLA. The ability (accuracy) to retrieve the wavefront improves with more number of microlenses that are used for sampling the wavefront. For a given pitch of the MLA, the longer the focal length of microlens the longer is the light spot displacement. The longer light spot displacement improves the accuracy of measurement of tilt that in turn helps to

improve measurement of the minimum wavefront deviation. It is necessary for an automated spot finding routine, to limit the displacement of light spot within the window ‘w’ defined by the aperture or pitch of the MLA to overcome the cross talk between the microlenses. This constraint along with image spot spread due to diffraction reduces the maximum range of light spot displacement and hence, the measurement of maximum wavefront deviation. The permissible light spot displacement can be expressed as,

$$\theta_{\max} = \frac{1}{2f\#} - \frac{\lambda}{d} \quad (5.11)$$

where $F\#$ is the F-number, f_{MLA} is the focal length, d is the side of square aperture of the microlens and λ is the wavelength of light. The amount of displacement of light spot for various magnitude of coefficient of Zernike polynomials can be determined by rewriting Eq. (5.5) as,

$$\Delta d = f_{MLA} [\Delta Z] a \quad (5.12)$$

A reverse analysis is carried out to determine the aperture, number of microlens and focal length of the MLA that are required to meet dynamic range and accuracy. It was reported (Widiker et al, 2006) that the light spot shall at least be sampled by eight pixels to achieve a light spot position error <0.01 pixel. In the reverse analysis, first step is to find the permissible light spot displacement using Eq. (5.11) for various square-aperture (pitch) sizes of microlens viz. 0.4, 0.5 and 0.6 mm with different focal lengths. Also it is to find the focal length required to meet the light spot position determination criteria for a given detector and microlens pitch. The second step is to find the minimum number of microlenses required to meet the required wavefront determination accuracy. This is arrived at

by finding the difference in the wave rms error computed for the full dynamic range of measurement with large number of samples, say 100x100 and then with a reduced number of samples such that it meets the required accuracy. The third step is to find the light spot displacement for the full dynamic range of measurements by Eq. (5.12) for the different MLAs arrived at from the earlier steps and its compliance to the permissible limit of displacement. The fourth step is to find the uncertainty in the measurement due to the determination error on the parameters of the SH WFS.

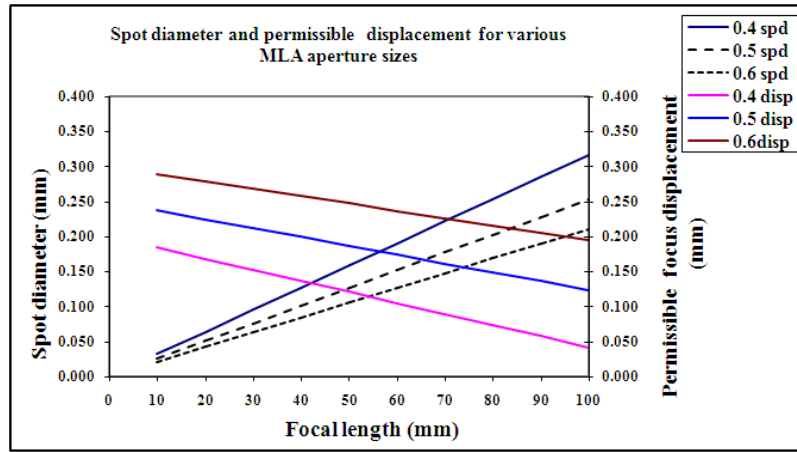


Fig. 5.7 Image spot spread and the permissible displacement

Figure 5.7 shows the light spot spread (primary axis) and the permissible light spot displacement (secondary axis) for various microlens focal lengths. The set of three ascending lines corresponds to the light spot diameter and the other set of three lines corresponds to the permissible light spot displacement. The intersection of the ascending and descending lines of a particular microlens aperture gives the focal length for which the light spot diameter and the permissible light spot displacement occupy the allowable window 'w' equally. All other focal lengths any one of the above parameter occupy the allowable window

more. For a detector of pixel pitch of 0.012 mm, one can notice from Fig. 5.7 that the light spot spread of the 0.4, 0.5 and 0.6 mm aperture microlenses with $f=32$, 40 and 48 mm respectively satisfies the light spot position determination criteria (Widiker et al, 2006). The respective permissible light spot displacement for those cases is 0.150, 0.200 and 0.249 mm. A 20x20 microlens array is considered for the SH WFS, since the difference of wave rms error between a 100x100 and a 20x20 sampling array is $< 2\%$. Fig. 5.8 shows the extent of light spot displacement for the maximum intended magnitude of various Zernike polynomial modes and the limit of displacement within the window 'w' for all three cases of SH WFS.

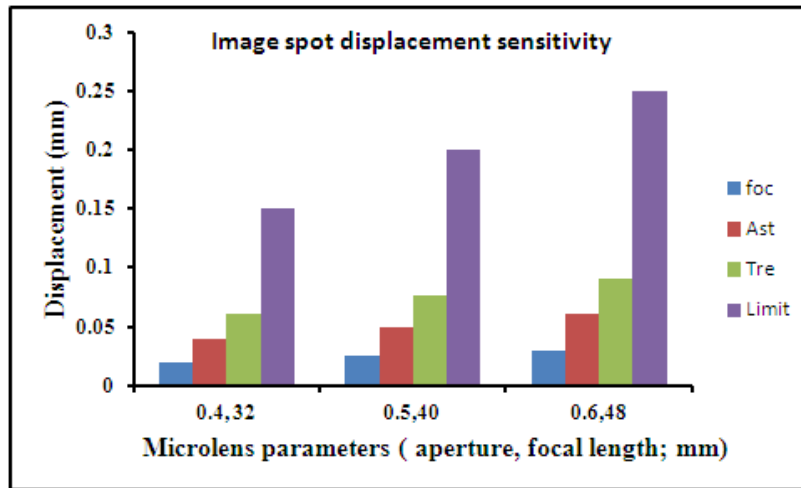


Fig. 5.8 Image spot displacement for the expected magnitude modal coefficient with different microlens aperture

The required dynamic range of all three cases is found to lie within the permissible limit. The SH WFS of $f=48$ mm, pitch = 0.6 mm MLA has 13 % more dynamic range than that of the $f=32$ mm, pitch = 0.4 mm. For compaction, we prefer to use a smaller focal length SH WFS. An error analysis is carried out on the parameters of the SH WFS to find the uncertainty in the determination of the coefficients of Zernike polynomial. The details of the identified off-the-shelf

MLA and the CCD for the SH WFS are given in table 5.3. The parameters of the SH WFS and their maximum uncertainties are listed in table 5.4.

Table 5.3: Details of the MLA and the CCD

MLA Parameters	Value	CCD Parameters	Value
Make	AOA	Make	IMPERX
Pitch	0.328 mm	Pixel size	0.009 mm
Focal length, Number of microlens	24 mm, 44 x 44	Pixel format	4000 x 2672

The error in the determination of light spot positions and the variations in the focal length of microlenses within the MLA are simulated in a way that random values generated from a normal distribution of a given mean and standard deviation, such that the maximum random value generated is equal to the expected maximum variation (using Matlab command *normrnd*). The nominal slope vector is modified with the displacements arise due to those uncertainties and then least squares fitted as in Eq. (5.5) to find the new set of Zernike polynomial modal coefficients. The measurement uncertainty arise due to the determination error in the axial separation between the MLA and the CCD is estimated by first generating light spot displacements Δd for the full dynamic range with the $(f_{MLA} + \Delta)$ by Eq. (5.12) and then calculating the slope vectors with the f_{MLA} . The calculated slope vectors are used to compute the new set of coefficients of Zernike polynomials. The expected maximum uncertainty in the retrieved Zernike modes is given in table 5.4.

Table 5.4: Expected uncertainty in the retrieved Zernike modal coefficient

S.no	Parameter	Value (mm)	Zernike coefficient maximum uncertainty (nm)
1	Maximum difference in the f among the microlenses	± 0.5	1.5
2	Maximum error in the separation between the MLA and the CCD	± 0.5	12
3	Maximum error in the estimation image spot position (centroid)	0.0001	7.5

The algebraic sum of error of Zernike modes is 21 nm against the design goal of < 25 nm.

5.6 Summary

We have investigated and identified a test method based on the Shack-Hartmann wavefront sensor for the evaluation of the optical system at EOM. The method is compact, can be integral part of the EOM and the measurements are vibration insensitive. We have identified and described the scheme for the testing of the optical system at EOM with this method. We have carried out detailed design and analysis of the SH WFS that meets the requirements of testing of the optical system at electro optical module and also found that the estimation error (i) in the axial separation between the MLA and the CCD and, (ii) in the light spot position are the major contributors to the retrieval of modal coefficients.

Portion of the work is published in

“Design and development of Shack-Hartmann wavefront sensor- based testing of high resolution optical system for earth observation,” *Opt. Eng.*, (2014) **53**(11):11410.

CHAPTER 6

DEVELOPMENT AND VERIFICATION OF WAVEFRONT SENSOR FOR OPTICAL TESTING AT EOM

6.1 Introduction

Micro lens array and charge coupled device are the basic elements of a Shack-Hartmann wavefront sensor. As we have found in the chapter-5 that it is necessary to ensure the parameters of the SH WFS within the required tolerance so as to achieve the desired accuracy on the measured Zernike modal coefficient. In view of this, we have developed techniques to characterize the MLA and also the Shack-Hartmann wavefront sensor. The proposed test methodology of testing of the optical system using the developed SH WFS has been demonstrated in a simulated-system. The results obtained with the SH WFS are cross-verified with an *in situ* evaluation configuration using a standard interferometer.

6.2 Methods of MLA characterization

In an SH WFS, the MLA spatially samples the incident wavefront and forms two dimensional arrays of image spot in the focal plane as shown in Fig. 6.1. The local slope of the incident wavefront is obtained from the displacement of centroid of image spot from the optic axis of each microlens. The MLA for the SH WFS is typically embedded on one side of a high surface quality plane glass plate with antireflection coated on non-microlens portion. The knowledge of microlens parameters such as focal length, diameter and pitch are crucial for the

accurate estimation of wavefront slope in the SH WFS (Pfund et al, 1998; Neal et al, 2002). Owing to the large number of small sized and small numerical aperture microlenses within the two dimensional layout, the measurement of focal length of the MLA is not easy. Traditionally the focal length of each microlens of the MLA is obtained indirectly by substituting the measured radius of curvature in the basic thin lens formula. The radius of curvature of each microlens can be arrived at by measuring the sagitta over its diameter using a travelling microscope (Bardina et al, 2007; Zhuet al, 2012). The radius of curvature can also be obtained from the separation between the cat-eye and confocal positions either using a reflective compound microscope or with a Twyman-Green interferometer (Reichelt et al, 2005). The focal length of microlens can be directly estimated with a Mach-Zehnder interferometer configuration (Reichelt et al, 2005) and also based on the measurement of image position and the size of an object placed at a finite distance using a reflective compound microscope (Cholletand et al, 2009). All those methods are tedious since the measurement has to be repeated one after other microlenses within the MLA.

6.3 Spherical wavefronts method

A direct estimation of the MLA parameters in the SH WFS configuration can be found by fitting the difference between measured and reference spherical wavefront curvature to a quadratic polynomial basis (Chernyshov et al, 2005) or from the light spot measurement of two different spherical wavefronts (Yang et al, 2010). Those methods use a semiconductor laser coupled to a single mode fiber to generate a spherical wavefront. It was reported (Chernyshov et al, 2005; Yang et

al, 2010) that the measurements are sensitive to the tilt of spherical wavefront with respect to the MLA. Therefore, an additional arrangement was incorporated to minimize the tilt error. Even then the test setup requires a reconfiguration between the measurement and the tilt monitoring (Chrnyshov et al, 2005). We have proposed an experimental configuration for the focal length measurement as shown in Fig. 6.1, which does not require any test setup reconfiguration.

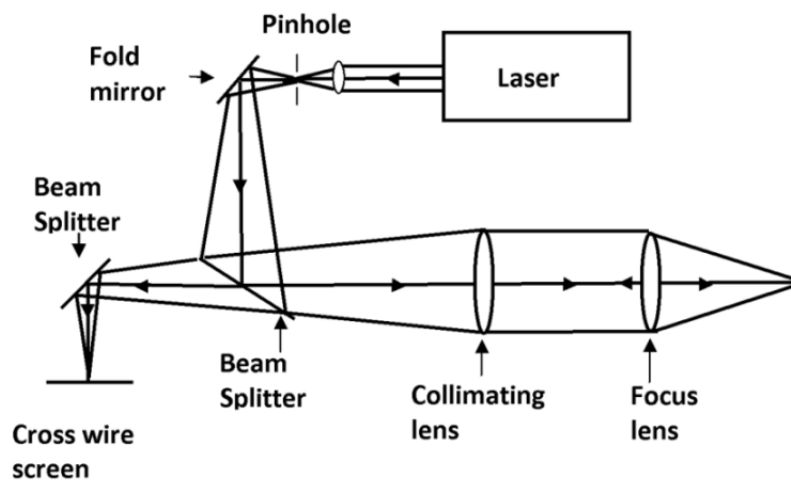


Fig. 6.1 Proposed experimental configuration for the spherical wavefront method

The proposed experimental configuration is realized using the provisions available with a standard Fizeau interferometer (Malacara, 1992). The align mode provision of the interferometer, which is meant for matching the center of pinhole image of the test and the reference wavefront, is used for monitoring the tilt of the plane of the MLA with respect to the local normal of the spherical wavefront. The transmission sphere attachment of the interferometer is used for the generation of a spherical wavefront. The proposed method and uncertainty in the focal length measurement are experimentally demonstrated with an off-the-shelf MLA.

6.3.1 Theory

The MLA is illuminated with a diverging spherical wavefront generated by an axially placed point source at a distance R from it. The sagitta (in other words, path difference) of the incident spherical wavefront at a point on the MLA for $R \gg (x^2 + y^2)$ can be expressed as

$$\phi(x, y) \approx \frac{(x^2 + y^2)}{2R} \quad (6.1)$$

where x and y are the Cartesian coordinates of the point on the MLA.

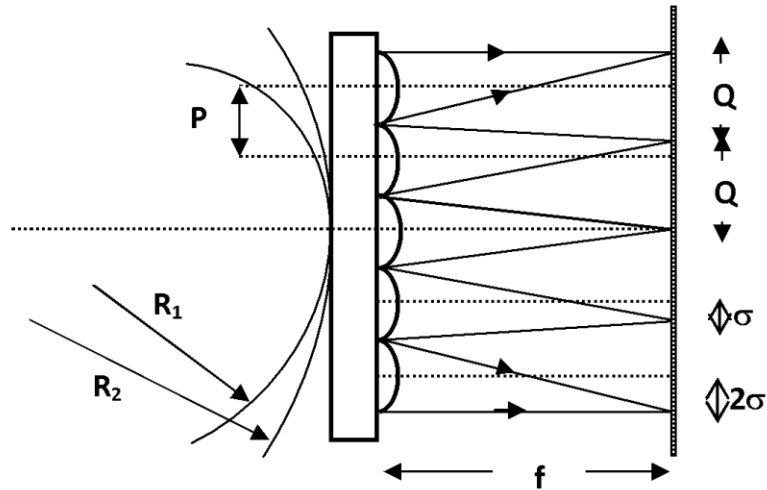


Fig. 6.2 Image spot at the MLA focal plane for a spherical wavefront

The mean slope of the wavefront over the aperture and the displacement of light spot from the optic-axis of microlens number k along x and y directions are given in Eqs. (6.2) and (6.3), where f_k is the focal length of the microlens number k .

$$\frac{\partial \phi}{\partial x} = \frac{x_k}{R} \text{ and } \frac{\partial \phi}{\partial y} = \frac{y_k}{R} \quad (6.2)$$

$$\sigma(x_k) = \frac{f_k \partial \phi}{\partial x} \text{ and } \sigma(y_k) = \frac{f_k \partial \phi}{\partial y} \quad (6.3)$$

The light spot pattern formed by the MLA for a spherical wavefront is shown in Fig. 6.2. The displacement of light spot between adjacent microlens increases by $\sigma_x = \sigma(x_k) - \sigma(x_{k-1})$ and $\sigma_y = \sigma(y_k) - \sigma(y_{k-1})$ in two transverse directions of the image. Therefore, the distances Q_x and Q_y between adjacent light spots in the image plane in two directions are constant and they can be determined by Eq. (6.4),

$$Q_x = P + \sigma_x \text{ and } Q_y = P + \sigma_y \quad (6.4)$$

By substituting Eqs. (6.2) and (6.3) in Eq. (6.4) and $f = f_k = f_{k-1}$

$$Q_x = P + \left\{ f \frac{x_k - x_{k-1}}{R} \right\} \text{ and } Q_y = P + \left\{ f \frac{y_k - y_{k-1}}{R} \right\} \quad (6.5)$$

where P is the distance (pitch) between center of adjacent microlenses. In this method, since both f and P are unknown in Eq. (6.5), as an approximation, P in the both directions of the MLA is assumed constant. Therefore Eq. (6.5) can be expressed as,

$$Q = Q_x = Q_y = P + \left(f \frac{P}{R} \right) \quad (6.6)$$

Eq. (6.6) can be rewritten as,

$$R = \frac{fP}{Q - P} \quad (6.7)$$

In practical situations, the focal length of adjacent microlenses is not the same. Hence the f in Eq. (6.7) corresponds to the mean focal length of adjacent microlenses that are used to arrive at the values of Q . In order to generate wavefronts of different curvatures the point source is placed axially at various distances from the MLA. The tilt α of the spherical wavefront with respect to the MLA induces error in the determination of axial separation R as,

$$\frac{\partial R}{\partial \alpha} = R_0 \sin(\alpha) \quad (6.8)$$

($R=R_0$ for $\alpha=0$). Hence it is necessary to control the tilt of the spherical wavefront with respect to the MLA during the axial translation. Also it was suggested that a more convenient and accurate way (Yang et al, 2010) is to measure the separation ΔR between the two positions of the point source rather than the separation between the MLA and the point source. The distances between adjacent light spots in the image plane for the two positions of point source are Q_1 and Q_2 . Hence from Eq. (6.7),

$$\Delta R = R_1 - R_2 = \left(\frac{fP}{Q_1 - P}\right) - \left(\frac{fP}{Q_2 - P}\right) \quad (6.9)$$

Eq. (6.9) is rearranged for f as,

$$f = \frac{(Q_1 - P)(Q_2 - P)}{(Q_2 - Q_1)P} \Delta R \quad (6.10)$$

The light spot intensity formed by the microlens is sampled by two dimensional pixels of the CCD. The location of the light spot x (*or* y) is determined by finding the centroid of sampled light spot intensity. The centroid x_c

(or y_c) is computed in a window (w) of pixels defining the aperture of a microlens, starts from (j_1, k_1) pixel to (j_n, k_n) pixel. For high flux condition, threshold limited intensity center of gravity method is widely adopted (Thomas et al, 2006; Neal et al, 1998; Ares et al, 2004) for the estimation of centroid as given in Eq. (6.11). In a threshold limited intensity, the peak intensity value within the window “ w ” is determined first and the threshold intensity value is set to 11% of the peak intensity value (Neal et al, 2002). Then, the pixels having intensity value less than the threshold is set to zero and the pixels having intensity more than threshold is set to their intensity value minus the threshold intensity value. Threshold limiting of intensity $I_{j,k}$ at each pixel helps to limit the centroid estimation within the first ring of the airy disc and also to reduce the effect of camera noise on the centroid estimation.

$$x_c = \frac{\sum_{j,k \in w} I_{j,k} x_{j,k}}{\sum_{j,k \in w} I_{j,k}} \quad (\text{or}) \quad y_c = \frac{\sum_{j,k \in w} I_{j,k} y_{j,k}}{\sum_{j,k \in w} I_{j,k}} \quad (6.11)$$

The focal length f_{MLA} of MLA corresponds to the mean focal length of all microlenses within the area of interest of the MLA. Therefore, for the determination of the f_{MLA} , the CCD chip has to be placed at the focal plane of the MLA. We have proposed here a procedure to locate the focal plane of microlens; hence the MLA. We define an intensity spread measure I_s for a microlens for a normal incident plane wavefront as the ratio of sum of threshold limited intensity in a square pixel region of $[(I_x, I_y), (J_x, J_y)]$ to a square pixel region of $[(M_x, M_y), (N_x, N_y)]$, where the region $[(I_x, I_y), (J_x, J_y)]$ is approximately one-half of and centered within the pixel region of $[(M_x, M_y), (N_x, N_y)]$. The side of the

square pixel region $[(M_x, M_y), (N_x, N_y)]$ is approximately $2\lambda F/\#$ and centered around the peak intensity of the microlens. We have also calculated the I_s for various image plane separations z ; starting from outside to inside focus. In order to establish the relation between the calculated I_s and the z , typical microlens of various $F/\#$ s are modelled in the Zemax optical design software. The trend analysis of the calculated I_s for various z is found to fit well with a cubic polynomial (correlation coefficient $R^2 > 0.999$). Therefore, the relation between the I_s and the z is expressed as,

$$I_s = az^3 + bz^2 + cz + d \quad (6.12)$$

Also at the focal plane position, the I_s is supposed to be maximum, hence at maxima

$$\frac{dI_s}{dz} = 3az^2 + 2bz + c = 0 \quad (6.13)$$

The positive root obtained by solving Eq. (6.13) defines the location of the focal plane of the microlens. Therefore, the intensity spread measure I_s of the MLA, obtained from the mean of I_s of all microlenses, at various z is used to determine the focal plane location z_f of the MLA.

6.3.2 Error Analysis

The determination of the f_{MLA} is a function of mean value of all adjacent light spot displacements viz. Q_1 , Q_2 and ΔR , therefore, the partial derivative of f_{MLA} with respect to Q_1 , Q_2 and ΔR in Eq. (6.10) gives the measurement sensitivity. The error E of the measurement of spherical wavefront method can be expressed as,

$$E = \sum \partial f_{MLA} = \left\{ \frac{\Delta R}{P(Q_2 - Q_1)^2} Q_2 - P^2 \partial Q_1 \right\} - \left\{ \frac{\Delta R}{P(Q_2 - Q_1)^2} (Q_1 - P)^2 \partial Q_2 \right\} + \left\{ \frac{(Q_1 - P)(Q_2 - P)}{(Q_2 - Q_1)P} \partial \Delta R \right\}$$

(6.14)

The error E in Eq. (6.14) can be represented as standard deviation $\sigma_{f_{MLA}}$

$$\sigma_{f_{MLA}} = \sqrt{\left(\frac{\partial f_{MLA}}{\partial Q_1}\right)^2 \sigma_{Q_1}^2 + \left(\frac{\partial f_{MLA}}{\partial Q_2}\right)^2 \sigma_{Q_2}^2 + \left(\frac{\partial f_{MLA}}{\partial \Delta R}\right)^2 \sigma_{\Delta R}^2} \quad (6.15)$$

6.2.3 Measurement procedure

The experimental setup consists of a 4-in Zygo™ GPI HS interferometer, a F/#7.1 transmission sphere, a five –axes (tip-tilt and three linear axes) TS compatible mount fitted on an optical rail, a MLA (Adaptive Optics Associates 0328-24-S-44x44) and a CCD (IMPERX-IPX-11M5-L) as shown in Fig. 6.3.

The details of the MLA and the CCD are given in the Table 6.1. The MLA on tip-tilt mount is assembled on a linear translator to vary its position with respect to the CCD. The photograph of the experimental setup is shown in Fig. 6.4. By axially displacing the TS mounted on the five axes stage generates different spherical wavefront curvatures with respect to the MLA.

Table 6.1: Catalogue parameters of MLA and CCD camera

MLA parameters	value	CCD camera parameters	value
Make	AOA 0328-24-S-44x44	Make	IMPERX-IPX-11M5-L
Pitch (mm)	0.328	Size (μm)	9
Number of microlens	44x44	Number of pixels	4000x2672
Focal length (mm)	24	Separation between CCD chip to flange (mm)	6.85
Surface figure (μm)	0.16	Digitisation	12 bits

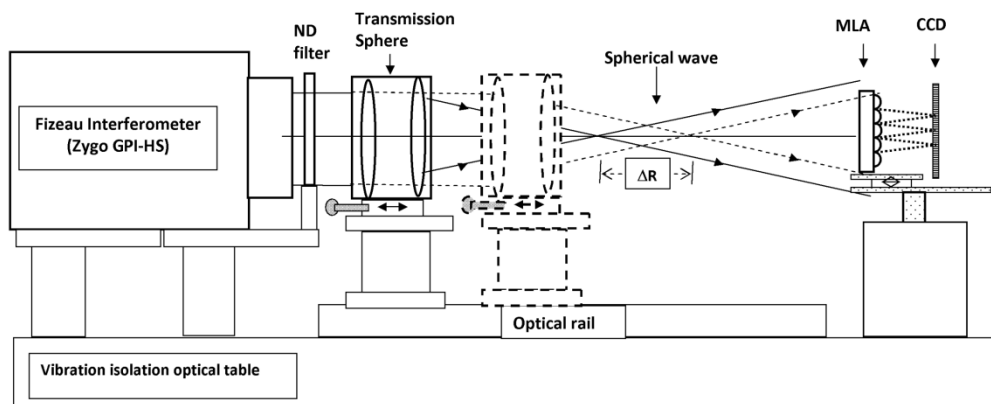


Fig. 6.3 Sketch of the interferometer based experimental setup for spherical wavefront

The measurement procedure consists of the following steps:

1. To start with, the MLA is kept at some distance in front of the CCD so that the CCD chip is outside the focus of the MLA. The CCD camera and the MLA are aligned normal to the collimated beam of the interferometer using the align mode provision of the Zygo interferometer. The MLA forms light

spots on the CCD for the incident collimated beam and the light spots are recorded for multiple times.

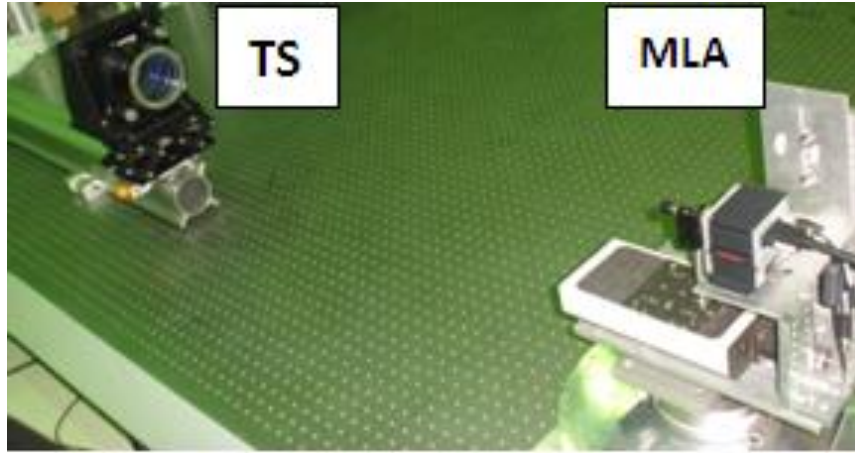


Fig. 6.4 Photograph of the interferometer based experimental setup for spherical wavefront method

2. The MLA is displaced along z and at regular spacing intervals, the light spots are recorded such that the CCD chip lies outside the focus in the start and inside the focus at the end.
3. The focal plane location z_f of the MLA is determined as in Sec.6.3.1 and the CCD chip is placed at the focal plane z_f of the MLA.
4. The diverging spherical wavefront is generated by the TS, which is kept axially at a sufficient distance away from the MLA so that image spot is contained within the window (w) defining the aperture of a microlens, and the TS is aligned normal to the interferometer. The light spots formed by the MLA are recorded.
5. The TS is displaced axially away from the MLA and at least two more point source separations the light spots are recorded. Also light spot recording are repeated at these positions for more times. The TS is aligned

normal to the MLA after every translation using the align mode provision of test setup.

6.3.4 Results and Discussion

It was reported earlier (Yoon et al, 1996) that the estimation of the centroid of light spot improves by averaging a few frames of image. In order to arrive at the centroid estimation error σ_c , 120 light spot measurements are recorded for normal incident plane wavefront. From the 120 measurements the root mean square of centroid difference of light spot are computed for an average of 5, 10, 15 and 20 measurements.

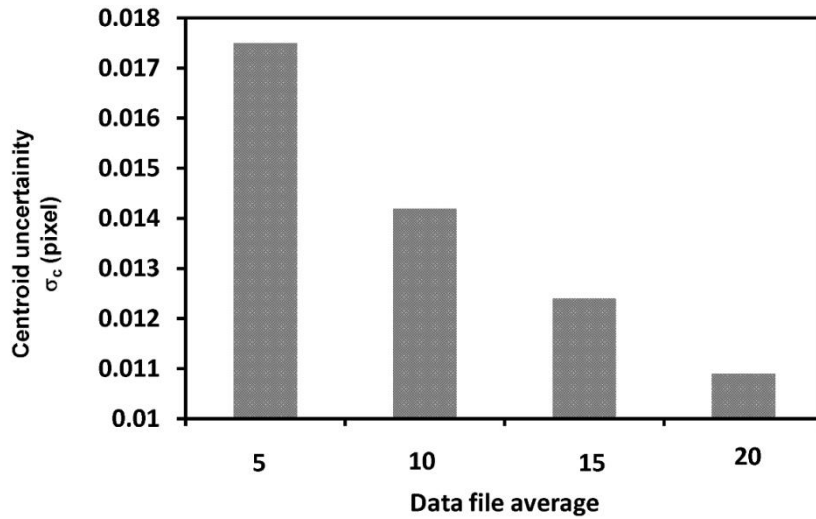


Fig. 6.5 Centroid estimation error σ_c for various image spot measurement averages.

It can be inferred from Fig. 6.5 that the centroid estimation error σ_c reduces with more number of measurements average and found to be 0.01 pixel (9×10^{-5} mm) from an average of 20 measurements. The error induced in the adjacent point source separation $\Delta R = 500$ mm for a tilt $\alpha = 1^\circ$ is 8.7 mm by Eq. (6.8). However, with the in-built align mode provision of the interferometer, the

tilt of the spherical wavefront, generated by the TS with respect to the MLA is controlled < 20 arc sec. Therefore, the error induced due to the tilt of point source in the ΔR is insignificant (for $\Delta R = 500$ mm the error is 0.05 mm). The measurement uncertainty in σ_{Q1} and σ_{Q2} arises from the σ_c . The intensity spread measure I_s of microlens is obtained by taking the ratio of sum of threshold limited digital number of 5x5 pixels to sum of the digital number of 9x9 pixels with their center at the peak DN of the microlens. The intensity spread measure I_s of the MLA at various z is shown in Fig. 6.6.

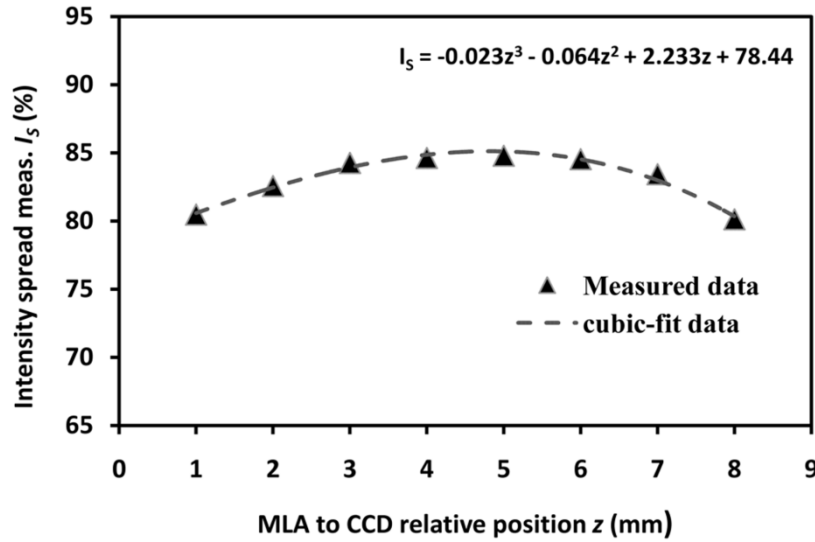


Fig. 6.6 Plot of intensity spread measure for various image plane separations

The location of the focal plane z_f of the MLA is obtained by fitting the I_s to a cubic polynomial in z . The fitted cubic polynomial expression is

$$I_s = -0.0232z^3 - 0.064z^2 + 2.233z + 78.44$$

$$\text{At the focal plane, } \frac{dI_s}{dz} = -0.0696z^2 - 0.1282z + 2.2333 = 0$$

The positive root of the above quadratic equation and hence the location z_f of the focal plane of the MLA is 4.82 mm in this test setup. In the experiment,

the image spots recording are carried out for three different point source (TS) distances from the MLA viz. 1700, 1950 and 2200 mm and also the measurements are repeated twice.

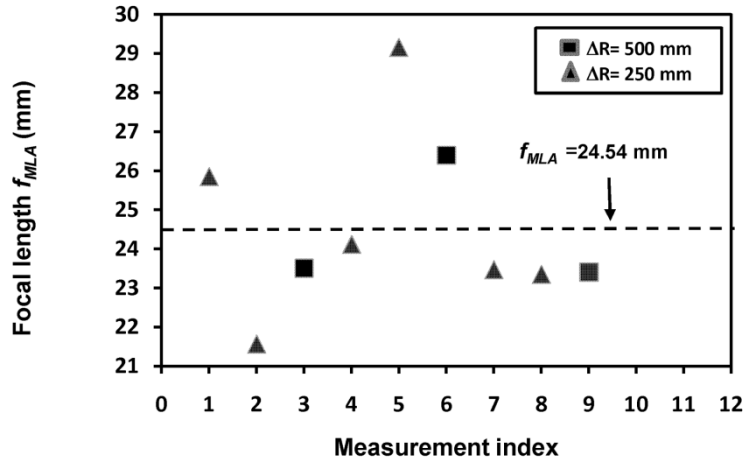


Fig. 6.7 Estimated focal length for various TS relative measurement positions

For longer separations between the TS and the MLA, the measurement criticality has been encountered due to air turbulence and light intensity at the CCD plane. The focal length of the MLA is calculated from 18x18 microlenses of the MLA. The f_{MLA} is estimated from the nine relative position measurements (shown in Fig. 6.7) and the mean f_{MLA} is 24.54 mm against the catalogue value of 24 mm. It is found that the deviation of individual f_{MLA} with respect to its mean value is large. Since the estimation of f_{MLA} from the each relative position measurements is independent, it is expected that a greater number of relative position measurements is required to achieve a mean f_{MLA} that is nearer to the true value. The same measurement strategy is required to be adopted to estimate the separation between the MLA and the CCD less than 0.5 mm to ensure the

maximum modal coefficient uncertainty < 12 nm. Also this method gives the average focal length of adjacent microlenses not the individual.

6.4 Plane wavefront method

We have proposed another method using plane wavefront method that estimates the focal length of each microlens directly and also for all lenses within the MLA simultaneously. This method is based on the measurement of transverse displacement of image spot in the focal plane of the MLA for a change of angle of incidence of plane wavefront. The proposed plane wavefront method is compact, easy to align and utilizes the existing interferometer test setup meant for the surface figure measurement of the MLA substrate. The interferometer is used for simultaneous generation of plane wavefront and measurement of angle of incidence at the MLA. The image spots formed by the MLA for the plane wavefront are recorded using a charge coupled device (CCD) as shown in Fig. 6.8.

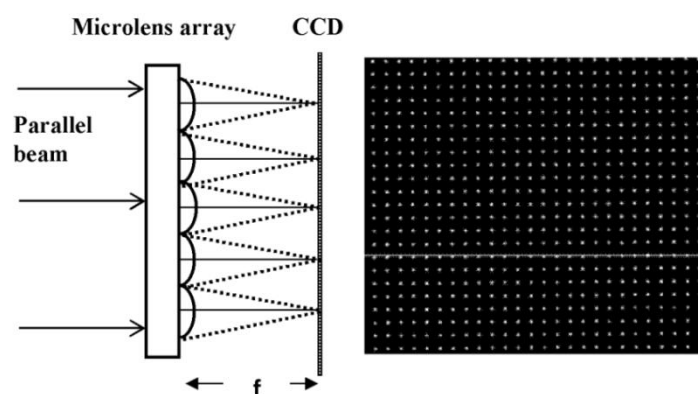


Fig. 6.8 Image spots at the focal plane of MLA for a plane wavefront

The position, i.e., the transverse displacement of the light spot of each microlens is computed from the recorded intensity distribution.

6.4.1 Theory

Each microlens in the MLA is a large f-number plano-convex lens. For an incident plane wavefront, the microlens forms diffraction limited image spot in the focal plane separated by f from the principal plane. A plane wavefront of normal incidence ($\theta = 0^\circ$), the microlens forms image (light) spot at the intersection of focal plane and optic-axis, and deviates to off optic-axis for other non-normal incidence wavefronts ($\theta \neq 0^\circ$) as shown in Fig. 6.9.

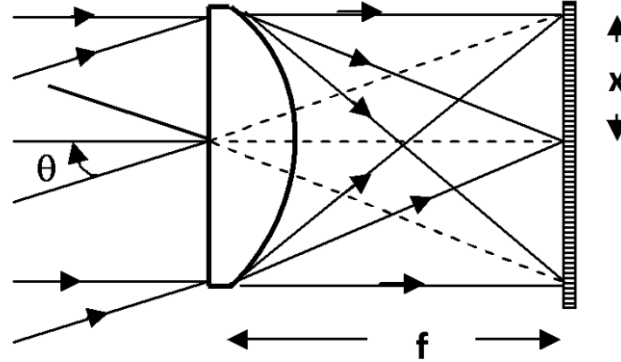


Fig. 6.9 Position of the light spot for various angles of incident plane wave at the
MLA focal plane

The position of image spot x_i in the focal plane of microlens for a plane wavefront of angle of incidence θ_i at the optic axis can be obtained from

$$x_i = f \tan(\theta_i) \approx f \theta_i \quad (6.16)$$

where $i=1\dots n$; θ is small and expressed in radians. Hence there will be ‘n’ equations formed with Eq. (6.16) and it can be solved for the f using the least squares method. The focal length f_{MLA} of the MLA is calculated by averaging the focal length f of all microlenses within the MLA.

The angle of incidence θ of plane wavefront, in other words, the tilt of microlens, can be determined using an interferometer. Interference occurs between light reflected from the reference surface of interferometer and the microlens substrate surface. Equi-distant straight line interference fringes (Jenkins and White, 2001) are produced in the case of pure tilt between the reference and the microlens substrate surfaces as shown in Fig. 6.10. The tilt θ between the surfaces gets manifested as phase difference ϕ in the interferogram and it can be obtained by Eq. (6.17).

$$\theta = \frac{\phi}{L} \quad (6.17)$$

where L is the length of surface over which the phase difference is calculated.

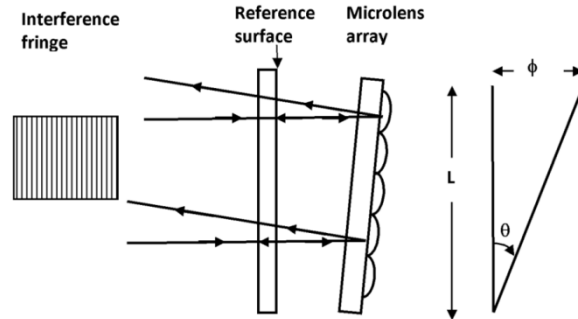


Fig. 6.10 Schematic of interference of light between tilted plane surfaces

A phase shifting interferometer can be used for the measurement of phase difference. The phase shifting interferometer (Schreiber et al., 2007) measures the intensity rather than the fringe center; hence, it enables measurement of large phase difference corresponding to a large tilt. The phase shifting interferometer is used not only for the measurement of large tilt angle but also for the measurement of phase difference ϕ with better accuracy. For the determination of the f_{MLA} , the CCD chip has to be placed at the focal plane of the MLA. As is mentioned in Sec. 6.1.2, the focal plane of the MLA is determined from the intensity spread measure I_S for various image plane separations z .

6.4.2 Error Analysis

In the case of plane wavefront method, the determination of focal length f is a function of estimation of the image spot location x and measurement of angle θ of incidence of the plane wavefront. Therefore, the sensitivity of f to θ and x is found by taking partial derivative of Eq. (6.16). The error E_p of the measurement of plane wavefront method can be expressed as,

$$E_p = \sum \partial f = \frac{\partial x}{\theta} - \frac{x \partial \theta}{\theta^2} \quad (6.18)$$

The error E_p in Eq. (6.18) can be represented as a standard deviation

$$\sigma_{fp} = \sqrt{\left(\frac{\partial f}{\partial \theta}\right)^2 \sigma_{\theta}^2 + \left(\frac{\partial f}{\partial x}\right)^2 \sigma_x^2} \quad (6.19)$$

6.4.3 Measurement procedure

The experimental setup for the plane wavefront method consists of an interferometer, a microlens array and a CCD as shown in Fig. 6.11.

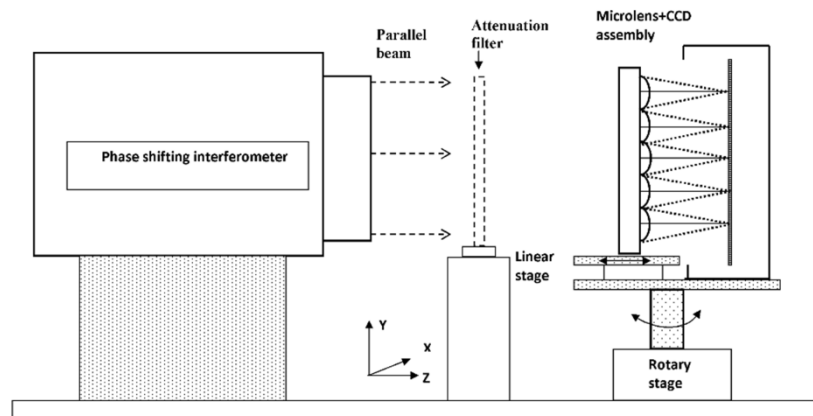


Fig. 6.11 Schematic of experimental set up of the plane wavefront method

The interferometer employed for this experiment is Zygo corporation make 4-in aperture Fizeau phase shifting interferometer (ZygoTM GPI HS). The MLA on a tip-tilt mount is assembled on a linear translation stage of 50 mm traverse with 0.020 mm read out. The MLA assembly and the CCD camera are mounted on single mechanical fixture, which in turn mounted on a rotary stage as shown in Fig. 6.11. The CCD camera and the MLA are aligned normal to the interferometer using the align mode provision of the Zygo interferometer. Photograph of the experimental setup is shown in Fig. 6.12. A 0.5-in square aperture out of the 4-in diameter circular parallel beam of 1 mw He-Ne laser light obtained at the output port of interferometer is only required for this experiment.

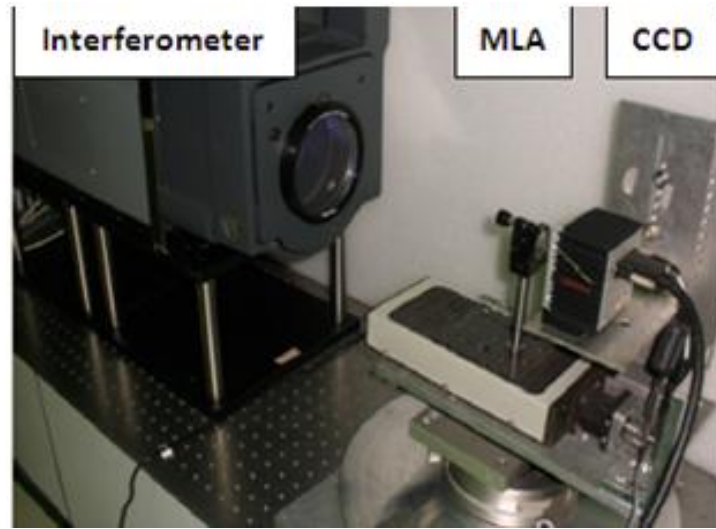


Fig. 6.12 Photograph of experimental set up of the plane wavefront method

A part of the emergent laser light intensity is reflected from the reference surface (transmission flat) and goes back into the interferometer, forming the reference beam and the other part is transmitted. The transmitted plane wavefront intensity refracts through the MLA. A part of refracted light gets reflected from the substrate surface nearer to the MLA forming the test beam. Both reference and test beams interfere and form the interference pattern. The tilt of reference and test beams, hence angle of incidence θ is obtained from the fringes (Metropro reference guide, 2004). The remaining part of refracted plane wavefront focuses on the CCD camera forming the light spots. An intensity attenuation filter is placed in between the transmission flat and the MLA during the recording of light spot, so as not to saturate the CCD pixel, as shown in Fig. 6.11. The attenuation filter is aligned normal to the interferometer each time using the align mode provision of the Zygo. The imaged light spots are acquired by an “Epix-Xcap Ltd” data acquisition system.

The measurement procedure consists of the following steps:

1. To start with the MLA is kept at some distance such that the CCD chip is outside the focus of the MLA and also aligned for a normal incident plane wavefront ($\theta = 0^\circ$) from the interferometer.
2. The MLA is displaced along z and at regular spacing intervals the light spots are recorded for 20 times such that the CCD chip lies outside the focus in the start and inside the focus at the end.
3. After determining the focal plane location z_f of the MLA as mentioned in Sec 6.3.1, the CCD chip is placed at z_f .
4. The angle of incidence of plane wavefront with the MLA is measured using the interferometer and the light spots are recorded using the CCD for 20 times.
5. The above step (4) is repeated for various angles of incidence of plane wavefront by tilting the rotary stage.

6.4.4 Results and Discussion

The angle of incidence of plane wavefront at the MLA is measured with the phase shifting interferometer. A typical angle measurement result obtained with the interferometer is shown in Fig. 6.13.

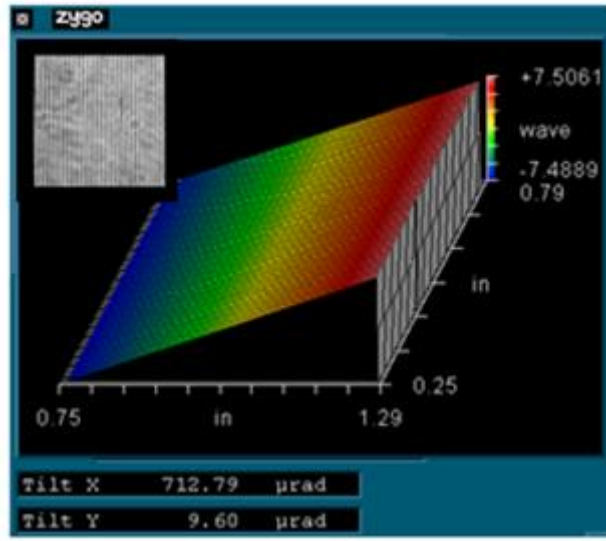


Fig. 6.13 Typical measured tilt θ between the plane wavefront and the MLA
(Inset: interference fringes)

Nevertheless, the repeatability of the phase shifting interferometer is high; the angle of incidence of plane wave is obtained by averaging multiple measurements. The standard deviation of the measured incident angle σ_θ (tilt) is $1.5 \mu\text{rad}$. It can be noted that the measurement uncertainty of σ_x , σ_{Q1} and σ_{Q2} arise from the centroid estimation error σ_c of the light spot. We have computed the focal length measurement error of plane wavefront method σ_{fp} and spherical wavefront method σ_{fs} with the observed measurement error of $\sigma_c = 9 \times 10^{-5} \text{ mm}$ and $\sigma_\theta = 1.5 \mu\text{rad}$ for a MLA of $f_{\text{MLA}} = 24 \text{ mm}$, $P = 0.3283 \text{ mm}$. The focal length measurement error σ_{fp} for the plane wavefront method and σ_{fs} for the spherical wavefront method computed through Eqs. (6.19) and (6.15) are shown in Figs. 6.14 and 6.15 respectively. In the case of spherical wavefront method, the separation ΔR between two positions of the point source can be measured more accurately and hence $\sigma_{\Delta R} = 0$ in Eq. (6.15). It can be inferred from Figs. 6.14 and 6.15 that the focal length measurement error of the plane wavefront method is by

1 order of magnitude less sensitive to that of the spherical wavefront method for the observed errors in this test set up.

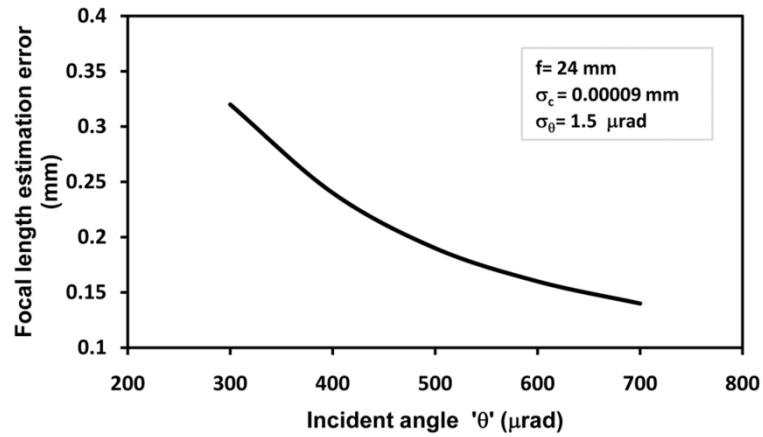


Fig. 6.14 Sensitivity of the plane wavefront method

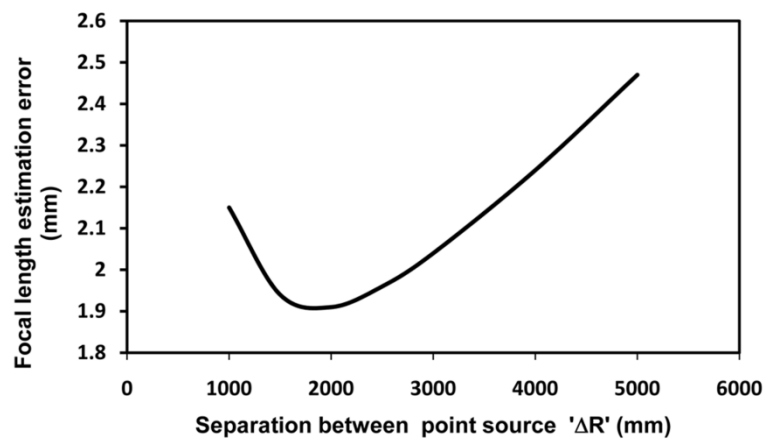


Fig. 6.15 Sensitivity of the spherical wavefront method

After positioning the CCD at the focal plane of ($z_f = 4.82$ mm) the MLA, the light spot displacement measurements are carried out for 7 different angles of plane wavefront incidence. The seven equations formed with Eq. (6.16) are solved

for the f with the least squares method. The focal length f of each microlens within the MLA for 18x18 microlens array is shown in Fig. 6.16.

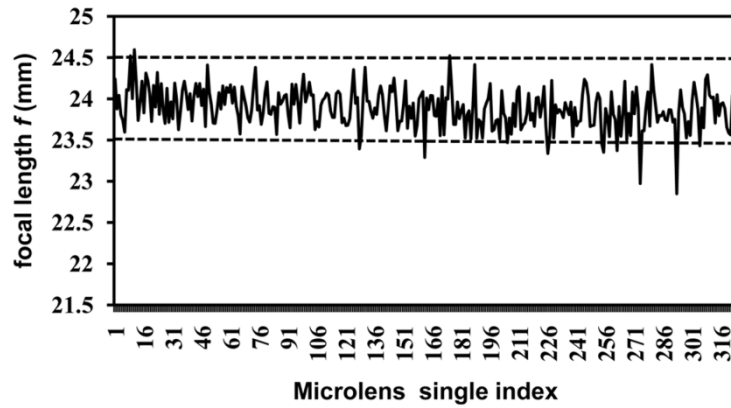


Fig. 6.16 Focal length of the each microlens

The focal length f_{MLA} of the MLA is calculated by averaging the f of all microlens and it is found to be 23.86 mm against 24 mm of the catalogue value. The focal length of the MLA corresponding to the seven different plane wavefront incident angles is shown in Fig. 6.17. In the plane wavefront method, the determination of focal length of each microlens is independent of pitch P ; hence the separation between centroids of any two adjacent microlens for the normal incident plane wavefront gives the P of the MLA (pixel size is assumed as constant).

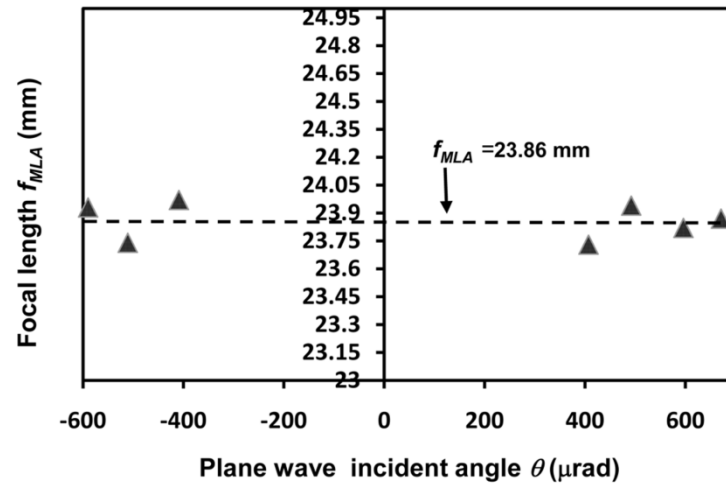


Fig. 6.17 Focal length of the MLA for various incident plane wavefront angles

The pitch of the MLA is obtained by averaging the P of all microlenses. The wavefront error (WFE) of the substrate is computed from the single pass fringe formed with the interferometer, after removing tilts and piston terms. The estimated parameters of the MLA are given in the Table 6.2. Further the same test is used to estimate the separation of microlens array with respect to the CCD in the SH WFS configuration.

Table 6.2: Measured parameters of the MLA

Microarray Lens parameters	Specification	Measured mean value (measurement error)
Pitch (μm)	328	328.3 (± 0.1)
Focal length (mm)	24	23.86 (± 0.09)
WFE PV (μm)	< 0.22	0.11* (± 0.06)

* for 12x12 mm square area,

6.5 Development of the SH WFS

An MLA and an area array detector form the SH WFS instrumentation part. The SH WFS is constructed using the MLA (AOA-0328-24-S-44x44) and the CCD (IMPERX-IPX-11M5-L). The separation of the MLA with respect to the CCD is adjusted to the f_{MLA} and quantified using the plane wavefront method and cross-verified with the spherical wavefront method; detailed in Sec 6.3 & 6.4. The photograph of the developed SH WFS is shown in Fig. 6.18. The testing of telescope in the EOM using Shack-Hartmann wavefront sensor and cross verification of it is discussed in the following sections.

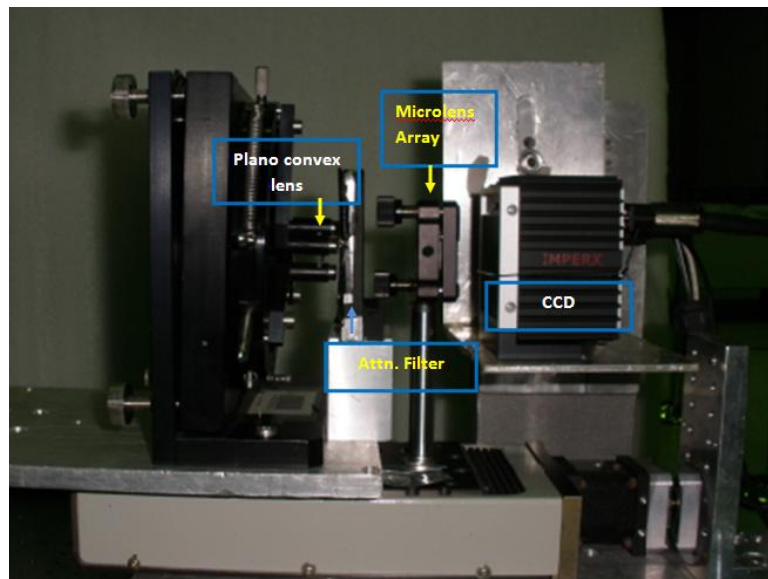
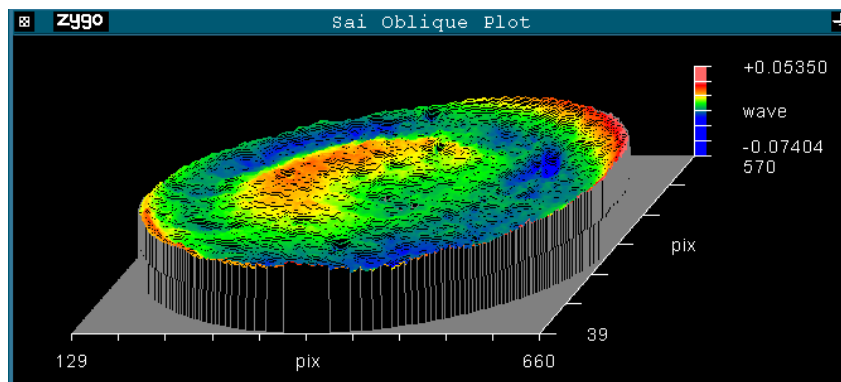
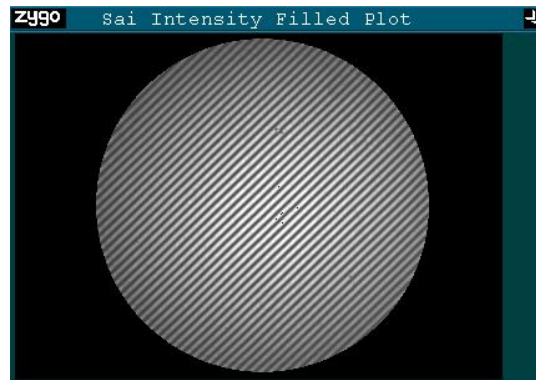


Fig. 6.18 Photograph of the developed SH WFS

6.6 Evaluation of telescope with the SH WFS

The scheme to evaluate the telescope with the SH WFS is worked out with converging optics that simulating the telescope. The SH WFS is required to evaluate the wavefront converged at the image plane of the telescope for a distant

point source. The experimental setup consists of a Zygo interferometer, a telescope, a convex lens and the SH WFS. The telescope is simulated using a 4-in f/7.1 transmission sphere of Zygo. The collimated laser beam ($\lambda = 633 \text{ nm}$) from the 4-in Zygo interferometer main frame is focused by the (transmission sphere) telescope kept in front of it. The quality of the wavefront emerges from the telescope is evaluated with interferometer in retro reflected mode and it is expressed in terms of rms and the lower-order Zernike polynomial coefficients as in fig 6.19.



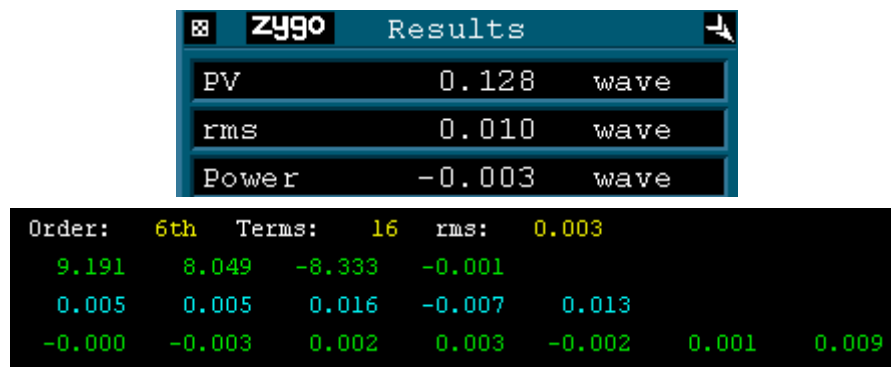


Fig. 6.19 Quality of wavefront emerging from the simulated telescope

The diverging wavefront from the focus of the telescope is collimated with a 1.5-in diameter, $f=35$ mm plano-convex lens. The plane surface of convex lens is kept facing the diverging beam to minimize the spherical aberration. The SH WFS is required to evaluate the 4.93 mm diameter collimated beam exiting from the plano-convex lens as shown in Fig. 6.20; the photograph of the test configuration is shown in Fig. 6.21.

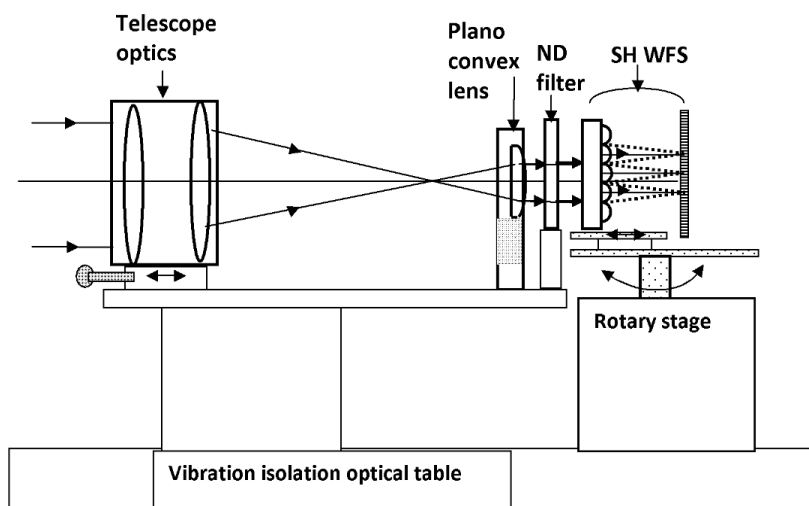


Fig. 6.20 Sketch of the SH WFS configuration for the evaluation of telescope

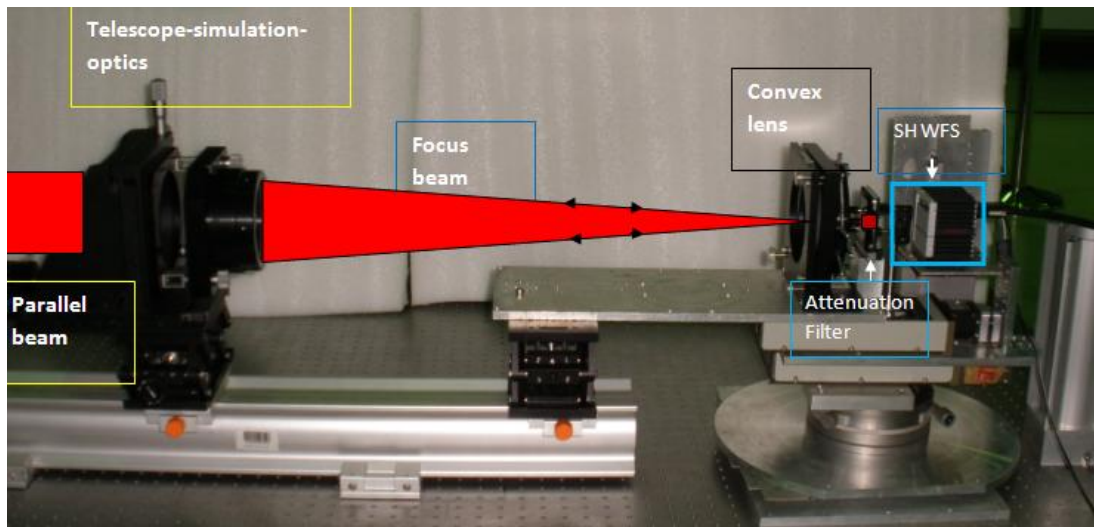


Fig. 6.21 Photograph of the SH WFS configuration for the evaluation of telescope

The alignment of test setup is carried out in the following sequential steps,

1. The SH WFS is rotated to match the retro-reflected light from the SH WFS with the align mode cross wire of the interferometer so that the SH WFS is normal to the interferometer.
2. The plano-convex lens is centered and positioned at the required distance from the SH WFS on a tip- tilt self-center mount. The lens is tilted to match the retro-reflected light from the plano surface of the lens with the align mode cross wire of the interferometer so as to make the lens normal to the interferometer.
3. The transmission sphere is mounted on a five axis mount. Initially the transmission sphere is made normal to the interferometer using the interferometer align mode cross wire. Later it is adjusted laterally so that the focus spot is centered with respect to the plano-convex lens.

4. The wavefront exiting from the plano-convex lens is evaluated with the interferometer in a retro-reflection configuration. The position of the TS is tip-tilted and decentered to reduce coma and astigmatism, also axially adjusted to minimize the focus error. The quality of the transmitted wavefront in terms of root mean square (rms) and lower order Zernike polynomial coefficients are shown Fig. 6.22.

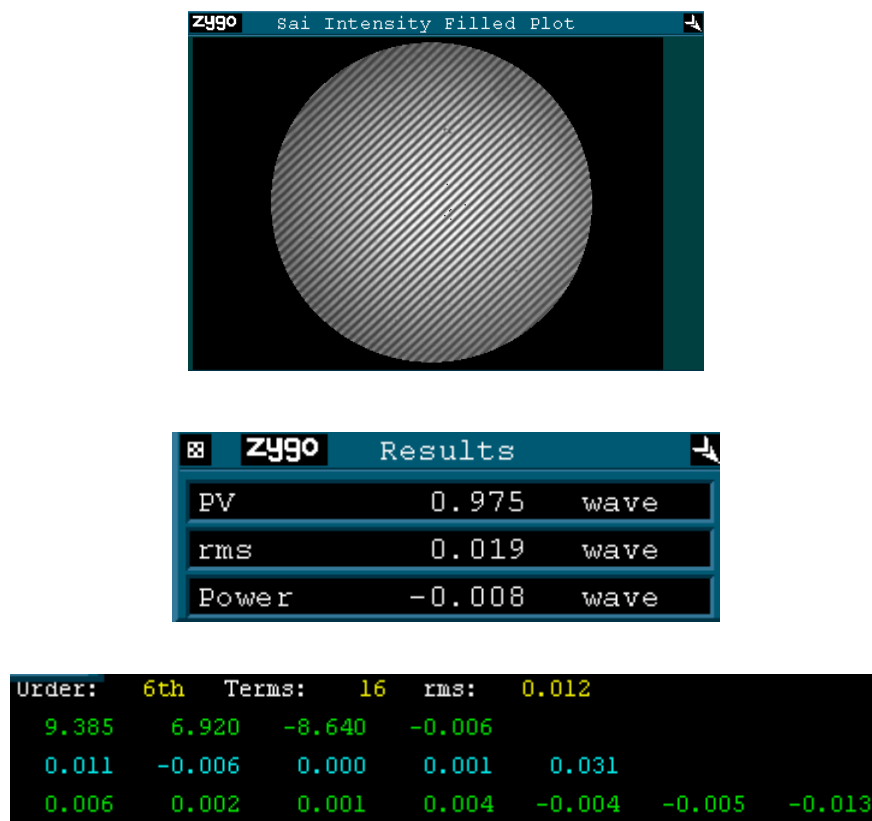


Fig.6.22 Quality of the wavefront emerging from the plano-convex lens in the test setup shown in Fig. 6.20

The SH WFS is placed in the path of collimated light, at the re-imaged pupil plane of the telescope. The focused collimated beam emerging from the plano-convex is recorded on the CCD of the SH WFS. The centroid of light spots formed in the SH WFS is given in appendix -2 and forms the reference frame. We have proposed the operation of the SH WFS for evaluating the telescope is by

carrying defocus measurements. The defocus positions are generated by axially translating the telescope (transmission sphere) with respect to the plano-convex lens and the corresponding image spot centroids are recorded. The steps followed starting from the data acquisition with the SH WFS to the generation of the wavefront are given below,

1. The light spot data are recorded for each position (defocus) of the TS for 40 times.
2. Fix a circular window, circumscribing all the light spots, equivalent to the radius of the incident collimated beam on the MLA.
3. Find the image centroid in both directions X_c and Y_c over the circular window, pixel window corresponding to the fully illuminated microlenses, for the reference and the defocused positions using the threshold limited intensity center of mass method.
4. Find displacement δ of image spot with respect to the reference frame.
5. Find the local slope (δ / f_{MLA}) at each microlens locations with mean focal length (i.e., $f_{MLA}=23.86$ the separation between the MLA and the CCD) of the MLA.
6. Reconstruct the wavefront from the slope data using modal reconstruction method. In the modal reconstruction, the slope data are fitted using the least squares method to the derivatives of 10 terms of fringe Zernike polynomial over the normalized radial coordinates of image centroid to find the modal coefficients. Then the wavefront is reconstructed over the pupil coordinate of the telescope using the Zernike polynomial.

The experiment is conducted for four defocus positions covering the required range. Since the test set up is established on a vibration isolation optical table, the experiment is also conducted for vibration isolation and non-isolation conditions. The centroid for the defocus positions # 2 of the vibration isolation and the non-isolation conditions are given in appendix-2. The reconstructed wavefront in terms of Zernike polynomial coefficients for both vibration isolation and non-isolation conditions are given in tables 6.3 and 6.4.

Table 6.3: Zernike polynomial coefficients (in λ) retrieved with the SH WFS (vibration isolation condition)

Zernike polyn. coefficients	Defocus #1 Zernike polyn.coeffts	Defocus #2 Zernike polyn.coeffts	Defocus #3 Zernike polyn.coeffts	Defocus #4 Zernike polyn.coeffts
Focus	0.117	0.239	0.357	0.469
Astigmatism $\pm 45^\circ$	0.002	0.005	0.000	-0.002
Astigmatism 0° or 90°	0.002	0.001	0.000	-0.001
Coma X	0.003	0.002	0.004	0.008
Coma Y	0.000	-0.004	0.001	-0.006
Spherical	0.005	0.005	0.005	0.009
Trefoil at X	0.000	0.000	-0.004	0.000
Trefoil at Y	-0.005	-0.000	-0.003	-0.004
Focus after correction	0.126	0.258	0.385	0.506

Table 6.4 Zernike polynomial coefficients (in λ) retrieved with the SH WFS
(vibration non- isolation condition)

Zernike polyn. coefficients	Defocus #1 Zernike polyn.coeffts	Defocus #2 Zernike polyn.coeffts	Defocus #3 Zernike polyn. coeffts	Defocus #4 Zernike polyn. coeffts
Focus	0.118	0.225	0.339	0.408
Astigmatism $\pm 45^\circ$	-0.001	-0.005	-0.0062	-0.009
Astigmatism 0° or 90°	0.005	0.008	0.009	0.012
Coma X	0.002	0.004	0.001	0.003
Coma Y	0.002	0.004	0.001	0.003
Spherical	-0.001	0.000	0.000	0.003
Trefoil at X	0.002	0.004	0.003	0.004
Trefoil at Y	-0.001	-0.002	-0.005	-0.005
Focus after correction	0.127	0.243	0.366	0.440

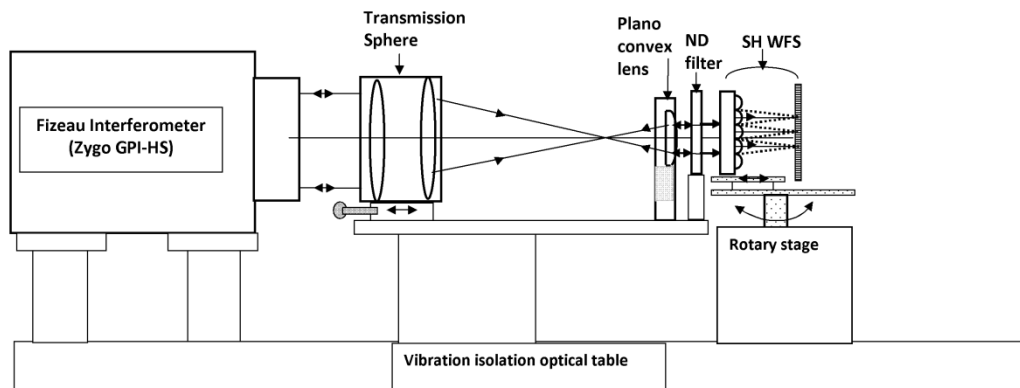


Fig. 6.23. *In situ* verification the SH WFS with a Fizeau interferometer

In order to calibrate the SH WFS, an *in situ* Fizeau interferometer measurement configuration is planned as shown in fig. 6.23. The collimated beam emerges from the plano-convex lens is retro-reflected by the surface of the neutral density filter that is kept in-front of the MLA as shown in Fig. 6.23. The measurement by the MLA and the interferometer is carried out simultaneously.

For the vibration isolation condition, the interferometer acquisition is carried out using the flash phase mode. Also, for the non-vibration isolation condition, the measurement is carried out using the flash phase mode of the Zygo interferometer. In the flash phase mode, the interferogram is recorded using a high speed single frame acquisition with a spatial carrier. The wavefront phase retrieval is carried out by Fourier fringe analysis. The Zernike polynomial coefficients obtained using interferometer (interferometer scale factor of 0.25) for both vibration isolation and non-isolation conditions are presented in tables 6.5 and 6.6.

Table 6.5: Zernike polynomial coefficients (in λ) retrieved with the interferometer (vibration isolation condition)

Zernike polyn. coefficients	Defocus #1 Zernike polyn.coefffts (λ)	Defocus #2 Zernike polyn.coefffts (λ)	Defocus #3 Zernike polyn.coefffts (λ)	Defocus #4 Zernike polyn.coefffts (λ)
Focus	0.131	0.256	0.384	0.507
Astigmatism $\pm 45^\circ$	-0.001	-0.011	0.012	0.005
Astigmatism 0° or 90°	-0.005	0.001	-0.005	0.001
Coma X	-0.003	0.000	-0.003	-0.003
Coma Y	-0.005	-0.002	0.007	0.002
Spherical	0.004	-0.003	-0.006	-0.006
Trefoil at X	0.002	0.004	0.001	0.000
Trefoil at Y	0.008	0.002	-0.007	-0.001

From tables 6.3 to 6.6 one can observe that, as expected for an axial translation of the telescope, the measurements of interferometer and that of the SH WFS show the focus error as the significant mode. It is evident from the results in tables 6.3 and 6.5 that the mean difference in the estimation of coefficients of

focus mode for the various defocus positions between the interferometer and the SH WFS measurements is 7.9%.

Table 6.6 Zernike polynomial coefficients (in λ) retrieved with the interferometer (vibration non- isolation condition)

Zernike polyn. coefficients	Defocus #1 Zernike polyn.coeffts	Defocus #2 Zernike polyn.coeffts	Defocus #3 Zernike polyn.coeffts	Defocus #4 Zernike polyn.coeffts
Focus	0.130	0.252	0.381	0.455
Astigmatism $\pm 45^\circ$	-0.006	0.002	0.004	-0.003
Astigmatism 0° or 90°	0.000	-0.006	-0.003	-0.005
Coma X	-0.004	0.005	-0.007	-0.004
Coma Y	0.003	0.009	0.001	0.001
Spherical	0.014	0.010	0.012	0.011
Trefoil at X	0.001	0.001	0.005	0.000
Trefoil at Y	-0.001	-0.001	-0.002	0.001

After applying the above correction value to the measurements of the SH WFS (shown in the last row of tables 6.3 and 6.4), the difference in the estimated magnitude of the focus modal coefficients between the two methods is < 3 nm and < 10 nm for vibration isolation and non-isolation measurements respectively.

6.7 Summary

From the design and analysis of the SH WFS, we have estimated certain parameters of the SH WFS that are to be ensured within the required tolerances. In order to estimate the parameters viz. focal length, pitch and position of MLA in the SH WFS, we have developed certain measurement techniques. We have proposed a measurement metric called image spread measure that aids in the determination of the focal plane of the MLA. We have developed experimental

methods for the determination of the focal length of the MLA using spherical wavefronts. It is found the dispersion of the estimated focal length of the MLA from multiple measurements is more with respect to the mean value. Since each focal length estimation is independent and a greater number of measurements are required to find the focal length of the MLA which is near to the true value. In view of this we have developed another method using plane wavefront generated using a phase shifting interferometer. We have shown that the focal length estimated with this method is one order of magnitude less uncertain compared to that of the spherical wavefront method. Both methods facilitates in the determination of axial position of the MLA with respect to the CCD in the SH WFS. In addition, the plane wavefront method helps in the determination of focal length of each microlens within the MLA. The knowledge of focal length of each microlens of the MLA in the SH WFS will certainly help to improve the estimation of wavefront. We have evaluated the defocus performance of a simulated optical system with the developed SH WFS. Also *in situ* verification of the SH WFS measurements is carried out with a commercial Fizeau interferometer and a close match between both methods is established after applying the correction; supporting the utility of the proposed test method for the evaluation of the optical system at EOM.

Portion of the work are published in

“Focal length measurement of microlens array for Shack-Hartmann wavefront sensor using interferometer,” *Opt. Eng.*, (2013), **52**(12): 124103.

“Determination of focal length of microlens array by spherical wavefronts,” *Opt. Eng.*, (2014) **53**(6): 064102.

“Design and development of Shack-Hartmann wavefront sensor- based testing of high resolution optical system for earth observation,” accepted for publication in *Opt. Eng.*, (2014) **53**(11):11410.

CHAPTER 7

SUMMARY AND CONCLUSION

7.1 Summary of key results

The objective of this work is to investigate the procedures and activities involved in the development of the optical system namely, design, assembly & alignment and testing that having impact on the imaging performance; devise techniques that will help to eliminate or to minimize the degradation of the imaging performance during the various development stages of the optical system; and devise a compatible method to evaluate the imaging performance of the optical system at the EOM level.

We have investigated initially the design procedures adopted for a typical high resolution optical system for earth observation. The presence of stray light, off-scene light reaching the image plane reduces the MTF of the optical system which is initially designed for a diffraction-limited MTF. It also affects the radiometric fidelity of the image. Baffles are designed and implemented to alleviate the above problem. We have investigated and identified the procedure adopted for design of baffle for direct rays of stray light and has been found in the case of Ritchey-Chretien telescope that is limited to narrow field of view or approximate or trial and error method; involving tens of thousands of rays. We have developed a new method called direct method for the design of baffle for direct rays of stray light with the real ray coordinates. The baffle parameters arrived at eliminates the direct rays of stray light reaching the image plane. However, the additional

obscuration arise due to baffles reduces the MTF. We have developed another new method called iterative method that converges to the minimum baffle obscuration and also blocks the direct rays of stray light. We have also proposed a baffle design approach for a rectangular image format optical system; a typical image format for an optical system for earth observation. We have then formulated a method to find the position of vanes that will eliminate the first order reflection arise from the inner wall of the primary mirror baffle.

After arriving at a definite procedure of baffle design for the direct rays and first order reflected rays from the primary mirror baffle, it is applied to modified RC telescope with 1 m separation between mirrors and 1.3 m total length operates at visible spectrum. The computations required for the baffle design are carried out with an optical design program ZEMAX[®]. The baffle parameters are converged to the minimum obscuration in ten iterations. The performance of baffles including vanes is evaluated with the ZEMAX[®] non-sequential mode. The baffle parameters are modelled using the NSC and the UDA of ZEMAX[®]. It is found that no direct rays of stray light as well as no significant light power after internal reflections from the inner wall of the primary mirror reach the image plane. The obscuration due to the baffle parameters are simulated in the sequential mode of ZEMAX[®] using appropriately placed user defined apertures. It is found that there is a marked improvement in the reduction of the MTF due to obscuration between low and mid spatial frequencies.

We have then investigated the techniques involved in the assembly and alignment of optical system. The mechanical stress on the optical component

during its assembly distorts the optical surface, which in turn degrades the image. The semi-kinematic type mount is used for holding the mirror and optical elements in the telescope configuration. The mount is directly bonded to the mirror with an adhesive. Many space-qualified adhesives are available and characteristics affecting the performance of optical elements are not well defined. We have investigated on the surface distortion of mirror that occurs due to space qualified adhesives at any stages of optical system development, apart from other requirements namely out-gas and lap shear strength. We have prepared samples with 3M 2216 B/A gray and Epotek 301 adhesives, and carried out experiments for surface figure evaluation, lap shear test and out-gas.

We have observed that the bonded optical assembly with Epotek 301 has shown surface deformation as concave profile upon cure and convex profile upon exposure to elevated temperature (tested at room temperature). The smaller aspect ratio bonded assembly has shown pronounced surface distortion and the surface distortion reduces for the relief bond pattern bonded assembly. A peculiar change of profile of optical surface for Epotek 301 assembly on exposure to elevated temperature has been observed that to our knowledge was not reported earlier. Also it has been noticed that the change of surface distortion profile starts occurring for the temperature near to the T_g . On the basis of this, a new method has been proposed to reduce the surface deformation occurs upon curing using the thermal exposure as against the generally adopted post-cure polishing. However, in the case of the bonded assembly with 3M 2216 B/A gray does not show any appreciable surface distortion upon curing and thermal exposure.

We have investigated further and have been found that the surface distortion phenomenon similar to Epotek 301 occurs for Hysol EA9396 adhesive. By comparing the properties of all three adhesives, we have hypothesized that the properties namely low viscous, high shore D hardness and the Tg can be used initially to identify the probable candidate among the declared space qualified adhesives for the high resolution optical systems.

We have then investigated testing of optical system in an integrated EOM. The EOM consists of CCD and other related electronics for its operation that blocks the rear of focal plane of the telescope. Due to this the conventional retro-reflected mode of interferometer test of the optical system at the electro optical module is not possible at the EOM in many cases. We explored and identified possibility of incorporating the SH WFS with the EOM as an evaluation tool.

During the development of SH WFS, we have developed an experimental method to determine the focal length of the MLA using spherical wavefront. With this method we are able to determine the position of the MLA in the SH WFS configuration. However, the dispersion of the measured focal length of MLA and hence the MLA axial position with respect to the CCD from the mean value is more. Hence a greater number of measurements are required to arrive at a value near to the true mean value. To overcome this we have developed a new method to determine the focal length of the MLA using plane wavefront with an interferometer. The measurement error of this method is 1 order of magnitude better than the spherical wavefront method. Also one can determine the focal

length of each microlens directly and also for all lenses within the MLA simultaneously using this method.

We have designed and developed a wavefront sensor tailored to meet the requirement of testing of an optical system in the electro optical module. We have then tested a simulated optical system for its defocus error with the developed SH WFS. We have also carried out in-situ verification of the results obtained with the SH WFS using a Fizeau interferometer and a close match between the measurements is established.

7.2 Future work

The baffle design method proposed here is a combination of a standard optical design package and analytical relations formulated herein. The entire procedure of baffle design method can be incorporated in a standard optical design package as a macro. Also in the baffle modelling, the vanes are considered as zero thickness and completely absorbing member. However, in reality the vanes of the baffle have finite thickness and not a perfect blackened surface. A model that can incorporate above factors may be explored in future and also the effect of finite edge of the baffle on the stray light may also be modelled and quantified. The model may also include the angular dependence of reflected light energy from the baffle surface.

The investigation carried out on the adhesive-induced stress on the optical surface revealed a peculiar phenomenon of change of surface profile for Epotek-301 assembly. The surface deformation is observed as concave profile

upon cure and convex profile upon exposure to elevated temperature near the glass transition temperature; tested at room temperature. This observation may be investigated in detail to understand the phenomena occur at polymer linkages as a new research topic.

We have developed an SH WFS based-test method for evaluating the high resolution optics. The sensor is envisaged for the testing of optical systems in the electro optical module during various tests that undergoes while on ground. It will be interesting to use the same sensor to evaluate the optical system during in-orbit operations. The results obtained during in-orbit condition certainly will open a larger domain of research activities in the very high resolution earth observation system namely, in-orbit performance evaluation, and subsequent correction either by onboard system or by post processing of image or by both.

REFERENCES

1. Ares, J and Arines, J. (2004). Influence of thresholding on centroid statistics: full analytical description, *App. Opt.* 43(31): 5796-5805.
2. Bachmann, A. G. (2001). Advances in light curing adhesive, *Proc. SPIE* 4444, pp. 185-195.
3. Bardinal, V. Daran, E. Leicle, T. Levallois, C. Camps, T. Conedera, V. Doucel, J.B and Carcenac, F. (2007). Fabrication and characterization of microlens arrays using a cantilever-based spotter, *Opt. Exp* 15 (11): 6900-6907.
4. Bely, P.Y. (2003). *The Design and Construction of large optical telescope* Springer, New York, Chapter 5, pp. 187-188.
5. Chollet, F and Ashraf, M. (2009). Simultaneous measurement of focal length and index of refraction of a microlens using a compound microscope, *J Micromechanics and Microengineering*, 19: 1-8.
6. Cawthorne, A. Purll, D and Eves, S. (2008). Very High Resolution Imaging Using Small Satellites, *6th Responsive Space Conference*, AIAA-RS6-2008-4007.
7. Chernyshov, A. Sterr, U. Riehle, F. Helmcke, J and Pfund, J. (2005), Calibration of a Shack-Hartmann sensor for absolute measurement of wavefronts, *Appl. Opt.* 44(30): 6419-6425.
8. Coleman, H.S. (1947). Stray Light in Optical Systems, *J. Opt. Soc. Am.* 37(6): 434-451.
9. Dai, G.M and Mahajan, V.N. (2008). Orthonormal polynomials in wavefront analysis: error analysis, *App. Opt.* 47(19): 3433-3445.
10. Daly, J. G and Daly, D. J. (2001). Structural adhesives for bonding optics to metals: a study of opto-mechanical stability, *Proc. SPIE* 4444, pp. 177-184.
11. Doyle, K.B. Genberg, V.L and Michels, G.J. (2002). *Integrated optomechanical analysis*, SPIE press, Washington.
12. Dyson, R. (2011). *Principles of Adaptive Optics*, 3rd ed., CRC press, New York.
13. Epps, H.W and Fabricant, D. (1997). Field corrector for wide-field CCD imaging with Ritchey-Chretien telescope, *The Astronomical Journal*, 113: 439-445.

14. Fender, J (2000). Future trend in large space optics, *Proc. SPIE* 4013, pp. 682-686.
15. Fest, E.C. (2013). *Stray light analysis and control*, 1st ed. SPIE Press, Washington.
16. Figoski, J. W. (1999). "Alignment and test results of the QuickBird Telescope using the BallOptical System Test Facility," *Proc. SPIE* 3785, pp. 99-108,
17. Fitzsimmons, J. Erickson, D and Hill, A (2008). Design and analysis of flexure mounts for precision optics, *Proc. SPIE*, pp. 7018, 7018K(1)-(8).
18. Fried, D.L. (1966). Limiting resolution looking down through the atmosphere, *J. Opt. Soc. Am.* 56(10):1380-1384.
19. Gaudin-Delrieu, C. Lamard, J. Cheroutro, P. Bailly, B. Dhuicq, P. Puig, O. (2008). The high resolution optical instruments for the Pleiades HR earth observation satellites, <http://congrexprojects.com/icso/2008-proceedings-ppts>.
20. Geary, J.M. (1995). *Introduction to wavefront sensor*, TT-18, SPIE Optical engineering press, Washington.
21. Geary, J.M. (2002). *Introduction to lens design with practical Zemax examples*, Willman Bell Inc. Virginia.
22. Geyl, R (1994). Design and fabrication of a three mirror flat field anastigmat for high resolution earth observation, *Proc. SPIE* 2210, pp. 739-746.
23. Gregory, H. S. (1998). *Practical computer-aided lens design*, Willmann-Bell Inc, Virginia, Chapter B.5, pp. 352.
24. Hales, W. L. (1992). Optimum Cassegrain baffle systems, *Appl. Opt.* 31(28): 5341-5344.
25. Harvey, J. E. (2010). Image degradation due to scattering effects in two mirror telescopes, *Opt. Eng.* 49(6): 063202(1)-(7).
26. Ho, C. and Chang, S. (2009). Baffle design for a Cassegrain telescope, *Proc. SPIE* 7506, pp. 75061S1-10.
27. Holst, G.C. (2008). Target discrimination, Chapter 20 in *Electro-optical imaging system performance*, 5th Ed., pp 413, JCD publishing, Winter park and SPIE press, Washington.

28. Jenkins, F.A. and White, H. E. (2001). Interference of two beams of light, Chapter 13 in *Fundamentals of Optics*, 4th Ed., pp. 259-282, McGraw Hill companies Inc., New York.
29. Jiang, W. Rao, X. Yang, Z and Ling, N. (2005). Applications of Hartmann Shack wavefront sensors, *Proc. SPIE* 6018, pp. 60180N (1)-(9).
30. Joseph, G. (2003). *Fundamental of remote sensing*, 1st ed., University Press, Hyderabad.
31. Joseph, G. (1996). Imaging sensors for remote sensing, *Remote sen. rev* 13(3): 257-342.
32. Jung, H. Jung, D and Lee, S. (2005). Optical design for multispectral camera (MSC) for high resolution earth observation, *Proc. SPIE*, 6024, pp 602404.
33. Kasturirangan, K. (2004). Science and technology of imaging from space, *Current science*, 87(5): 584-601.
34. Kihm, H. and Lee, Y. (2010). Optimization and tolerance Scheme for a mirror mount design based on optomechanical performance, *J. Korean Phy Soc.* 51(3): 440-445
35. Kingslake, R. and BarryJohnson, R. (2010). *Lens Design Fundamentals*, Elsevier.
36. Korsch D (1980). Design and optimization technique for three mirror telescopes, *Appl. Opt.* 19(21): 3640-3545.
37. Kramer, H.J. (2002). *Observation of the Earth and its Environment*, 4th ed. Springer-Verlag, Berlin Heidelberg, Germany.
38. Laikin, M. (2006) *Lens Design*, 4th ed. CRC press, Taylor and Francis, Baco Raton.
39. Lamard, J. Gaudin-Delrieu, C. Valentini, D. Renard, C. Tournier, T and Laherrere, J. (2004). Design of the high resolution optical instrument for the PLEIADES HR earth observation satellite, *Proc. ICSO*, pp. 149-156.
40. Lane, R.G and Tallon, M. (1992). Wavefront reconstruction using Shack-Hartmann wavefront sensor, *App. Opt.* 31(32): 6902.
41. Lakshminarayanan, V. and Fleck. (2011). Zernike polynomial: a guide, *J Mod. Opt*, 58: 545-561.
42. Mahajan, V.N. (1981). Zernike annular polynomial for imaging systems with annular pupils, *J. Opt. Soc. Am.* 71(1): 75-85.

43. Mahajan, V.N. (2013). Optical imaging and aberrations (Part-III) Wavefront analysis, Chapter 14, *SPIE Press*, Washington.
44. Malacara, D. (1992). *Optical Shop Testing*, 2nd ed. John-Wiley Inc., New Jersey.
45. Malacara, D and Malacara, Z. (2004). *Handbook of Lens Design*, Marcel Dekker Inc, Chapter 14.
46. Malacara, D. and Malacara, Z. (1992). Testing and centering of lenses by means of a Hartmann test with four holes, *Opt. Eng.* 31(7): 1551-1555.
47. *Metropro reference guide*-OMP-0347J, (2004). Zygo Corporation, USA. (www.Zygo.com).
48. Michaelis, H. Grothues, H.C. Behnke, T. Hirsch, T. Ress, E and Sebastian, I. (1998). New concepts for high resolution imagers for earth observation and planetary exploration, *Proc.32nd Symp. Remote sensing methodology for earth observation and planetary exploration*, Netherlands.
49. NASA report on Selection of spacecraft materials and supporting vacuum outgassing data -*Practice no PT-TE-1410*
<http://www.nasa.gov/offices/oce/lis/0778.html>
50. Neal, D. R. Coupland, J. and Neal, D, (2002). Shack-Hartmann Wavefront sensor precision and accuracy, *Proc. SPIE* 477, pp. 148-160.
51. Neal D. R. Armstrong , D. J. and Turner W. T. (1998). Characterization of Infrared Laser systems, *Proc. SPIE*, 3437, pp. 360-370.
52. Ohl, R. G. Barkhouser, R.H. Kennedy, M. J and Friedman, S.D, *Assembly and test-induced distortions of FUSE mirrors- lessons learned*, <http://fuse.pha.jhu.edu>.
53. Pateric cote and Nichola Desnoyers. (2011). Thermal stress failure criteria for a structural epoxy, *Proc. SPIE* 8125, pp. 8125 (K1)-(K12).
54. Platt, B. and Shack, R. (2001). History and principles of Shack-Hartmann wavefront sensing, *J. Refract Surg.* 17: 573-577.
55. Pfund, J. Lindlein, N and Schwider, J. (1998). Misalignment effects of the Shack-Hartmann sensor, *Appl.Opt.* 37(1), 22-27.
56. Prescott, R. (1968). Cassegrainian Baffle Design, *Appl. Opt.* 7(3): 479–481.

57. Reichelt, S. and Zappe, H. (2005). Combined Twyman-Green and Mach-Zehnder interferometer for microlens testing, *Appl. Opt.* 44(27): 5786-5792.
58. Roddier, F. (1988). Curvature sensing and compensation: a new concept in adaptive optics, *Appl. Opt.* 27(7): 1223 – 1225.
59. SAC. (1994). *Critical Design Review- Indian Remote Sensing Satellite (IRS)-1C PAN camera*, SAC-IRS- 1C/1D-1-11- 1994.
60. Saxena, A.K. and Jayarajan, A.P. (1980). Testing concave aspheric surfaces: Use of two crossed Babinet Compensators, *Appl. Opt.* 20 (5): 724.
61. Schreiber, H. and Bruning, J.H. (2007). Phase shifting interferometer, Chap. 14 in *Optical Shop Testing*, 3rd ed., D Malacara, Eds., pp. 547-655, John-Wiley Inc., New Jersey.
62. Shannon, R.R. (1997). *The art and science of Optical Design*, Cambridge University Press.
63. Senthil Kumar, M and Shanker, ASL. (2001). Realization of Optical system for IRS-TES payload, *Seminar on Frontiers in Optics*, Laboratory for Electro Optic Sensors (LEOS), ISRO, Bangalore.
64. Seo, Y. D. Kim, F. J and Youn, S (2007). A Study on the adhesive effects on the optical performance of the primary system of the camera, *J. Korean Phy. Soc.* 51(6): 1901-1908.
65. Simonetti, F. Romoli, A and Mazzinghi, P. (2006). Reflecting telescopes for an orbiting high-resolution camera for earth observation, *Opt. Eng.* 45(5): 05300.
66. Slater, P.N. (1980). *Remote Sensing: Optics and Optical Systems*, Addison-Wesley publishing company, Massachusetts, USA.
67. Smith, G. H. (1998). *Practical computer-aided lens design* Willmann-Bell Inc, Virginia, Chapter B.5, pp. 352.
68. Smith W J. (1992). *Modern Lens Design-A resource Manual*, McGraw-Hill Inc, New york.
69. Smith, W.J. (2000). *Modern Optical Engineering*, 3rd ed. McGraw Hill publications, New york.
70. Song, N. Zongmin, Y and Fengyao, H. (2002). Baffles design of an axial two-mirror telescope, *Opt. Eng.* 41(9), 2353-2356.

71. Southwell, W.H. (1980). Wavefront estimation from wavefront slope measurements, *J. Opt. Soc. Am* 70 (8): 998-1006.
72. Stahl, P. (2011). Rules for Optical Metrology, *International Commission for Optics 22nd General Congress*, Mexico.
73. Treibitz, T. and Schechner, Y.Y. (2012). Resolution loss without imaging blur, *J. Opt. Soc. Am. A*, 29: 1516-1528.
74. Technical Data sheets of *Epotek-301*. (1/1994). Epoxy technology Inc. USA Rev:1.
75. Technical Data sheets of *Hysol EA 9396*. (2002). Henkel Corp. USA Rev:6.
76. Technical Data sheets of *3M 2216 Gray*. (2010). 3M Scotch Weld USA.
77. Thomas, S. Fusco, T. Tokovinin, A. Nicolle, M. Michau, V and Rousset, G. (2006). Comparison of centroid computation algorithms in a Shack–Hartmann sensor, *Mon. Not. R. Astron. Soc.* 371: 323–336.
78. Vreugd , J. Voert, M.J.A. Nijenhuis, J. R. Pijnenburg, J.A.C.M and Tabak, E. (2012). An improved stress prediction in adhesive bonded optical components, *Proc. SPIE* 8450, pp. 8450A(1)- 10).
79. West, S.C. Burge, J.H. Yound, R.S. Anderson, D.S. Murgluc, C and Ketelsen, D. A. (1992). Optical metrology for two large highly aspheric telescope mirrors, *App. Opt.* 31(34): 7191-7197.
80. J. J. Widiker, S.R. Harris, and B.D. Duncan. (2006). “High-speed Shack–Hartmann wavefront sensor design with commercial off-the-shelf optics,” *Appl. Opt.*, 45(2): 383-395.
81. William, D.R. (1993). *The Infrared and Electro-Optical systems Handbook*, SPIE Optical Engineering Press, Washington, Vol: 4, Chapter-3.
82. Wilson, R.N. (2007). *Reflecting telescope optics- I*, 2nd ed. Springer, Germany.
83. Wimperis, J.R. and Johnston, S.F. (1984). Optical cements for interferometric applications. *Appl. Opt.*, 23 (8):1145-1147.
84. Wyant, J.C. (1987). Interferometric testing of aspheric surfaces, *Proc SPIE*, 816, pp. 19-39.

85. Yang J. Wei, L. Chen, Hongli. Rao, X and Rao, C. (2010). Absolute calibration of Hartmann-Shack wavefront sensor by spherical wavefronts, *Opt. Commun.* 283(6): 910-916.
86. Yoder P.R (2006a). *Opto-mechanical systems design*, 3rd ed. CRC Press, Taylor & Francis, Boca Raton.
87. Yoder P.R (2006b). *Mounting of optics in optical instruments*, 2nd ed. SPIE Press, Washington.
88. Yoon, G. Y. Jitsuna, T. Nakatsuka, M and Nakai, S, (1996). Shack Hartmann wavefront measurement with a large F-number plastic microlens array, *Appl. Opt.* 35(1): 188-192.
89. Young, A.T. (1967). Design of Cassegrain light shields, *Appl. Opt.* 6 (6): 1063-1067.
90. ZEMAX[®] *optical design program* User's Guide. (2009). Focus Software Incorporated, USA.
91. Zhu, X. Wu, F. Cao, X. Wu, S. Zhang, P, Jing, H. (2012). "Focal length measurement of Microlens-array by the clarity function of digital image," *Proc. SPIE* 8417, pp. 84171E (1)-(9).

APPENDIX- 1

1. Primary mirror baffle is constructed with the following objects and aperture.

a. Cylindrical tube with 1 mm thickness positioning 30 mm in front the first surface of the field corrector optics (FCO).

b. there are fourteen plate like structures make the vanes of the primary mirror baffle positioned along the length of the cylindrical tube of the baffle.

a. Cylindrical tube

It is constructed using object type “Cone” placed at 516.15 mm with respect to secondary mirror vertex; towards primary mirror. The radius at both ends is kept same 82.58 mm and length is 608.86 mm. The cylindrical baffle object is shown Fig. A1.

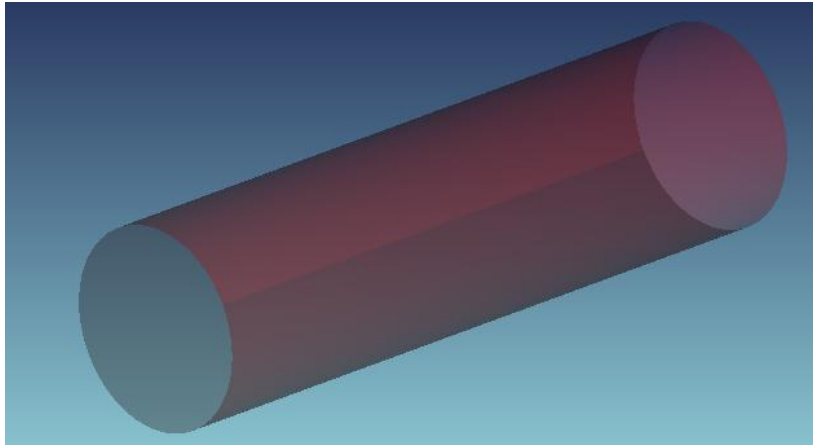


Fig. A1 baffle cylindrical structure

b. Vane structures

1. The first vane (shown in A2) forms the front end of the primary mirror baffle placed at -453.86 mm with respect to the primary mirror vertex (negative sign indicates object is left of the primary mirror). It is constructed using the user defined aperture (UDA). It is made in two UDA files forming left and right half of the vane structure. Due to the linear segmentation of arc by straight lines, small

gap is formed between the cylindrical tube inner circle and the arc of the vane structure. To block the gap an annulus NSC object is placed with inner radius of 82.55 mm and outer radius of 82.58 mm.

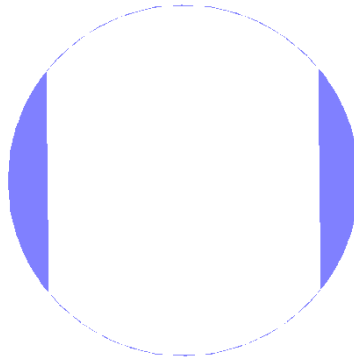
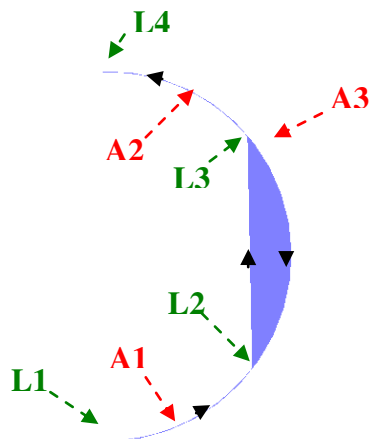


Fig. A2 first vane structure

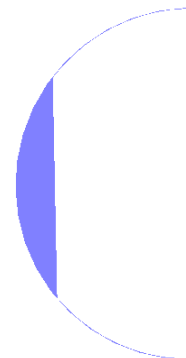
Vane :1 UDA file for right part of the vane

```
lin 0 -82.55          L1
arc 0 0 -51.095 10    A1
lin 64.24 -51.84      L2
lin 64.24 51.84       L3
arc 0 0 -51.10 10     A2
lin 0 82.55           L4
arc 0 0 180 30        A3
brk
```



Vane :1 UDA file for left part of the vane

```
lin 0 -82.55
arc 0 0 51.095 10
lin -64.24 -51.84
```



```

lin -64.24 51.84
arc 0 0 51.095 10
lin 0 82.55
arc 0 0 -180 20
brk

```

2. The second vane (shown in A3) is placed at 6.5 mm with respect to the first vane of the primary mirror baffle. To block the gap an annulus NSC object is placed with inner radius of 82.35 mm and outer radius of 82.58 mm.

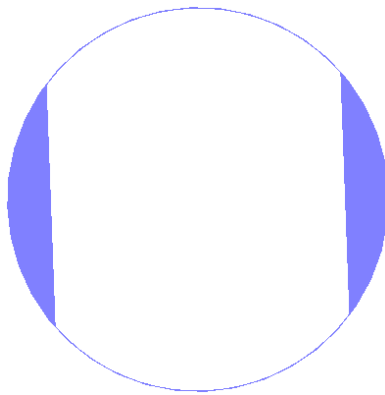


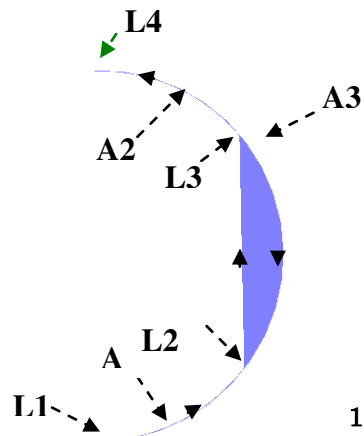
Fig. A3 Second vane structure

Vane :2 UDA file for right part of the vane

```

lin 0 -82.35          L1
arc 0 0 -50.90 10     A1
lin 63.891 -51.92     L2
lin 63.891 51.92      L3
arc 0 0 -50.90 10     A2
lin 0 -82.35          L4
arc 0 0 180 30        A3
brk

```



Vane :2 UDA file for left part of the vane

```
lin 0 -82.35
arc 0 0 50.90 10
lin -63.89 -51.92
lin -63.89 51.92
arc 0 0 50.90 10
lin 0 82.35
arc 0 0 -180 20
brk
```



3. The third vane (shown in A4) is placed at 10.1 mm with respect to the second vane of the primary mirror baffle. To block the gap an annulus NSC object is placed with inner radius of 82.03 mm and outer radius of 82.58 mm.

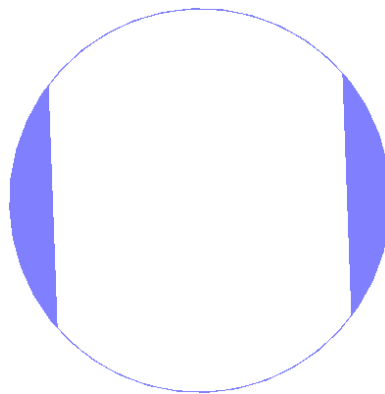


Fig. A4 Third vane structure

Vane :3 UDA file for right part of the vane

```
lin 0 -82.03
arc 0 0 -50.57 10
lin 63.36 -52.1
lin 63.36 52.1
arc 0 0 -50.57 10
lin 0 82.03
arc 0 0 180 30
brk
```

Vane :3 UDA file for left part of the vane

```
lin 0 -82.03
arc 0 0 50.57 10
lin -63.36 -52.1
```



```

lin -63.36 52.1
arc 0 0 50.57 10
lin 0 82.03
arc 0 0 -180 30
brk

```

4. The fourth vane (shown in A5) is placed at 14.4 mm with respect to the third vane of the primary mirror baffle. To block the gap an annulus NSC object is placed with inner radius of 65.9 mm and outer radius of 82.58 mm.

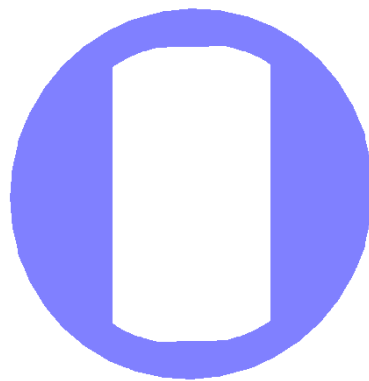


Fig. A5 Fourth vane structure

Vane : 4 UDA file for right part of the vane

```

lin 0 -82.55
lin 0 -65.9
lin 15.35 -65.95
arc 0 0 -18.79 10
lin 35.77 -57.49
lin 35.77 57.49
arc 0 0 -18.79 10
lin 0 65.95
lin 0 82.55
arc 0 0 180 30
brk

```



Vane : 4 UDA file for left part of the vane

```

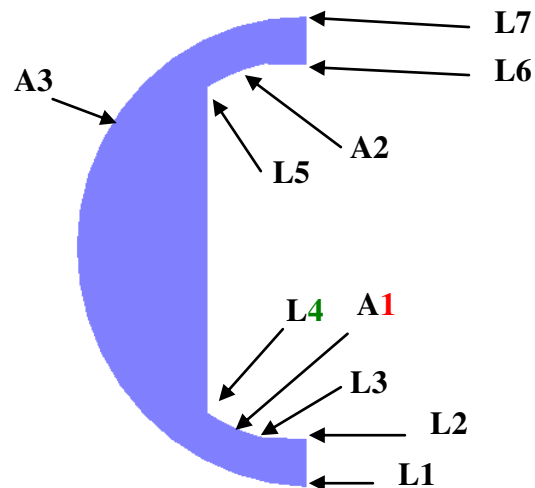
lin 0 -82.55          L1
lin 0 -65.945        L2

```

```

lin -15.35 -65.945      L3
arc 0 0 18.79 10       A1
lin -35.77 -57.49      L4
lin -35.77 57.49       L5
arc 0 0 18.79 10       A2
lin 0 65.945           L6
lin 0 82.55            L7
arc 0 0 -180 30        A3
brk

```



5. The fifth vane is placed at 20.2 mm with respect to the fourth vane of the primary mirror baffle.

Vane : 5 UDA file for right part of the vane

```

lin 0 -82.55
lin 0 -80.97
lin -3.077 -80.97
arc 0 0 47.22 10
lin 61.53 -52.72
lin 61.53 52.72
arc 0 0 47.22 10
lin 0 80.97
lin 0 82.55
arc 0 0 -180 30
brk

```

Vane : 5 UDA file for left part of the vane

```

lin 0 -82.55
lin 0 -80.97

```

```

lin -3.077 -80.97
arc 0 0 47.22 10
lin -61.53 -52.72
lin -61.53 52.72
arc 0 0 47.22 10
lin 0 80.97
lin 0 82.55
arc 0 0 -180 30
brk

```

6. The sixth vane is placed at 27.8 mm with respect to the fifth vane of the primary mirror baffle.

Vane : 6 UDA file for right part of the vane

```

lin 0 -82.55
lin 0 -63.22
lin 21.37 -63.22
arc 21.37 -33.27 -90 25
lin 51.33 33.27
arc 21.37 33.27 -90 25
lin 0 63.22
lin 0 82.55
arc 0 0 180 30
brk

```

Vane : 6 UDA file for left part of the vane

```

lin 0 -82.55
lin 0 -63.22
lin -21.37 -63.22
arc -21.37 -33.27 -90 25
lin -51.33 33.27
arc -21.37 33.27 -90 25
lin 0 63.22
lin 0 82.55
arc 0 0 -180 30
brk

```

7. The seventh vane is placed at 37.3 mm with respect to the sixth vane of the primary mirror baffle.

Vane : 7 UDA file for right part of the vane

```

lin 0 -82.55
lin 0 -62.185

```

```

lin 19.78 -62.19
arc 19.78 -32.21 -90 25
lin 49.77 32.21
arc 19.78 32.21 -90 25
lin 0 62.19
lin 0 82.55
arc 0 0 180 25
brk
Vane : 7 UDA file for left part of the vane

```

```

lin 0 -82.55
lin 0 -62.19
lin -19.775 -62.19
arc -19.78 -32.21 -90 25
lin -49.77 32.21
arc -19.78 32.21 -90 25
lin 0 62.19
lin 0 82.55
arc 0 0 -180 25
brk

```

8. The eighth vane is placed at 48.5 mm with respect to the seventh vane of the primary mirror baffle.

Vane : 8 UDA file for right part of the vane

```

lin 0 -82.55
lin 0 -61.13
lin 18.24 -61.13
arc 18.24 -31.18 -90 25
lin 48.21 31.18
arc 18.24 31.18 -90 25
lin 0 61.13
lin 0 82.55
arc 0 0 180 25
brk

```

Vane : 8 UDA file for left part of the vane

```

lin 0 -82.55
lin 0 -61.13
lin -18.24 -61.13
arc -18.24 -31.18 -90 25
lin -48.21 31.18

```

```

arc -18.24 31.18 -90 25
lin 0 61.13
lin 0 82.55
arc 0 0 -180 25
brk

```

9. The ninth vane is placed at 60.4 mm with respect to the eighth vane of the primary mirror baffle.

Vane : 9 UDA file for right part of the vane

```

lin 0 -82.55
lin 0 -60.085
lin 21.64 -60.085
arc 21.64 -35.11 -90 25
lin 46.63 35.11
arc 21.64 35.11 -90 25
lin 0 60.85
lin 0 82.55
arc 0 0 180 25
brk

```

Vane : 9 UDA file for left part of the vane

```

lin 0 -82.55
lin 0 -60.09
lin -21.64 -60.09
arc -21.64 -35.11 -90 25
lin -46.63 35.11
arc -21.64 35.11 -90 25
lin 0 60.85
lin 0 82.55
arc 0 0 -180 25
brk

```

10. The tenth vane is placed at 71.4 mm with respect to the ninth vane of the primary mirror baffle.

Vane : 10 UDA file for right part of the vane

```

lin 0 -82.55
lin 0 -59.04
lin 20.02 -59.04
arc 20.02 -34 -90 25
lin 45.06 34

```

```

arc 20.02 34 -90 25
lin 0 59.04
lin 0 82.55
arc 0 0 180 25
brk

```

Vane : 10 UDA file for left part of the vane

```

lin 0 -82.55
lin 0 -59.04
lin -20.02 -59.04
arc -20.02 -34 -90 25
lin -45.06 34
arc -20.02 34 -90 25
lin 0 59.04
lin 0 82.55
arc 0 0 -180 30
brk

```

11. The eleventh vane is placed at 79.3 mm with respect to the tenth vane of the primary mirror baffle.

Vane : 11 UDA file for right part of the vane

```

lin 0 -82.55
lin 0 -70.93
lin 11.96 -70.93
arc 0 0 28.46 10
lin 44.32 -56.66
lin 44.32 56.66
arc 0 0 28.46 10
lin 0 70.93
lin 0 82.55
arc 0 0 180 30
brk

```

Vane : 11 UDA file for left part of the vane

```

lin 0 -82.55
lin 0 -70.93
lin -11.96 -70.93
arc 0 0 28.46 10
lin -44.32 -56.66
lin -44.32 56.66
arc 0 0 28.46 10
lin 0 70.93
lin 0 82.55

```

arc 0 0 -180 30
brk

12. The twelfth vane is placed at 82.2 mm with respect to the eleventh vane of the primary mirror baffle.

Vane : 12 UDA file for right part of the vane

lin 0 -82.55
lin 0 -68.40
lin 13.71 -68.40
arc 0 0 23.62 10
lin 39.97 -57.17
lin 39.97 57.17
arc 0 0 23.62 10
lin 0 68.40
lin 0 82.55
arc 0 0 180 30
brk

Vane : 12 UDA file for left part of the vane

lin 0 -82.55
lin 0 -68.40
lin -13.71 -68.40
arc 0 0 23.62 10
lin -39.97 -57.17
lin -39.97 57.17
arc 0 0 23.62 10
lin 0 68.40
lin 0 82.55
arc 0 0 -180 30
brk

13. The thirteenth vane is placed at 79.3 mm with respect to the twelfth vane of the primary mirror baffle.

Vane : 13 UDA file for right part of the vane

lin 0 -82.55
lin 0 -65.95
lin 15.35 -65.95
arc 0 0 -18.79 10
lin 35.77 -57.49
lin 35.77 57.49
arc 0 0 -18.79 10

lin 0 65.95
lin 0 82.55
arc 0 0 180 30
brk

Vane : 13 UDA file for left part of the vane

lin 0 -82.55
lin 0 -65.95
lin -15.35 -65.95
arc 0 0 -18.79 10
lin -35.77 -57.49
lin -35.77 57.49
arc 0 0 -18.79 10
lin 0 65.95
lin 0 82.55
arc 0 0 -180 30
brk

14. The fourteenth vane is placed at 71.4 mm with respect to the thirteenth vane of the primary mirror baffle. This vane forms the back of the primary mirror baffle.

Vane : 14 UDA file for right part of the vane

lin 0 -82.55
lin 0 -63.74
lin 16.786 -63.74
arc 0 0 -14.27 10
lin 31.99 -57.63
lin 31.99 57.63
arc 0 0 -14.27 10
lin 0 63.74
lin 0 82.55
arc 0 0 180 30
brk

Vane : 14 UDA file for left part of the vane

lin 0 -82.55
lin 0 -63.74
lin -16.79 -63.74
arc 0 0 -14.27 10
lin -31.99 -57.63
lin -31.99 57.63
arc 0 0 -14.27 10
lin 0 63.738
lin 0 82.55


```
arc 0 0 180 30
brk
```

2. Secondary mirror baffle is constructed with the following objects and aperture.

- i. Back annular plate structure
- ii. Side rectangular projection
- iii. Curved corners

i. Back annular plate structure is shown in Fig. A6. This structure is constructed using the UDA files.

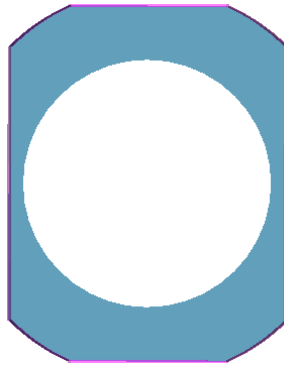


Fig. A6 Back plate of secondary mirror baffle

The UDA for the right side

```
lin 0 -143.146
lin 0 -99.5
arc 0 0 -180 30
lin 0 143.146
lin 63.46 143.146
arc 0 0 21.3072 5
lin 111.1375 -110.302
arc 0 0 21.3072 5
brk
```



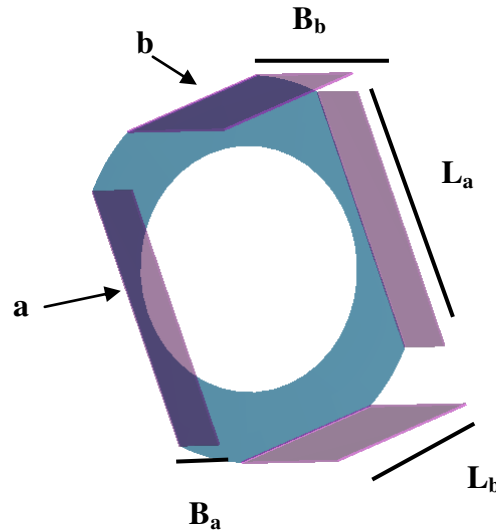
The UDA for the left side

```
lin 0 -143.146
lin 0 -99.5
arc 0 0 180 20
lin 0 143.146
lin -63.46 143.146
arc 0 0 -21.307 20
lin -111.138 -110.307
arc 0 0 -21.307 20
brk
```



ii. Rectangular projections are made by NSC object “**Rectangular volume**”.

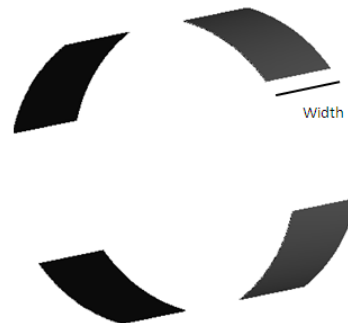
(a) Two rectangular volume objects are used with breadth (B_a) 66.2 mm, length (L_a) 220.6 mm and thickness of 1 mm. (b) Two rectangular volume objects are used with breadth (B_b) 162.8 mm, length (L_b) 126.9 mm and thickness of 1 mm. (shown below)



iii. The curved corners are constructed using “**Rectangular Torus Surface**” of NSC objects. The rectangular torus surface is defined by 5 parameters viz. inner radius, outer radius, thickness, start angle and stop angle. Since this object is drawn in YZ plane, it has to 90 rotated to make it XY plane. Inner radius defines the required curvature of the corner and outer radius gives the thickness of the baffle plate. The thickness defines the length along optic axis. The start & stop angle defines length of arc of curved corner and also defines the angular position in XY plane. The view of baffle corners and also schematic of curved corner are shown below.



Baffle corners



Schematic of curved corners

APPENDIX-2

1. Centroids of image spot recording along x and y directions at focus with vibration isolation

Centroid along x -axis

	90.49658	125.3455	160.6941	196.6451	232.9255	269.1714	305.4685	341.7588	377.2494		
54.19382	88.98555	124.3997	160.2749	196.1918	232.6795	269.1001	305.4842	341.844	378.0798	413.5626	
53.21868	88.04552	123.5379	159.4419	195.7071	232.7398	269.1338	305.7558	342.2273	378.2285	414.3402	449.0964
52.10349	87.23927	122.7794	158.9536	195.6047	232.4386	269.267	305.9653	342.6016	378.7034	414.5157	450.1057
51.43532	86.53027	122.0477	158.4209	195.3125	232.2294	269.245	306.1211	342.7778	379.0599	414.6969	450.4696
50.69957	86.04177	121.4589	157.9644	194.7307	231.9079	269.3201	306.2679	342.7199	378.9662	415.1102	450.5234
50.73344	85.65166	121.3412	157.5106	194.8453	231.853	268.8109	306.2123	343.0361	378.9547	415.0046	450.3996
50.68179	85.7155	121.4244	157.6732	194.6903	231.8952	268.9148	306.0084	342.4277	378.8268	414.6525	450.1991
51.00712	86.21074	121.8677	157.7667	194.6174	231.7518	268.7812	305.7147	342.0988	378.3765	414.0839	449.5749
51.90035	86.52941	122.1749	158.0482	194.8328	231.7321	268.3869	305.2754	341.4379	377.6052	413.3475	449.0515
52.7882	87.36856	122.674	158.7	195.14	231.6927	268.0705	304.752	340.9077	376.9147	412.6098	447.9907
	88.39778	123.336	159.0038	195.093	231.4995	267.8269	304.1969	340.2565	376.1797	411.6435	

Centroid along y –axis

	19.41354	18.29781	17.93784	17.58461	17.55353	17.50741	17.72563	18.1823	18.90265		
55.03307	54.12826	53.52066	52.9965	52.43756	52.57997	52.52546	53.11167	53.46429	53.96831	54.66281	
90.19923	89.41801	88.87314	88.23092	88.12029	88.07098	88.08417	88.57146	88.99284	89.83194	90.31079	91.04994
125.823	125.0657	124.6697	124.1463	123.9126	123.9091	124.3254	124.8353	124.9127	125.3587	126.1305	126.6144
161.558	161.3494	161.1024	160.6517	160.356	160.3043	160.5884	161.1357	161.3184	161.9041	162.1169	162.6648
197.6217	197.4501	197.5781	197.5506	197.4605	197.5931	197.7273	197.7417	198.0612	198.4363	198.7317	199.0799
233.8946	234.1003	234.2912	234.6915	234.4379	234.7736	234.9669	234.7908	235.1339	235.0548	235.1448	235.1482
269.9022	270.4807	271.3165	271.4947	271.7513	271.6915	271.8274	272.1376	271.7879	271.9429	271.6497	271.3681
306.0543	306.9654	307.5984	308.3652	308.6644	308.9204	309.0794	308.6436	308.7083	308.4685	308.0587	307.5848
342.1324	343.0025	343.5522	344.4374	344.6962	345.1653	345.4425	345.4761	344.7005	344.5158	344.0057	343.5244
377.0542	378.4149	379.4207	380.1247	380.9341	381.1989	380.9169	381.0417	380.8254	380.3509	380.0679	379.1474
	413.42	414.5868	415.33	416.1356	416.2965	416.5766	416.4863	415.9876	415.8425	415.0827	

2. Centroids of image spot recording along x and y directions for defocus position #2 with vibration isolation.

Centroid along x -axis

	89.86379	124.7972	160.4619	196.6689	233.1377	269.5786	306.1844	342.5854	378.3132		
53.44662	88.21086	123.9293	160.0622	196.232	232.9233	269.5343	306.1675	342.77	379.1506	414.9151	
52.23524	87.42903	123.0968	159.2541	195.7733	232.9498	269.6331	306.4231	343.0682	379.2938	415.6165	450.6884
51.19059	86.54825	122.3829	158.7413	195.6617	232.6783	269.7038	306.5778	343.4245	379.8792	415.835	451.6062
50.57233	85.8428	121.6006	158.1671	195.3304	232.4468	269.6418	306.8017	343.5847	380.1695	415.9754	452.0142
49.82713	85.44215	120.9509	157.771	194.7298	232.1323	269.6719	306.8628	343.5944	379.9822	416.3865	452.1631
49.91357	85.04363	120.8527	157.2153	194.8192	232.0761	269.3047	306.7889	343.8278	379.9413	416.1609	451.722
49.75649	85.07213	121.0179	157.484	194.6867	232.1703	269.4001	306.6509	343.2136	379.7912	415.9114	451.7358
50.12455	85.53452	121.5156	157.5891	194.6654	231.9781	269.2382	306.391	342.9078	379.4046	415.2682	451.1077
51.03052	85.81292	121.6838	157.804	194.8165	231.9499	268.7372	305.8528	342.3133	378.6743	414.6084	450.5945
51.79129	86.67275	122.2068	158.5585	195.1395	231.891	268.5415	305.3894	341.7182	377.9619	413.9082	449.5203
	87.67535	122.868	158.7842	195.1221	231.7009	268.3046	304.8158	341.1099	377.2741	413.0253	

Centroid along y –axis

	18.07998	16.85214	16.43961	16.13532	16.19856	16.04452	16.22258	16.76419	17.48119		
54.03991	52.89557	52.24491	51.73875	51.26639	51.37677	51.349	51.96935	52.26988	52.75583	53.50689	
89.04896	88.42686	87.79895	87.30269	87.17414	87.09778	87.18118	87.586	88.04445	88.85693	89.3834	90.06398
125.0034	124.3372	123.8619	123.4053	123.2942	123.2082	123.6259	124.0818	124.1581	124.6277	125.333	125.7698
161.0345	160.7008	160.5165	160.1156	159.7434	159.7409	160.1233	160.6361	160.7854	161.2297	161.5918	162.1166
197.2991	197.1163	197.2544	197.2775	197.1805	197.3407	197.4536	197.4479	197.6835	198.0337	198.3501	198.8326
233.7978	233.9559	234.1707	234.5626	234.3636	234.6866	234.8289	234.6646	234.9735	234.9155	235.0969	235.0868
270.0301	270.5801	271.4259	271.5843	271.811	271.7612	271.8999	272.2244	271.8282	271.9789	271.8142	271.452
306.4464	307.3322	307.9701	308.6135	308.9948	309.2368	309.3881	308.8786	308.9906	308.7333	308.2851	307.9781
342.6855	343.539	344.1219	344.92	345.272	345.6343	345.8971	345.9125	345.2465	345.0535	344.5071	344.1282
377.8614	379.2296	380.2425	380.8262	381.7018	381.7986	381.6197	381.7288	381.519	381.0699	380.8879	379.9012
	414.4947	415.5707	416.3003	417.118	417.2936	417.5522	417.4179	416.9119	416.8273	416.0915	

3. Centroids of image spot recording along x and y directions at focus with vibration non-isolation.

Centroid along x -axis

	90.08908	124.9359	160.2941	196.4527	232.579	268.8593	305.0392	341.1352	376.6545		
53.88472	88.86454	124.2069	159.86	195.7484	232.3456	268.7249	305.1974	341.4236	377.4559	412.9461	
52.91698	87.83262	123.3759	159.3071	195.5171	232.3809	268.6515	305.1863	341.7762	377.8123	413.8855	448.5715
51.96867	87.05815	122.5307	158.6305	195.3079	232.1122	268.8254	305.4136	342.0736	378.0976	413.9737	449.513
51.32698	86.39688	121.8457	158.0485	194.7256	231.7648	268.8417	305.7741	342.2547	378.5588	414.0586	449.8366
50.68331	85.78129	121.2397	157.6461	194.5055	231.5466	268.6377	305.7757	342.1391	378.4656	414.661	450.0342
50.70442	85.62347	121.0961	157.3771	194.4634	231.4705	268.4948	305.6418	342.4453	378.2744	414.2937	449.9379
50.58272	85.56345	121.3223	157.5741	194.3901	231.4767	268.5045	305.5815	342.0002	378.2572	414.0342	449.526
51.04194	85.9168	121.7141	157.4136	194.4301	231.5172	268.3542	305.2261	341.4976	377.763	413.6715	449.0604
51.81152	86.45649	122.0421	157.8007	194.4785	231.4081	267.9529	304.7875	340.965	377.0658	412.8452	448.4624
52.81048	87.26256	122.5028	158.5567	194.7455	231.3583	267.6257	304.333	340.411	376.3676	412.1304	447.5329
	88.30663	123.1947	158.717	194.7188	231.1969	267.5587	303.7092	339.7701	375.7428	411.1898	

Centroid along y –axis

	22.7614	21.96881	21.26556	21.03183	20.92583	20.9233	21.15712	21.63866	22.22704		
58.20098	57.42136	56.74102	56.39821	55.99726	56.06766	55.82883	56.36031	56.82024	57.31771	58.09879	
93.54042	92.76013	92.24955	91.45641	91.4231	91.56334	91.56299	91.98677	92.18391	92.99271	93.78223	94.31358
128.9428	128.3375	128.0662	127.5828	127.3589	127.1581	127.5159	128.1549	128.179	128.8169	129.3101	129.8393
164.9041	164.5435	164.2521	163.8548	163.7374	163.6767	163.8925	164.3615	164.5178	165.1003	165.5017	166.043
200.8331	200.8706	200.8409	200.7315	200.5728	200.7904	201.284	201.1454	201.2607	201.5876	201.9438	202.34
237.0354	237.2007	237.4896	237.7824	237.7404	238.109	238.1822	238.0791	238.533	238.4807	238.5161	238.3959
273.2956	273.7143	274.3459	274.6444	274.9968	275.2789	275.3015	275.3297	274.8394	275.1876	274.9789	274.9054
309.1108	310.0834	311.012	311.4236	311.7779	312.0573	312.2215	311.9941	312.0599	311.6966	311.0336	310.8087
345.4213	346.0119	346.5831	347.5839	348.0731	348.4539	348.4973	348.4932	347.896	347.8439	347.4221	346.9582
380.1757	381.6119	382.5544	383.0434	383.8986	384.3435	384.3082	384.3549	384.0197	383.5409	383.1769	382.4
	416.4606	417.6423	418.5209	419.4171	419.3533	419.6123	419.661	419.3443	419.1255	418.2434	

4. Centroids of image spot recording along x and y directions for defocus position #2 with vibration non- isolation

Centroid along x –axis

	89.2934	124.1798	159.9758	196.1429	232.5618	269.0177	305.4046	341.844	377.4561		
53.09951	87.96638	123.5239	159.4023	195.4896	232.357	268.9213	305.5562	342.0466	378.3	413.9689	
51.78023	86.92225	122.6403	158.7545	195.2319	232.306	268.7935	305.5756	342.2917	378.5556	414.792	449.8547
50.91553	86.26276	121.8191	158.2057	194.9985	232.05	269.0034	305.7505	342.6086	378.9353	414.9957	450.7918
50.29404	85.50637	121.2312	157.6126	194.5498	231.7081	269.006	306.1443	342.7858	379.3737	415.0513	451.0171
49.57221	84.99421	120.541	157.2433	194.3128	231.5257	268.719	306.1805	342.7247	379.1924	415.6289	451.1789
49.55514	84.72553	120.4664	156.911	194.2878	231.4653	268.6249	305.9349	342.9876	379.0296	415.2724	450.9358
49.4629	84.6691	120.6241	157.145	194.1004	231.4782	268.63	305.8292	342.572	378.9587	415.0252	450.8067
49.89269	85.13154	121.1162	156.9309	194.1399	231.472	268.4873	305.5383	342.1143	378.5437	414.618	450.325
50.72302	85.59246	121.4457	157.3997	194.2097	231.3506	268.2381	305.1918	341.5742	377.8153	413.8855	449.8213
51.58433	86.3854	121.7406	158.1089	194.5527	231.3075	267.746	304.5786	340.9617	377.2227	413.0948	448.7751
	87.40309	122.493	158.2748	194.5014	231.1836	267.698	304.0565	340.34	376.5762	412.2192	

Centroid along y –axis

	21.29386	20.37397	19.83493	19.50585	19.42434	19.34813	19.67971	20.06386	20.76587		
57.23009	55.97819	55.44813	55.07746	54.65687	54.78536	54.52043	55.10177	55.48949	56.03423	56.73211	
92.39108	91.68157	91.12321	90.369	90.33519	90.48603	90.48175	90.88346	91.13091	91.8921	92.64317	93.18822
128.0745	127.4237	127.1874	126.6845	126.4479	126.2614	126.6261	127.292	127.3583	127.8851	128.4408	128.8843
164.268	163.75	163.5204	163.1884	163.092	163.0202	163.2807	163.6578	163.8006	164.4505	164.8	165.2786
200.4357	200.3366	200.3699	200.262	200.0441	200.35	200.698	200.6313	200.8778	200.9913	201.38	201.883
236.7042	236.9392	237.1862	237.5234	237.4906	237.7566	237.7488	237.7197	238.2225	238.2151	238.2022	238.1489
273.1524	273.6255	274.2246	274.554	274.8844	275.0739	275.1674	275.1801	274.7918	275.0671	274.8842	274.8213
309.2061	310.2667	311.1085	311.5066	311.8623	312.1305	312.3648	312.1335	312.1318	311.7711	311.1022	310.9137
345.6641	346.3718	346.905	347.9159	348.3781	348.6511	348.7062	348.7333	348.2686	348.1294	347.7163	347.1538
380.693	382.1726	383.071	383.5551	384.4274	384.7153	384.7001	384.7775	384.4765	384.0248	383.6869	382.999
	417.1733	418.4286	419.2532	420.0929	420.025	420.3553	420.4354	420.0283	419.9539	419.0599	

PUBLICATIONS BASED ON THE THESIS

Refereed journals

1. M. Senthil Kumar, A.S. Kiran Kumar, (2012). “Adhesive for optical component: an implementation study,” *J. Opt.*, Springer, **40**(12): 81-88.
2. M. Senthil Kumar, C.S.Narayanamurthy, A.S. Kiran Kumar, (2013). “Iterative method of baffle design for modified Ritchey–Chretien telescope,” *Appl. Opt.*, **52**(6): 1240-1247.
3. M. Senthil Kumar, C.S.Narayanamurthy, A.S. Kiran Kumar, (2013). “Focal length measurement of microlens array for Shack-Hartmann wavefront sensor using interferometer,” *Opt. Eng.*, **52**(12): 124103.
4. M. Senthil Kumar, Rahul Sharma, C.S.Narayanamurthy, A.S. Kiran Kumar, (2014). “Determination of focal length of microlens array by spherical wavefronts,” *Opt. Eng.*, **53**(6): 064102.
5. M. Senthil Kumar, C.S.Narayanamurthy, A.S. Kiran Kumar, (2014). “Design and development of Shack-Hartmann wavefront sensor based-testing of high resolution optical system for earth observation,” *Opt. Eng.*, **53**(11): 11410

Conferences

International

1. M. Senthil Kumar, A.S. Kiran Kumar, C.S.Narayanamurthy, (2011). “Design of wavefront analyser to characterize the space-borne high resolution system,” *Proc. of 35th OSI International symposium on Optics*, Trivandrum, pp: 96-97.
2. M. Senthil Kumar, A.S. Kiran Kumar, (2011). “Adhesive for space-borne optical system – an implementation study,” *Proc. of 35th OSI International symposium on Optics*, Trivandrum, pp: 427-428.

National

1. M. Senthil Kumar, C.S.Narayanamurthy, A.S. Kiran Kumar, (2013). “Hybrid computation method of baffle design for rectangular image format telescope,” *Proc. of 37th OSI National symposium on Optics*, Puducherry, pp: 242-243.

AUTHOR'S BIOGRAPHY

M. Senthil Kumar, received his Master of Technology in Applied Optics from Indian Institute of Technology (IIT) Delhi in 1990 and Master of Business Administration from BK school of Business Management, Gujarat University, Ahmedabad in 1997. He joined Space Applications Center, Indian Space Research Organisation, Ahmedabad as a Scientist/Engineer in 1991. Since then he has been involved in Optical Design, Development of space borne optical systems and test setups for various remote sensing and meteorological satellites. He was the project manager (optical systems) of Cartosat-2, 2A and 2B satellites. Currently, he is the head of reflective optics division and also an associate project director of the next in series Cartosat-3A and 3B satellites. He has registered for Ph.D. in the field of optical engineering at Indian Institute of Space science and Technology (IIST), Thiruvananthapuram on 1st April 2010.